

211
MAGNETIC AND MICROSTRUCTURE PROPERTIES
OF Mm-Fe-B PERMANENT MAGNETS

by

WEI GONG

B.S., Beijing University, 1978

A MASTER THESIS

submitted in partial fulfillment of the
requirements for the degree

MASTER OF SCIENCE

Department of Physics

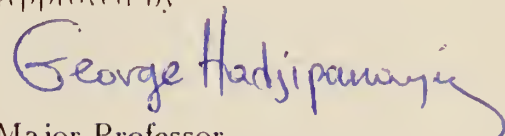
College of Arts and Science

KANSAS STATE UNIVERSITY

Manhattan, Kansas

1988

Approved by



Major Professor

ACKNOWLEDGEMENTS

I am grateful to my advisor Dr. George Hadjipanayis for giving me the opportunity to study in magnetism and magnetic materials in his laboratory. Thanks to him for his guidance, encouragement and support throughout this research.

I would like to thank my thesis committee members, Dr. E. Brock Dale and Dr. M.J.O'shea.

I would like to thank the members of my research group; particularly, Anton Nazareth, Yifei Tao, Jadwiga Strzeszewska and Larry Seib for assisting in the experimental methods, magnetic measurements and the electron microscopy studies.

It is also my pleasure to acknowledge the helpful assistance of all my teachers, colleagues and friends.

I wish to thank my wife, Yiping, for patience and support throughout this work.

I would like to thank Ford Motor Company Electrical and Electronics Division for their support of this research.

CONTENTS

ACKNOWLEDGMENTS	i
CONTENTS	ii
FIGURES	iv
TABLES	vii
Chapter 1 INTRODUCTION	1
1.1 History and Present of Permanent Magnets	1
1.2 Previous Work on Mn-Fe-B Magnets	5
1.3 Objectives of Present Study	6
Chapter 2 THEORETICAL BACKGROUND OF PERMANENT MAGNET	10
2.1 Hysteresis Loop	10
2.2 Magnetic Anisotropy	12
2.2.1 Shape Anisotropy	12
2.2.2 Magnetocrystalline Anisotropy	13
2.3 Curie Temperature	15
2.4 Single Domain Particles	16
2.5 Coercivity	17
2.5.1 Coercivity of Powder Particles	18
2.5.2 Coercivity Associated with Magnetization Rotation in SDP	18
2.5.3 Coercivity Associated with Nucleation	19
2.5.4 Coercivity Associated with Domain Wall Pinning	21
Chapter 3 EXPERIMENTAL TECHNIQUES	26
3.1 Alloy Preparation	26
3.2 Melt-Spinning Method	26
3.3 Powder Metallurgy Method	27
3.3.1 Powder Preparation	27
3.3.2 Alignment and Compaction of Powders	27

3.3.3 Sintering and Annealing	28
3.4 Magnetic Measurements	28
3.5 Microstructure and Phase Analysis	29
3.5.1 X-ray Diffraction	29
3.5.2 DTA and DSC Analysis	29
3.5.3 TEM and EDXA Analysis	30
 Chapter 4 Mm-Fe-B RIBBONS	 32
4.1 Substitution of Mm for Nd in $\text{Fe}_{76}\text{Nd}_{16-x}\text{Mm}_x\text{B}_8$ Ribbons	33
4.2 Substitutions of Ni and Dy in Mm-Fe-B Ribbons	34
4.3 Substitution of Al for Fe in Mm-Fe-B Ribbons	34
 Chapter 5 Mm-Fe-B SINTERED MAGNETS	 45
5.1 Effect of Particle Size	45
5.2 Effect of Sintering and Annealing Temperature	46
5.3 Al Substitution in Sintered Magnets	47
5.4 Addition of Dy_2O_3 , Nd_2O_3 and Dy in Sintered Magnets	48
5.5 Temperature Characteristics of Mm-Fe-B Magnets	49
5.6 Phases and Microstructure in a Mm-Fe-B Sintered Magnets	50
 Chapter 6 SINGLE PHASE $\text{R}_2\text{Fe}_{14}\text{B}$ POWDERS AND RIBBONS ...	 72
6.1 $\text{Mm}_2\text{Fe}_{14}\text{B}$ Powders and Ribbons	73
6.2 $\text{Nd}_2\text{Fe}_{14}\text{B}$ Powders and Ribbons	74
6.3 $\text{Dy}_2\text{Fe}_{14}\text{B}$ Powders and Ribbons	75
6.4 Coercivity Mechanism	75
 CONCLUSIONS	 89
REFERENCES	90
ABSTRACT	94

FIGURES

Fig. 1.1	The maximum energy product $(BH)_{max}$ as a function of time.	8
Fig. 1.2	The price per unit energy product of various materials as a function of time.	9
Fig. 2.1	A typical magnetic hysteresis loop of a permanent magnet. ...	23
Fig. 2.2	Calculating the maximum energy product.	23
Fig. 2.3	The coercivity H_c of powders versus on particle diameter D. ..	24
Fig. 2.4	Two types of the coercivity mechanism for permanent magnets.	25
Fig. 3.1	Melt spinning technique.	31
Fig. 4.1	Hysteresis loops of a typical Mn-Fe-B ribbons.	36
Fig. 4.2	The crystallization temperature of Mn-Fe-B based ribbons. ...	37
Fig. 4.3	The temperature dependence of magnetization M in a small magnetic field.	38
Fig. 4.4	Magnetic properties of Mn-Fe-B ribbons as a function of misch metal concentration x.	39
Fig. 4.5	Dependence of coercivity H_c in Mn-Fe-B ribbons on Ni, Sn and Dy concentrations.	40
Fig. 4.6	Magnetic properties of Mn-Fe-B based ribbons as a function of the concentration of Al and Dy.	41
Fig. 5.1	The magnetic properties of the ribbons are isotropic.	52
Fig. 5.2	Coercivity H_c versus particle size in Mn-Fe-B sintered magnets.	53
Fig. 5.3	The coercivity of Mn-Fe-B sintered magnets as a function of the sintering temperature.	54
Fig. 5.4	The coercivity of Mn-Fe-B sintered magnets as a function of the annealing temperature.	55
Fig. 5.5	Magnetic properties of Mn-Fe-B sintered magnets as a function of Al concentration.	56
Fig. 5.6	Substitutions Al for Mn in Mn-Fe-B sintered magnets.	57
Fig. 5.7	Substitutions Mn for Fe in Mn-Fe-B sintered magnets.	58

Fig. 5.8	The effect of additions of Dy_2O_3 and Nd_2O_3 powder in Mm-Fe-B sintered magnets.	59
Fig. 5.9	The hysteresis loops of $Fe_{68}Al_2Mm_{22}B_8 + x \text{ wt}\% Dy_2O_3$ sintered magnets.	60
Fig. 5.10	Magnetization curves of several Mm-Fe-B samples.	61
Fig. 5.11	Temperature dependence of coercivity H_c and magnetization M_s in Mm-Fe-B sintered magnets.	62
Fig. 5.12	Temperature dependence of coercivity H_c and magnetization M_s in Mm-Fe-Co-B based sintered magnets.	63
Fig. 5.13	Hysteresis loops of $Fe_{75}Al_xMm_{16}Dy_1B_7 + 5 \text{ wt}\% Dy_2O_3$ sintered magnets at different temperatures.	64
Fig. 5.14	The Curie temperature of Mm-Fe-B based sintered magnets.	65
Fig. 5.15	Grain sizes of the $Fe_{68}Al_2Mm_{22}Dy_1B_8$ sintered magnets. ...	66
Fig. 5.16	Grain sizes of the $Fe_{75}Al_2Mm_{16}Dy_1B_7 + 5 \text{ wt}\% Dy_2O_3$ sintered magnets.	67
Fig. 5.17	DTA analysis of a $Fe_{68}Al_2Mm_{22}Dy_1B_8$ sintered magnet. ...	68
Fig. 5.18	DSC analysis of the Mm-Fe-B sintered magnets.	69
Fig. 6.1	Grain sizes of the single phase $Nd_2Fe_{14}B$ ribbons with optimum wheel speed.	77
Fig. 6.2	Grain sizes of the single phase $Dy_2Fe_{14}B$ ribbons with optimum wheel speed.	78
Fig. 6.3	Magnetization curves of $Mm_2Fe_{14}B$ powders.	79
Fig. 6.4	Anisotropy constants K_1 , K_2 and K_u of $Mm_2Fe_{14}B$ alloy.	80
Fig. 6.5	Magnetic properties of the single phase $Nd_2Fe_{14}B$ powders versus particle size D.	81
Fig. 6.6	The coercivity H_c of Nd-Fe-B ribbons as a function of grain size.	82
Fig. 6.7	Hysteresis loops of single phase $Nd_2Fe_{14}B$ at different temperatures.	83
Fig. 6.8	The coercivity of the single phase $R_2Fe_{14}B$ (R = Nd, Dy)	

powders and ribbons as a function of temperature.	84
Fig. 6.9 Hysteresis loops of single phase $Dy_2Fe_{14}B$ at different temperatures.	85
Fig. 6.10 Initial magnetization curves and hysteresis loops of the single phase $R_2Fe_{14}B$ powder and ribbons at room temperature. ...	86
Fig. 6.11 The coercivity H_c of $R_2Fe_{14}B$ ($R = Nd, Dy$) powder and ribbons as a function of applied field H	87
Fig. 6.12 The coercivity H_c of $R_2Fe_{14}B$ ($R = Nd, Dy$) ribbons as a function of applied field H	88

TABLES

Table 4.1	Magnetic properties and crystal structure of single phase $R_2Fe_{14}B$	42
Table 4.2	Magnetic properties of Mm-Nd-Fe-B ribbons.	43
Table 4.3	Magnetic properties of Mm-Fe-B ribbons with Ni, Sn and Dy additions.	43
Table 4.4	Magnetic properties of Mm-Fe-B ribbons with Al and Dy additions.	44
Table 5.1	Magnetic properties of Mm-Fe-B sintered magnets.	70
Table 5.2	X-ray analysis.	71

Chapter 1

INTRODUCTION

1.1 History and Present of Permanent Magnets

Permanent magnets were known in the Ancient World in the form of loadestone in Greece before 800 BC and marked the beginning of magnetism. There were early observations of attractive and repulsive forces between loadestones and the compass was used for identifying directions in China about 2500 BC [1].

The first synthetic permanent magnet (Fe_3O_4) was made by Gowin Knight and described by Benjamin Wilson [2] in 1779. Later, bar and horseshoe magnets made from T-steel ($T = C, W, Co$) were well known and widely used.

A major advance in magnetic materials was made in 1932, when the development of the Al-Ni-Co magnets started with Mishimas' Al-Ni-Fe [3]. Rapid progress in permanent magnet development since then, has been the result of an increasing understanding of the fundamental origin of permanent magnet behavior and its relation to metallurgical structures. One of the milestones in this development was the emergence of domain theory [4] which led to the concept of the single domain particle and the contribution of

magnetic anisotropy giving rise to the permanent magnet behavior of magnetic materials. The magnetic and mechanical hardness of the Alnico alloy is due to a thermal treatment leading to precipitation of a second phase in a finely dispersed form. This development culminated with an Alnico alloy hardened in the presence of a magnetic field which leads to the precipitation of oriented second-phase particles of elongated shape [5]. The maximum energy product achieved was about 11 MGOe [6].

The next breakthrough in the the development of high energy product materials was made with Rare-Earth Transition (R-T) metal compounds. Strnat had made a magnet having an energy product of 20 MGOe by sintering $SmCo_5$ in 1969 [7]. Even higher values, up to 35 MGOe, were reported in a related material with the formula $(Sm)_2(CoFe)_{17}$ [8]. Due to the huge magnetocrystalline anisotropy of these compounds, much larger coercivities were obtained than in previous materials. In Sm-T compounds (T = 3d transition metals), strong 3d-3d exchange interactions stabilize the magnetic ordering against thermal agitation at high temperature and 4f-3d magnetic interactions sustain the R-sublattice magnetization, leading to a the strong 4f anisotropy at temperature well above room temperature.

Because Sm and Co are less abundant resource materials, there has been a growing interest in Rare-earth-Fe base alloys. Nd and Pr are very abundant in ordinary Rare Earth ores; moreover, both elements couple ferromagneti-

cally with Fe leading to larger magnetic moments. Fe which is almost inexhaustible compared to Co, in most metallic substances, possesses a larger magnetic moment than Co. But, none of the binary R-Fe compounds exhibit the magnetic properties required for a good permanent magnet. This is because the Curie temperatures are too low, the compounds have few stable intermetallic phases and none of the compounds shows a uniaxial magnetic anisotropy [9].

However, there were some indications of a trend in permanent magnets in the early 1980's. N. C. Koon and B. N. Das [10] knowing that boron enhances the likelihood of rapidly cooled materials being amorphous, examined the Tb-La-Fe-B system. They found that as they annealed these amorphous alloys at successively higher temperatures the coercivity increased sharply and then decreased. The maximum value of the coercivity was 9 KOe. J. J. Croat [11] prepared a series of specimens by spinning the wheel at different speeds and produced high coercivity in ribbons of $R_{40}Fe_{60}$ alloys where R = Pr, Nd and Sm. The ribbons of both alloys had a smaller magnetic energy product because of the lower magnetic moment, but these investigations formed the background for the development of the new rare earth iron boron permanent magnets.

In 1983, a breakthrough occurred in permanent magnetic materials, when G. C. Hadjipanayis [12] reported that FePrSiB ribbon samples had high

coercivities $H_c = 15$ KOe and $(BH)_{max} = 12$ MGOe, J. J. Croat [13] and N. C. Koon [14] had similar results in NdFeB and PrFeB ribbons. Later M. Sagawa [15] from Sumitomo's reported a sintered NdFeB magnet with $(BH)_{max} = 36$ MGOe made by the conventional powder method. These reports caused a sensation throughout the world of magnetic materials. The outstanding permanent magnetic properties of Nd-Fe-B alloys are due to the tetragonal $Nd_2Fe_{14}B$ phase [16] [17] which has a saturation magnetization $4\pi M_s = 16000$ G, an anisotropy field $H_A = 68$ KOe, and a Curie temperature $T_c = 315$ °C [18].

At the present the Nd-Fe-B magnets form a large family of magnets with varying alloy composition (Nd-Fe-B-M). Co substitution, $M = Co$, increases the Curie temperature and $M = Al, Dy$ substitutions, increase coercivity [19] [20]. The highest value of $(BH)_{max}$ for Nd-Fe-B magnets is up to 50 MGOe [21]. The value has increased by a factor of more than 100 to compare with the T-steel magnets. Fig. 1.1 shows the improvements achieved in maximum energy product over the years [21,22,23]. The record values are shown on a logarithmic scale. It is interesting to note how closely the curve approximates to an exponential development.

Fig. 1.1 also shows the Ferrite materials indicated as Fxd100 and Fxd330 which are very important in permanent magnets. The Ferrites were first pointed out by J. J. Went in 1952 [24]. The energy product of these materials

falls clearly below the general trend. They are a typical representation of the family of low cost permanent magnet materials having a medium energy product. Another systematic correlation is also observed, the price per unit energy product of various materials with time (see Fig. 1.2.). The figure shows clearly the continuous progress made in improving the economy of permanent magnet. Ferrites occupy a leading position and are the end point of the long development; moreover, the volume of Ferrites make up more than 80 percent of the total permanent magnets [22]. The great economic success of Ferrites is due to the low price per unit of available magnetic energy (see Fig. 2.2). Ferrites are inexpensive because they do not contain any rare materials such as nickel or cobalt and to make them it is only necessary to "mix a few cheap materials " to "bake them to the right shape".

1.2 Previous Work on Mm-Fe-B Magnetic Property

The impact of the Nd-Fe-B magnets will depend on both technological and economic factors. The Nd-Fe-B magnets in their present form are very expensive and can not compete with Ferrites. The high price of Nd-Fe-B is mostly due to Nd which is still quite expensive. It is known that $R_2Fe_{14}B$ magnetic phase exists in most Rare earth elements (R), such as R = Y, La, Ce, Pr, Nd, Dy, and Tb [25,26,27,28]. There is a great potential in Mm-Fe-B alloys for permanent magnet development (Mm = Misch metal). C. A.

Paik [29] has recently made permanent magnets containing a special form of Misch metal (85 %Nd, 15%Pr, and 5%Ce). However, the magnet still has high percentage of Nd and Pr. O. Popov [30] prepared Mm-Fe-B ribbons by melt-spinning with different wheel speeds. The coercivity of the ribbons was about 9 KOe. J .Yamasaki [31] prepared the plastic magnets from ribbons with $H_c = 7$ KOe and $(BH)_{max} = 4.4$ MGOe.

1.3 Objectives of Present Study

Mm-Fe-B magnets show a great potential for permanent magnet development and might be the only alternative to Nd-Fe-B that comes close to competing with the Ferrite magnets [32].

The purpose of this work has been to study the hard magnetic properties and microstructure of Misch-metal magnets and to develop a Mm-Fe-B based permanent magnet (Mm = 50%Ce, 25%La, 15%Nd, 5%Pr and 5%Others in weight percent). The magnets were prepared by melt-spinning and powder metallurgy methods. The hard magnetic properties of the magnets were improved by adding small amounts of *Dy*, *Al* and Dy_2O_3 . An economical permanent magnet, whose price per energy product may compete with Ferrites, has the following composition and magnetic properties; for a typical sample of $Fe_{75}Al_1Mm_{16}Dy_1B_7$ with 5 wt% Dy_2O_3 , $H_c = 7 \sim 9$ KOe, $4\pi M_r = 7500 \sim 8000$ G, $(BH)_{max} \approx 12$ MGOe and $T_c = 515$ K. The

density of the alloy is 7.3 g/cm^3 . The high saturation M_s and Curie temperature T_c can be explained by the presence of $Mm_2Fe_{14}B_1$ phase in the alloy which has been confirmed by X-rays. The coercivity mechanism of the magnets will be discussed using theoretical models associated with high magnetocrystalline anisotropy.

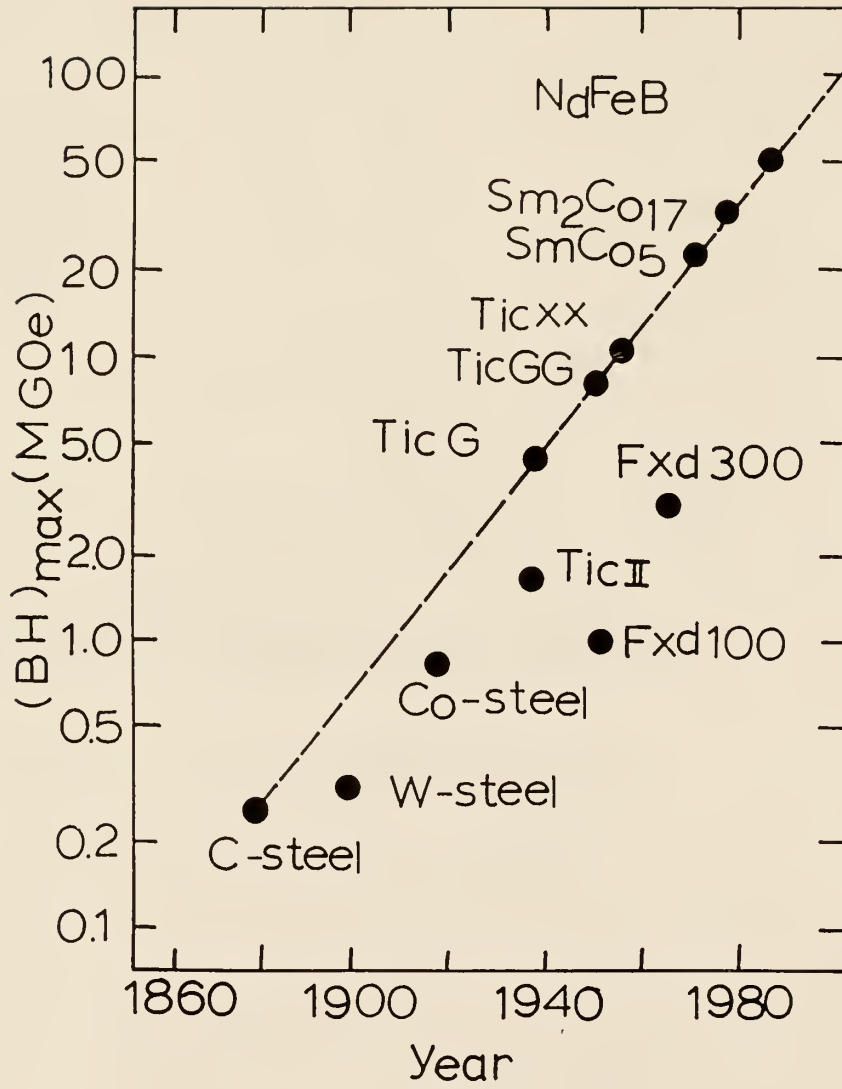


FIG. 1.1 The maximum energy product $(BH)_{max}$ as a function of time.

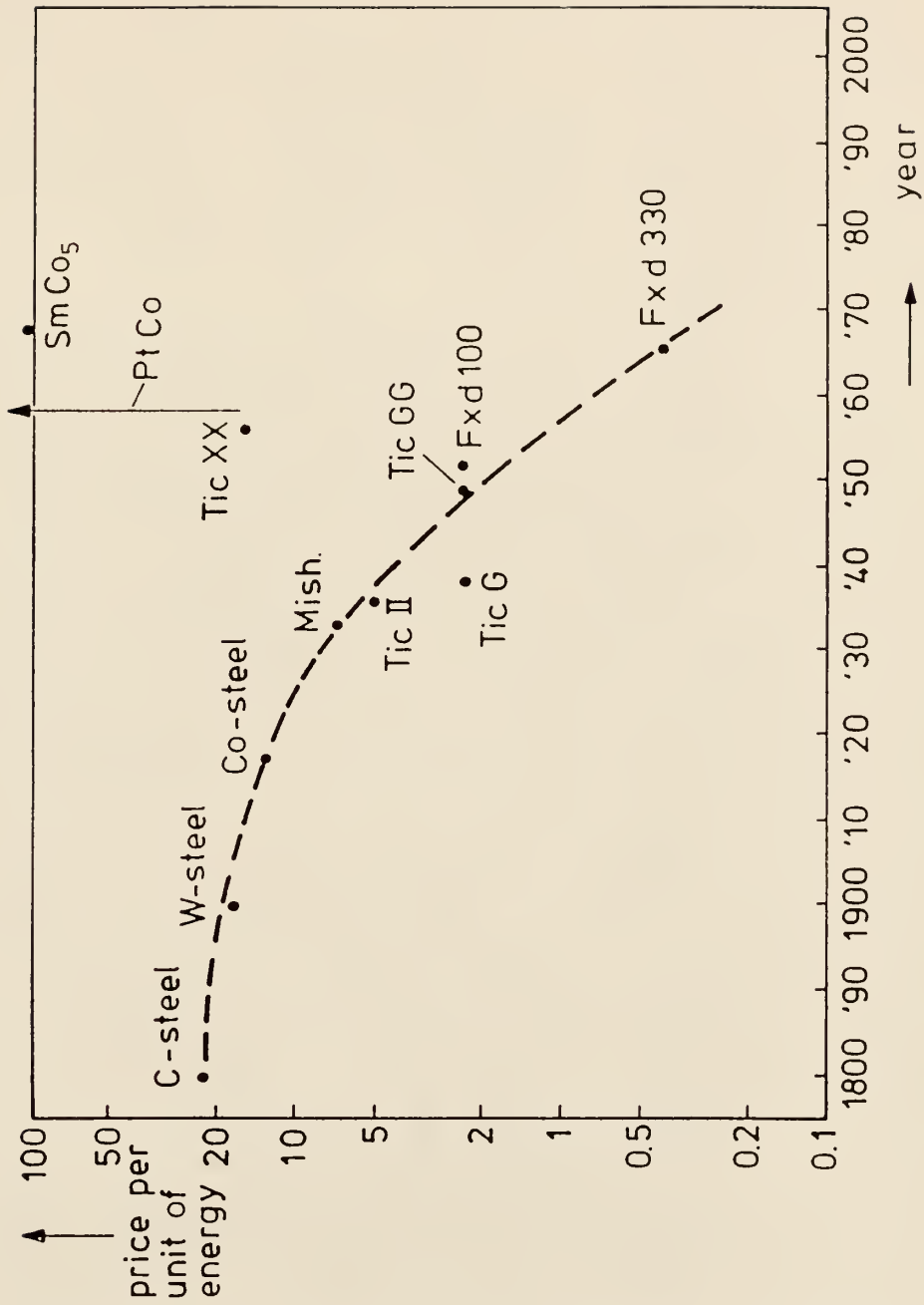


Fig. 1.2 The price per unit energy product of various materials as a function of time.

Chapter 2

THEORETICAL BACKGROUND OF PERMANENT MAGNET

2.1 Hysteresis Loop

Permanent magnet materials are characterized by high coercivities and high remanent magnetizations. Before proceeding with the discussion of the structural parameters that determine the hard magnetic properties, we must first define the parameters that are generally used to specify the magnetic properties of permanent magnets. The magnetic flux density B is expressed as

$$B = H + 4\pi M \quad , \quad (2.1)$$

where M is the local material contributions to the flux density and is called magnetization and H is the contribution from all other sources and is called magnetic field strength. If the magnetization M of a permanent magnet material is plotted as a function of the applied field H , a hysteresis loop is obtained in which the magnetization is not a unique function of H , but depends on the direction and magnitude of applied field. A typical hysteresis loop is shown in Fig. 2.1 [33].

The initial magnetization curve starting at the origin (O to A) is obtained when the material is in a thermally demagnetized state. If the maximum applied field H_m is sufficient to saturate the magnetization loop

it is referred to as a saturation loop (A-B-C-D-E-F), and the maximum magnetization is called saturation magnetization, M_s . When the applied field is reduced to zero the magnetization decreases to the remanent magnetization M_r , which is generally less than the saturation magnetization M_s . In an efficient permanent magnet material M_r is usually $0.8 \sim 1.0 M_s$.

If the material is subjected to a demagnetizing field (i.e. a negative applied field H) the magnetization is gradually reduced and at a critical field $-H = H_c$ the magnetization is zero (B to C). This critical field is known as the coercivity H_c and is defined as the reverse field required to reduce the net magnetization of the material to zero in the presence of the field.

The product of the flux density B and the associated opposing field H , referred to as the energy product, is a usual measure of the performance of a particular magnet, since it is proportional to the potential energy of the field in the air gap. The maximum value of the product ($B \times H$) is called $(BH)_{max}$. The ultimate limit to the maximum energy product of any material is given by $B_r^2/4$. To approach this limit, it is necessary to have nearly perfect alignment of the magnetic easy axes within the material, which makes possible a high remanence to saturation ratio M_r/M_s . Good permanent magnet performance requires high coercivity to ensure high resistance to demagnetization. It is also necessary to have the coercivity at

least as high as $B_r/2$. To determine the energy product hysteresis loop of the material must be known (Fig. 2.2).

2.2 Magnetic Anisotropy

The magnetic properties of a ferromagnet depend on the direction in which they are measured since the sample possess a certain magnetic anisotropy. Magnetic anisotropies are important in determining the properties of permanent magnet materials; higher magnetic anisotropy usually results in higher coercivity. The magnetic anisotropy may be of different origin. The most important anisotropies in permanent magnetic materials are: (a) shape anisotropy, associated with the geometrical shape of a magnetized body; (b) magnetocrystalline anisotropy, associated with the crystal symmetry of the material. They are discussed below.

2.2.1 Shape Anisotropy

The shape anisotropy concept was proposed almost simultaneously by L. Neel [34], C. Guillaud [35], and E. C. Stoner and E. P. Wohlfarth [36]. Shape anisotropy occurs in elongated particles because the magnetization prefers to lie along the major axis where the demagnetization factor is a minimum and magnetostatic energy is therefore lowest. The density of demagnetizing energy is

$$F_{dem} = \frac{1}{2} N M_S^2. \quad (2.2)$$

Where N is a constant demagnetization factor. N_a , N_b and N_c are the demagnetization factors along the axes, here

$$N_a + N_b + N_c = 4\pi \quad (2.3)$$

For an ellipsoid of revolution ($a > b = c$), the density of demagnetizing energy becomes

$$F_{dem} = \frac{1}{2}(N_a \cos^2 \phi + N_b \sin^2 \phi)M_s^2.$$

$$F_{dem} = Const + \frac{1}{2}(N_b - N_a) \sin^2 \phi M_s^2. \quad (2.4)$$

The constant of shape anisotropy is defined by

$$K_{sha} = \frac{1}{2}(N_b - N_a)M_s^2. \quad (2.5)$$

The maximum value of K_{sha} is obtained for a greatly elongated ($N_a \ll N_b$) or oblate ($N_a \gg N_b$) ellipsoid. When N_a or $N_b \approx 2\pi$, So that

$$|K_{sha}| \approx \pi M_s^2. \quad (2.6)$$

For example, $M_s \approx 1700$ G for Fe, the maximum value $K_{sha} = 9 \times 10^6$ ergs/cm³.

2.2.2 Magnetocrystalline Anisotropy

Magnetocrystalline anisotropy is the result of the existence of preferred crystalline axes for magnetization and is an intrinsic property of the material.

The crystal anisotropy energy is defined as the work required to make the magnetization lie along a direction different from the easy direction. Crystal anisotropy is due to spin-orbit coupling. Magnetocrystalline anisotropy is the an intrinsic property that is found in atoms possessing an electron-orbital moment in addition to the electron-spin moment. In such a situation the spin direction may be coupled to the crystal axes. This arises through the coupling between spin and orbital moment and the interaction between the charge distribution over the orbit and the electrostatic field of the surrounding atoms. The crystal will then be preferentially magnetized along one or more easy axes.

For a uniaxial crystal magnetic material [37], the anisotropy energy is given by

$$E_k = K_1 \sin^2 \theta + K_2 \sin^4 \theta. \quad (2.7)$$

Where K_1 and K_2 are the anisotropy constants for the material, and θ denotes the angle between the magnetization M_s and the c-axis.

The anisotropy constants can be calculated from

$$\frac{2K_1}{M_s} + \frac{4K_2}{M_s^3} M_H^2 = \frac{H}{M_H} M_s. \quad (2.8)$$

This latter expression corresponds to the Sucksmith-Thompson [38] formula which in general is used for determining K_1 and K_2 by plotting M_H^2 versus

$$\frac{H}{M_H}.$$

In another experiment, the uniaxial anisotropy constant \mathbf{K} can be found from the anisotropy field H_A of the material, $\mathbf{K} = M_s H_A / 2$. Equation (2.8) may be rewritten as

$$\mathbf{K} = K_1 + 2K_2 . \quad (2.9)$$

For $Nd_2Fe_{14}B$ single crystal,

$$K_1 = 4.2 \times 10^7 \text{ erg/cm}^3 ,$$

$$K_2 = 0.7 \times 10^7 \text{ erg/cm}^3 ,$$

$$\mathbf{K} = 4.2 \times 10^7 \text{ erg/cm}^3 , \text{ at room temperature [39].}$$

2.3 Curie Temperature

In a ferromagnetic material the atomic dipole moments are strongly coupled in a parallel arrangement and a spontaneous magnetization exists in the material. The Curie temperature T_c is the critical temperature of the ferromagnetic material which breaks this coupling and the material becomes paramagnetic [40]. Curie temperature T_c of four typical ferromagnetic materials are listed below [41]:

$$T_c(F_e) = 770 \text{ } ^\circ C$$

$$T_c(C_o) = 1131 \text{ } ^\circ C$$

$$T_c(N_i) = 358 \text{ } ^\circ C$$

$$T_c(G_d) = 16 \text{ } ^\circ C$$

2.4 Single Domain Particles

The classical theory of ferromagnetism (Weiss molecular field theory) [42,43] is based on the existence of domains. The domains are regions of parallel aligned magnetic moments. Each domain may be thought of as a tiny magnet pointing in a certain direction. A ferromagnet is generally composed of many such domains, pointing in many different directions. If sample size is reduced, for instance by crushing the material to form a fine powder, the particles will gradually become as small as individual domains. This is known as a single domain particle state. The particle becomes a miniature permanent magnet with the highest coercivity.

The single domain particle diameter D_c is an important parameter [44]

$$D_s = 1.4 \frac{\gamma}{M_s^2}$$

For $Nd_2Fe_{14}B$, the domain wall surface energy γ was determined to be 35 ergs/cm^2 [45], and therefore

$$D_s = 0.3 \mu m$$

Single domain particles possess properties that make them ideal permanent magnet materials. If a large anisotropy is present, they have a large coercivity. Also if they are aligned in a material with a large spontaneous magnetization, the magnet has both a large remanence and a large value of

$(BH)_{max}$. There are two general methods of manufacturing small-particle magnets. In one method the single domain particles of a powder are first aligned and then compressed; sometimes a nonmagnetic binder is added. In the other method an alloy is treated metallurgically so that small ferromagnetic particles are precipitated out into a relatively nonmagnetic matrix; that is, at least two phases are produced. Historically, the second method came first and indeed preceded the development of the theory of single domain particles.

2.5 Coercivity

Over the past half-century, progress in permanent magnetic materials has been remarkable. The coercivities available have increased from about 250 Oe to over 40 KOe, and maximum energy products have increased from about 1 MGOe to over 50 MGOe. These properties of permanent magnet materials are among the most structure-sensitive of all engineering properties of materials. Progress has been aided by an interplay between theoretical models, experimental measurement, and microstructural studies, all aimed at understanding the mechanisms of magnetization reversal.

As we saw in the previous section 2.1 that coercivity of permanent magnetic material should be at least as high as $B_r/2$. For shape and application involving large demagnetization fields, even higher coercivities are desirable.

The task of the materials scientist is to produce a permanent magnet with high values of saturation induction B_s , remanent induction B_r and coercivity H_c . In most case, the most challenging part of that task is to understand and control the coercivity, the primary measure of magnetic hardness.

2.5.1 Coercivity of Powder Particles

The coercivity of powder particles has a striking dependence on particle size. As the particle size is reduced, it is typically found that the coercivity increases, it goes through a maximum, and then tends toward zero. Fig. 2.3 shows very schematically how the size range is divided in relation to the variation of coercivity with particle diameter D [46]. Below a critical diameter D_s , the particles become single domain, and in this size range the coercivity reaches a maximum. When particle size decreases below D_s , the coercivity decreases because of thermal effects. Below a critical diameter D_p the coercivity is zero. Such particles are called superparamagnetic [46].

2.5.2 Coercivity Associated with Magnetization Rotation in SDP.

Magnetization reversal in a permanent magnet material occurs by the coherent or incoherent rotation of magnetization within individual domains and or by the nucleation and growth of reverse domains. The coherent and incoherent rotation of magnetization will be discussed in this section. The

nucleation and growth of reverse domains will be discussed in the next two sections.

From calculations using micromagnetic theory [47], magnetization reversal of a prolate spheroid may occur by a basic mechanism: the coercivity due uniform magnetization rotation (coherent mode) is equal to the anisotropy field H_A .

For shape anisotropy:

$$H_c = H_A = (N_b - N_a)M_s , \quad (2.10)$$

For magnetocrystalline anisotropy:

$$H_c = 2K/M_s , \quad (2.11)$$

where N_a and N_b are the demagnetization factors parallel and perpendicular to the major axes of the spheroid. The maximum value of ($N_b - N_a$) for infinite elongation is 2π , so that the maximum attainable coercivity from shape anisotropy is $2\pi M_s$. However, the experimental coercivity is lower than the theoretical value. Therefore, the incoherent modes are considered. There are two other important modes of magnetization reversal; the fanning and curling [48].

2.5.3 Coercivity associated with nucleation

In most real materials, coercivity H_c is determined by the nucleation field in magnets of single domain grains and by the pinning of domain walls

in precipitation hardened magnets. The initial magnetization behavior of the magnets can be used to distinguish between the two different types of the coercivity mechanism (see Fig. 2.4 [49]).

According to nucleation of reverse domains model the magnetization reversal is initiated by the nucleation of oppositely magnetized regions when the applied magnetic field exceeds a critical value. In the homogeneous rotation case, the nucleation field is

$$H_N = \frac{2K}{M_s}. \quad (2.12)$$

Brown's theory [50] pointed out that a perfect crystal of any size can be treated as single domain particle after magnetic saturation. The magnetization reversal occurs by rotation of the polarization. Nucleation of reversed domains occurs when (H antiparallel to M_s) [51]:

$$H_N + NM_s > \frac{2K}{M_s}$$

$$H_c = H_N = \frac{2K}{M_s} - NM_s. \quad (2.13)$$

After nucleation of reversed domains the crystal will spontaneously divide into domains.

However, the coercivities in actual crystals are a factor 3 ~ 10 smaller than the theoretical value. This phenomenon, known as Brown's paradox [50], is explained by the existence of crystal lattice defects, regions with low M_s ,

and K , surface closure domains, and surface irregularities. In these regions N may be large and K significantly smaller and therefore H_A much smaller [52].

The domain nucleation mode can explain the coercivity of single phase crystal anisotropy magnets, such as S_mCo_5 , Ferrites and MnAlC, which have high initial permeability after thermal demagnetization and strong dependence of coercivity on magnetic field.

2.5.4 Coercivity Associated with Domain Wall Pinning

In precipitation hardened permanent magnets coercivity is controlled by pinning of domain walls by a finely dispersed or coherent precipitation of a second phase. The narrow domain walls can be pinned by compositional disorder in magnetic anisotropy, producing high coercivity. The width of a magnetic domain wall is determined by a balance between the competing forces of crystal anisotropy, which tries to keep the wall narrow, and exchange force, which tries to keep it wide. The coercivity can be found from the gradient of the interaction energy Φ in general form:

$$H_c = \frac{1}{2M_s \cos \alpha} \left(\frac{\partial \Phi}{\partial X} \right)_{max}, \quad (2.14)$$

where α is a angle between the magnetization and the magnetic field.

M. Kersten [53] proposed a model to calculate the coercivity from the interaction of domain walls with cavities and non-ferromagnetic inclusions.

According to the model

$$H_c = \left(\frac{3\alpha}{4\pi} \right)^{2/3} \frac{\pi\gamma}{rM_s}, \quad (2.15)$$

where r is the radius and α is the occupancy of the non ferromagnetic sphere, and γ is the domain wall energy per unit area.

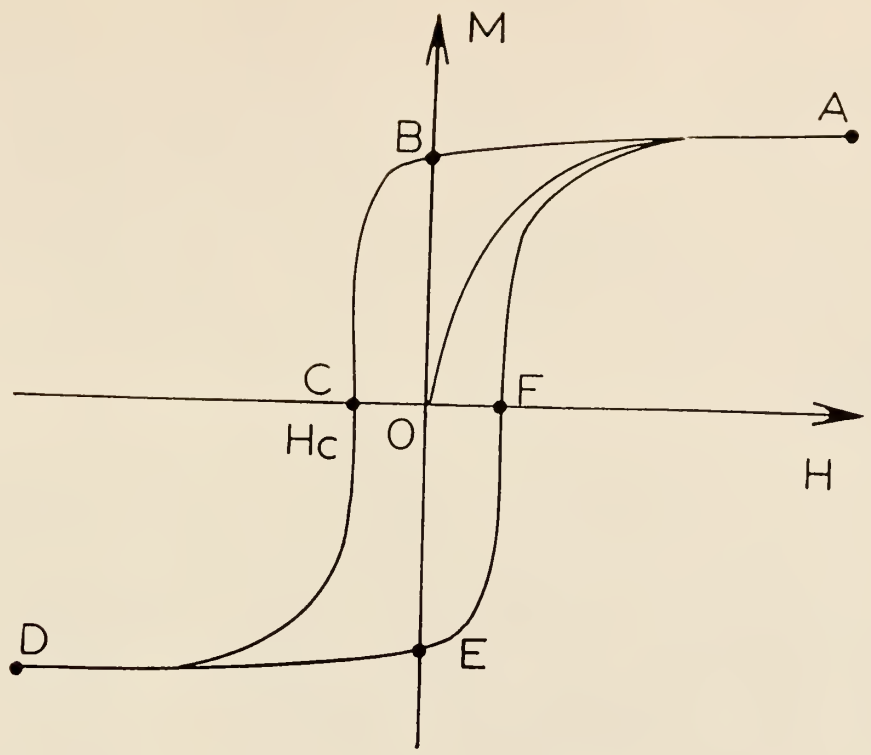


Fig. 2.1 Magnetic hysteresis loop.

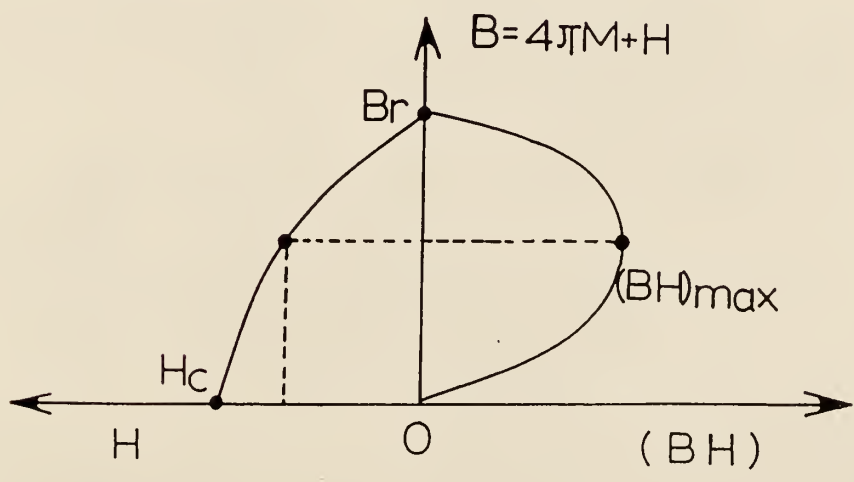


Fig. 2.2 The maximum energy product $(BH)_{max}$.

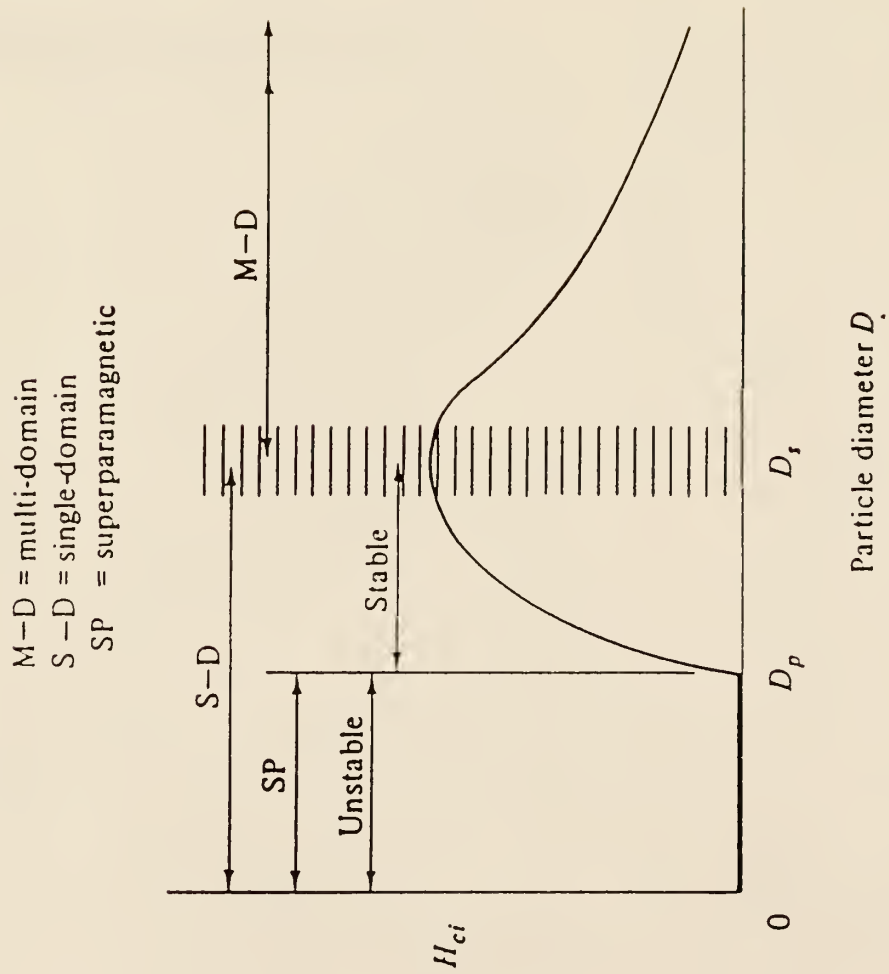


Fig. 2.3 The coercivity H_c of powders versus particle diameter D . D_s and D_p are the critical diameters for single domains and super-paramagnets.

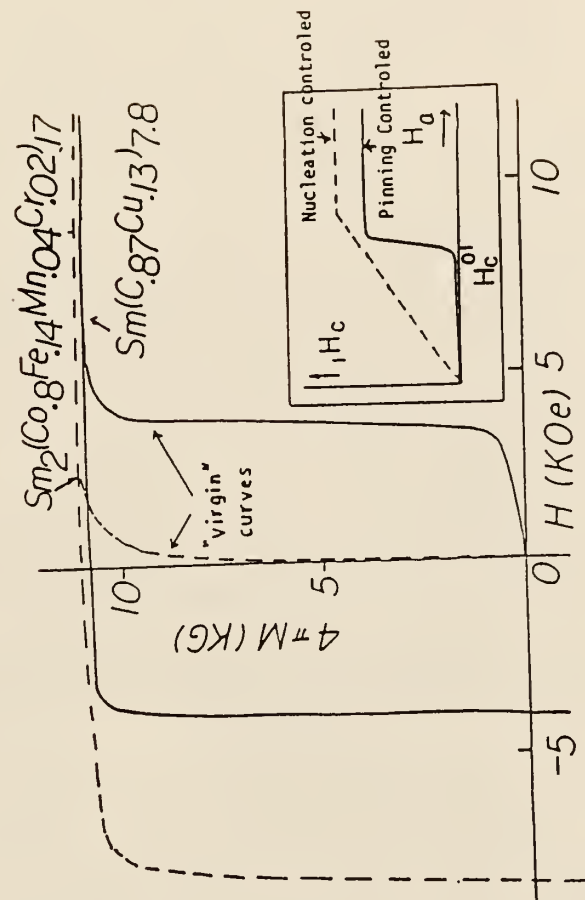


Fig. 2.4 The two types of the coercivity mechanism have different behavior in the initial magnetization curve and field dependence of H_c .

Chapter 3

EXPERIMENTAL TECHNIQUES

3.1 Alloy Preparation

The purity of the elements used to prepare the magnets was 99.9% or better with the exception of Mm. the Misch metal alloy Mm includes 50%Ce, 25%La, 15%Nd, 5%Pr, 3%Heavy rare earth, and 2% Others in weight percent. Boron was used in the form of FeB alloy which includes 81.7%Fe and 18.3%B in weight percent. As-cast alloys of the samples to be studied were made into buttons of 5 ~ 8 grams by arc-melting in a high purity argon atmosphere. The buttons were remelted four times, so as to improve their homogeneity. The weight losses of the sample were kept below 0.5% after melting.

For the powder samples, the buttons were homogenized at a high temperature 1000 °C for 24 hours.

3.2 Melt-Spinning Method

Amorphous alloys were prepared in a ribbon form by the melt-spinning technique (as Fig.3.1) [54,55]. The alloy button was broken into smaller pieces to fit inside a quartz tube. The top of the tube was connected with argon gas. The bottom of the tube had a small orifice with diameter about

0.5 mm. When the sample was melted by a high frequency induction coil and argon gas was introduced into the tube, the molten alloy was ejected into the Cu wheel and was rapidly cooled and solidified into a ribbon form which was 1 ~ 2 mm wide and 20 ~ 50 μm thick. The microstructure of the ribbons depends on the quenching rate that is related to wheel speed, distance between the orifice and the surface of the wheel, and pressure of the argon gas. For optimum magnetic hardening, the ribbons were used with different wheel speed or they were heat-treated at a temperature in the range of 600 ~ 750 $^{\circ}\text{C}$ under argon gas or in high vacuum.

3.3 Powder Metallurgy Method

A typical powder metallurgy technique involves preparation of fine powder, aligning and pressing the powder in magnetic field, and then sintering and annealing the "green compact" at suitable temperatures.

3.3.1 Powder Preparation

The as-cast alloy was crushed into coarse powder which had diameter of about 150 μm using a stainless steel mortar or a micro-mill machine under an argon gas atmosphere. The coarse powder was ground further to about 3 ~ 5 μm with ball-milling in a methylene chloride liquid.

3.3.2 Alignment and Compaction of Powders

The wet powder was aligned in a magnetic field of 10 KOe and pressed under a pressure of 7000 Kg/cm^2 . The aligning direction of the powder was perpendicular to pressure. The rectangular compact sample had dimensions of $6.0 \times 6.0 \times 5.0 \text{ mm}$.

3.3.3 Sintering and Annealing

The compacts were sintered either in an argon atmosphere or in vacuum at $1030 \sim 1080 \text{ }^\circ\text{C}$ for $1 \sim 2$ hours, and then were rapidly cooled to room temperature using a water cooled Cu-block and argon gas cooling system. The vacuum was lower than 10^{-6} Torr. For optimum magnetic hardening, annealing was used in the temperature range of $500 \sim 750 \text{ }^\circ\text{C}$ for $1 \sim 2$ hours, followed by a rapid cooling of the samples down to room temperature. The sintered magnets were polished with sand-paper and cut into small pieces suitable for magnetic measurements.

3.4 Magnetic Measurement

Hysteresis loops of the samples were measured by a vibrating sample magnetometer (VSM) [1], in magnetic fields upto 80 KOe and in the temperature range $T = 300 \sim 950 \text{ K}$. A superconducting quantum interference device (SQUID, Quantum Design, Inc.) was also used to provide additional

data in the temperature range from 1.7 K to 400 K and magnetic fields upto 55 KOe. Using a small magnetic field $H \approx 100$ Oe, the transition temperatures (Curie temperatures) of the magnetic phases present were measured by the temperature dependence of the magnetization $M_H(T)$.

3.5 Microstructure and Phase Analysis

The samples were further characterized by means of X-ray diffraction, DTA and DSC, TEM and EDXA.

3.5.1 X-ray Diffraction

X-ray diffraction analysis was employed to identify the crystalline structure of the samples [56]. The d-spacings were determined by the Debye powder method using $C_r(K_\alpha)$ radiation $\lambda_{C_r} = 2.291 \text{ \AA}$. The diameter of the camera is $180/\pi$ mm. Indices (hkl) of the crystal planes were obtained by Hull-Davey chart with d-spacings.

3.5.2 DTA and DSC Analysis

Differential thermal analysis (DTA)and differential scanning calorimetry (DSC) can give some important information about phase transitions and other temperature dependent processes, which can pilot correctly sintering and annealing temperatures of the samples. DTA and DSC experiments

were made using a Dupont 1090 thermal analyzer and 910 differential scanning calorimeter equipped in a range of temperature $T = 20\text{ }^{\circ}\text{C} \sim 1200\text{ }^{\circ}\text{C}$ and $T = 20\text{ }^{\circ}\text{C} \sim 750\text{ }^{\circ}\text{C}$ at various temperature rates.

3.5.3 TEM and EDXA Analysis

A JEOL 100C scanning and transmission electron microscope (TEM) with an energy dispersive X-ray analysis (EDXA) unit was used to examine the microstructure and chemical composition of the samples. The samples were thinned by an ion thinning technique (Technics MIM IV-C Ion Thinner).

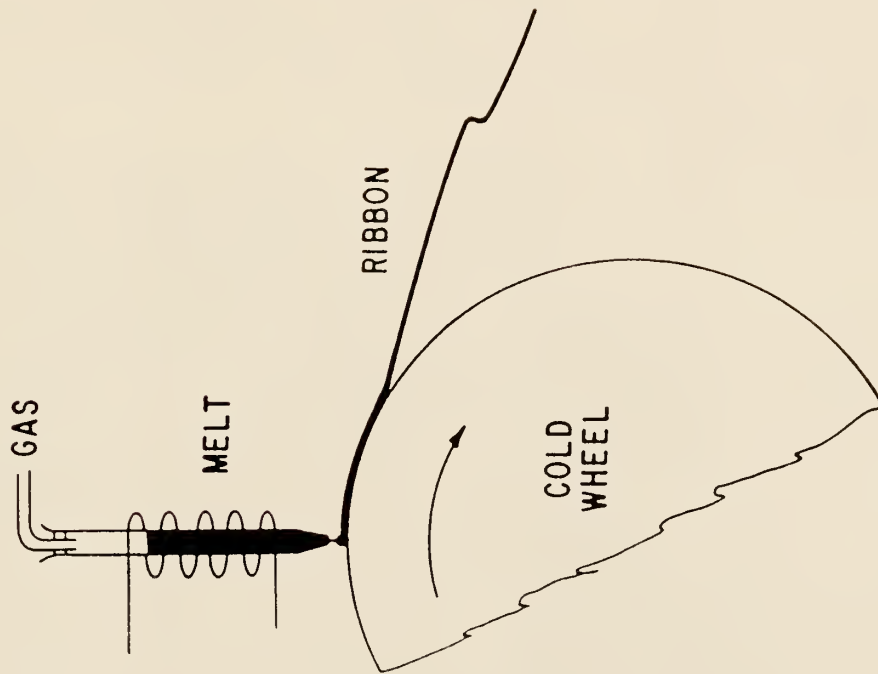


Fig. 3.1 Melt spinning technique

Chapter 4

Mm-Fe-B RIBBONS

Rapid solidification by melt-spinning produces ribbons with excellent hard magnetic properties in Nd-Fe-B [12,13,14]. The hard properties have been achieved by using both different wheel speeds and heat-treated techniques. In general, coercivity depends on the grain size of the ribbons. When the ribbons are amorphous and or microcrystalline (grain size $< 100 \text{ \AA}$), the coercivity is very small. A maximum value of coercivity can be obtained by the previously mentioned two techniques in samples with a grain size in the range from $100 \sim 2000 \text{ \AA}$. When the grain sizes are larger than 4000 \AA , the coercivity of ribbons is reduced again to the value of as-cast alloy ($H_c \approx 0.5 \text{ KOe}$). The hysteresis loops of typical Mm-Fe-B ribbons are shown in Fig. 4.1. The coercivity of the heat treated ribbons was much higher than that in amorphous ribbons. When the $Fe_{75}Al_1Mm_{14}Dy_2B_8$ ribbons were annealed at $650 \text{ }^\circ\text{C}/5 \text{ min}$, the coercivity at room temperature was increased from 0.5 KOe to 6.5 KOe

The as-quenched samples had an amorphous structure. The crystallization temperature T_{cr} obtained by DSC is in the range of $400 \sim 600 \text{ }^\circ\text{C}$ (see Fig.4.2). The Curie temperatures T_c of the ribbons were measured with themomagnetic measurements $M_H(T)$. T_c^{am} and T_c are the Curie tem-

peratures of the amorphous and crystalized ribbons, respectively. The temperature dependence of magnetization M is shown in Fig. 4.3, for $Fe_{68}Al_2Mm_{22}B_8$ ribbons, $T_c^{am} = 105^\circ C$, $T_c = 250^\circ C$.

In this chapter, the effects of alloy substitution in Mm-Fe-B magnets are discussed in an attempt to increase the system's coercivity.

4.1 Substitution of Mm for Nd in $Fe_{76}Nd_{16-x}Mm_xB_8$ Ribbons

The magnetization in a field of 16 KOe, M_s , the coercivity H_c and Curie-temperature T_c are shown as a function of misch metal concentration x in Fig. 4.4. Overall the magnetic properties are reduced by Mm substitutions in $Fe_{76}Nd_{16-x}Mm_xB_8$ alloys. The lattice constants and magnetic properties of $R_2Fe_{14}B$ single crystals are listed in table 4.1 [26,27,57]. The magnetic properties of the $La_2Fe_{14}B$ and the $Ce_2Fe_{14}B$ compounds are $M_s = 130$ and 121 emu/g, anisotropy field $H_A = 20$ and 30 KOe, $T_c = 257$ and 149 $^\circ C$, respectively. It is known that both La and Ce form tetragonal R-Fe-B compounds, but they have not orbital moment and their anisotropy is low [3]. Consequently, their magnetization and coercivity are not high as in other $R_2Fe_{14}B$ compounds.

When Mm is substituted for all Nd, the coercivity of Mm-Fe-B samples has a very low $H_c = 2.0$ KOe (see Table 4.2). It is clear that the coercivity is far too low for most permanent magnet applications. A quantitative

investigation to increasing coercivity by addition of several elements will be studied in the following sections.

4.2 Substitutions of Ni, Sn for Fe and Dy for Mm in Mm-Fe-B Ribbons

In order to improve coercivity the of Fe-Mm-B magnets, substitutions of Ni, Sn for Fe and Dy for Mm were investigated in melt-spun and heat-treated samples. The results of the substitutions of Ni and Sn are shown in Fig.4.5 and Table 4.3. In the Sn ribbon system, $Fe_{76-x}Sn_xMm_{16-d}Dy_dB_8$, the magnetic properties M_s , T_c and H_c were not changed much, even with addition of 2 at%Dy. It appears that Sn can not substitute for Fe. In the Ni ribbon system, $Fe_{76-x}Ni_xMm_{16-d}Dy_dB_8$, the coercivity was increased by Ni and Dy substitutions. For $y = 3$ and $d = 0$, $Fe_{73}Ni_3Mm_{16}B_8$ ribbons, the coercivity H_c was 5.5 KOe. A considerable increase in coercivity $\Delta H_c = 3 \sim 4$ KOe is achieved with substitutions of 2 at% Dy for Mm. For $y = 3$ and $d = 2$, in $Fe_{73}Ni_3Mm_{14}Dy_2B_8$ ribbons, the coercivity H_c was 8.4 KOe.

4.3 Substitution of Al for Fe in Mm-Fe-B Ribbons

Al was found to be effective in improving the coercivity of Mm-Fe-B magnets. Experimental data are summarized in Fig. 4.6 and Table 4.4. As it is clearly shown, the coercivity of the sample is linearly increased by Al substitutions and the magnetization M_s is reduced quickly when Al content is high ($x > 4$). Similar to the previous Ni, Sn systems, the coercivity was

increased by about $\Delta H_c = 3$ KOe with substitution of 2 at% Dy for Mn, in $Fe_{74}Al_2Mn_{14}dDy_2B_8$ ribbons; $M_s = 68.0$ emu/g, $H_c = 7.0$ KOe and $T_c = 240$ °C. This is a good example that Al and Dy substitutions increase the hard magnetic properties of ribbons at room temperature and make these alloys suitable for of permanent magnet applications.

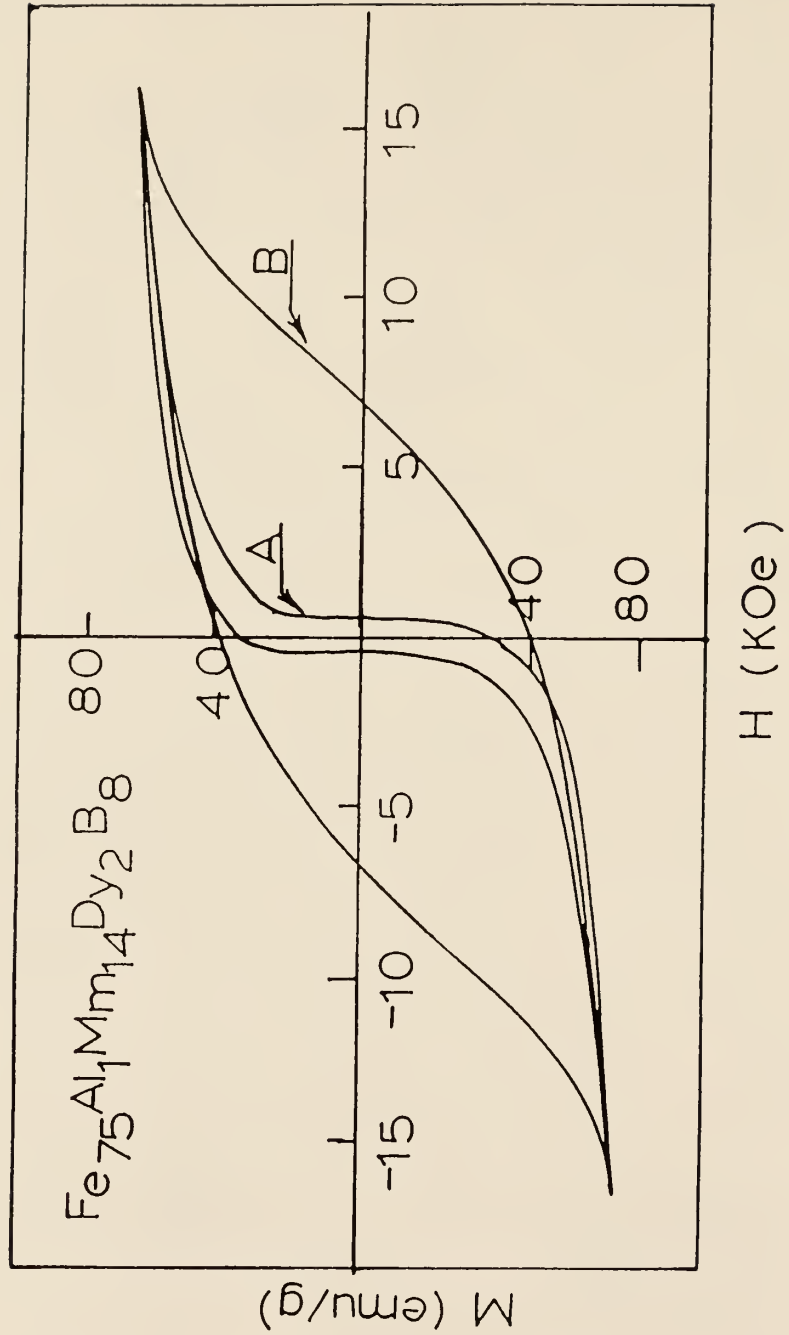


Fig. 4.1 Two hysteresis loops of typical Mm-Fe-B ribbons in the amorphous and heat-treated state. The coercivity of the heat-treated ($650\text{ }^\circ\text{C}/5\text{mins}$) ribbons was much higher than in the amorphous ribbons.

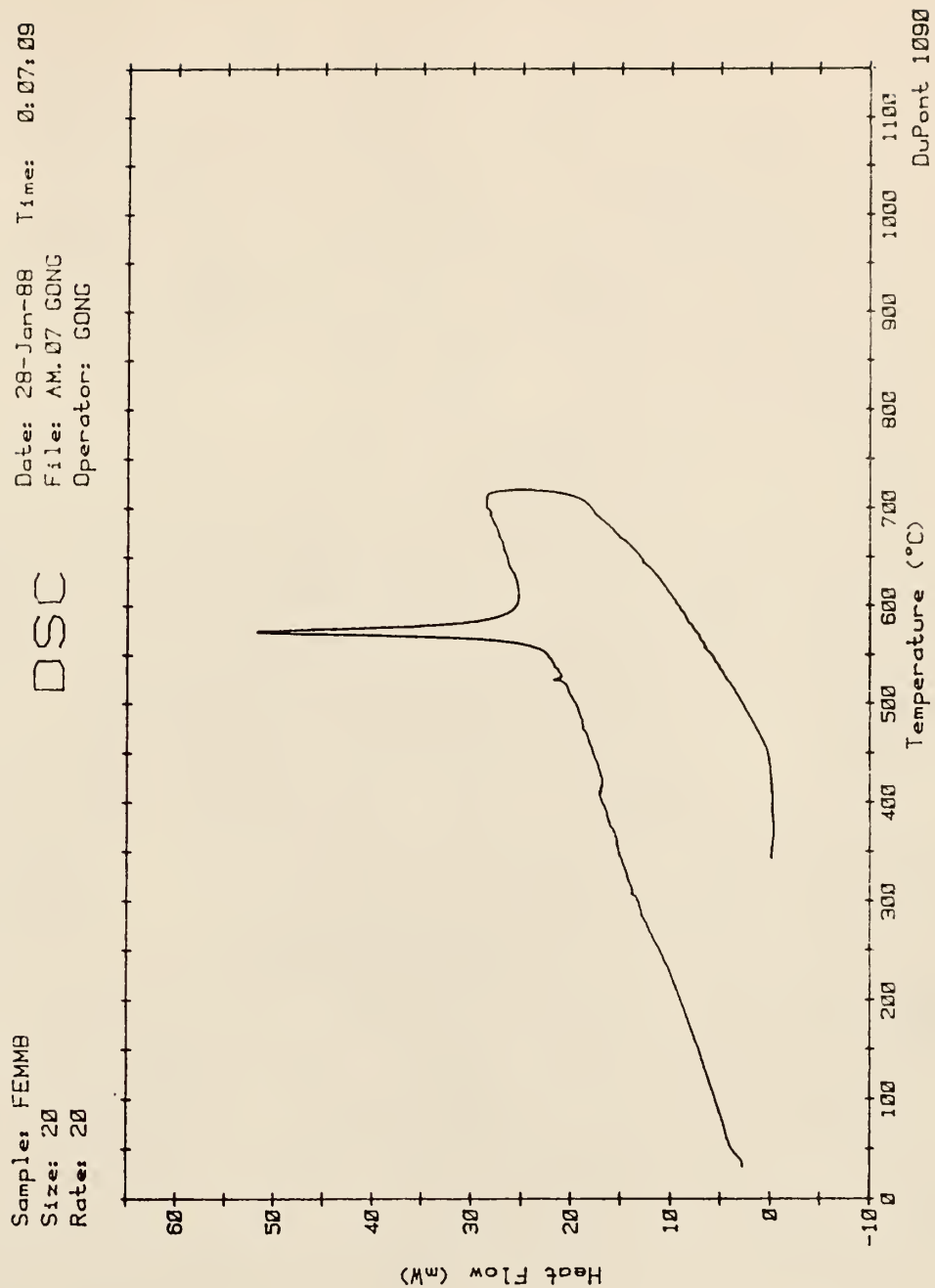


Fig. 4.2 The crystallization temperature T_{cr} of Mn-Fe-B based ribbons.

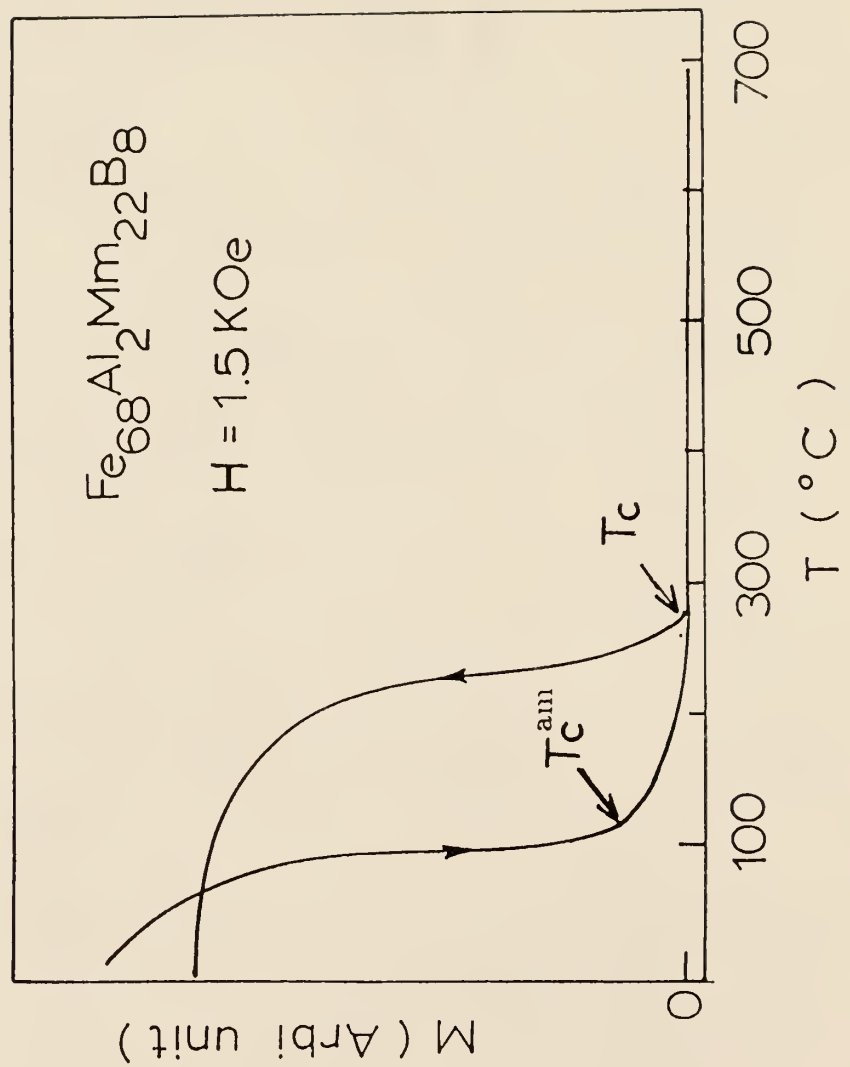


Fig. 4.3 The temperature dependence of magnetization M in a small magnetic field. T_c^{am} and T_c are Curie temperatures for the amorphous and crystalline samples.

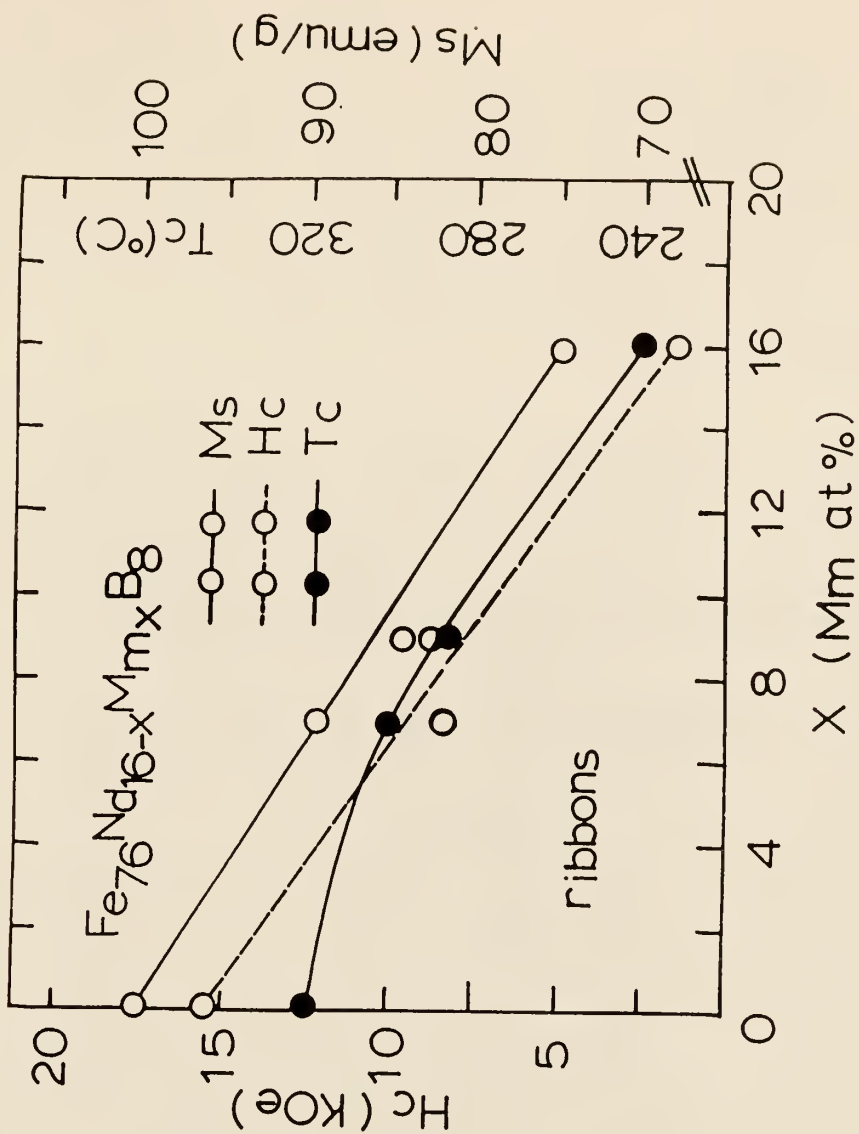


Fig. 4.4 The dependence of magnetization M_s , the coercivity H_c and the Curie temperature T_c as a function of misch metal concentration x in $Fe_{76}Nd_{16-x}Mm_xB_8$ ribbons.

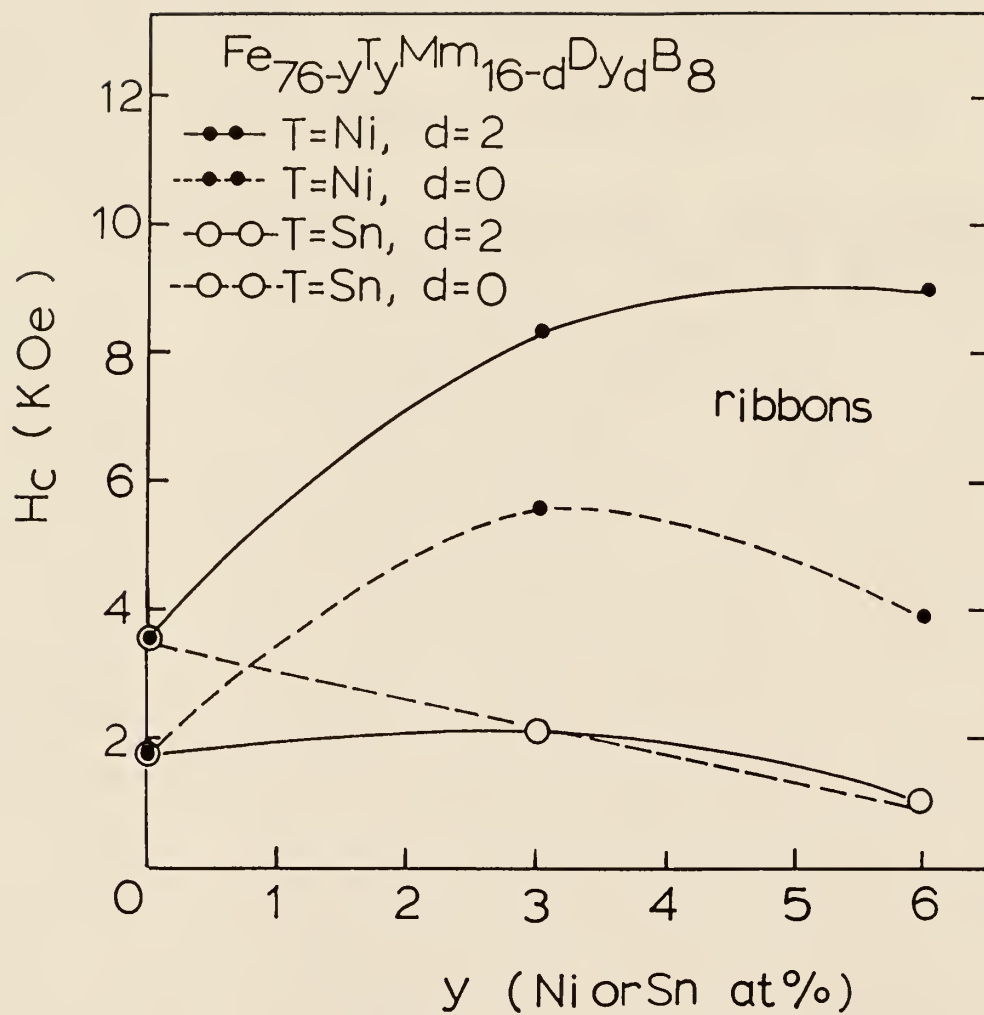


Fig. 4.5 The dependence of coercivity H_c of $Fe_{76-y}T_yMm_{16-d}Dy_dB_8$ ribbons on the contents of Ni, Sn and Dy. The detail magnetic properties are summarized in Table 4.2.

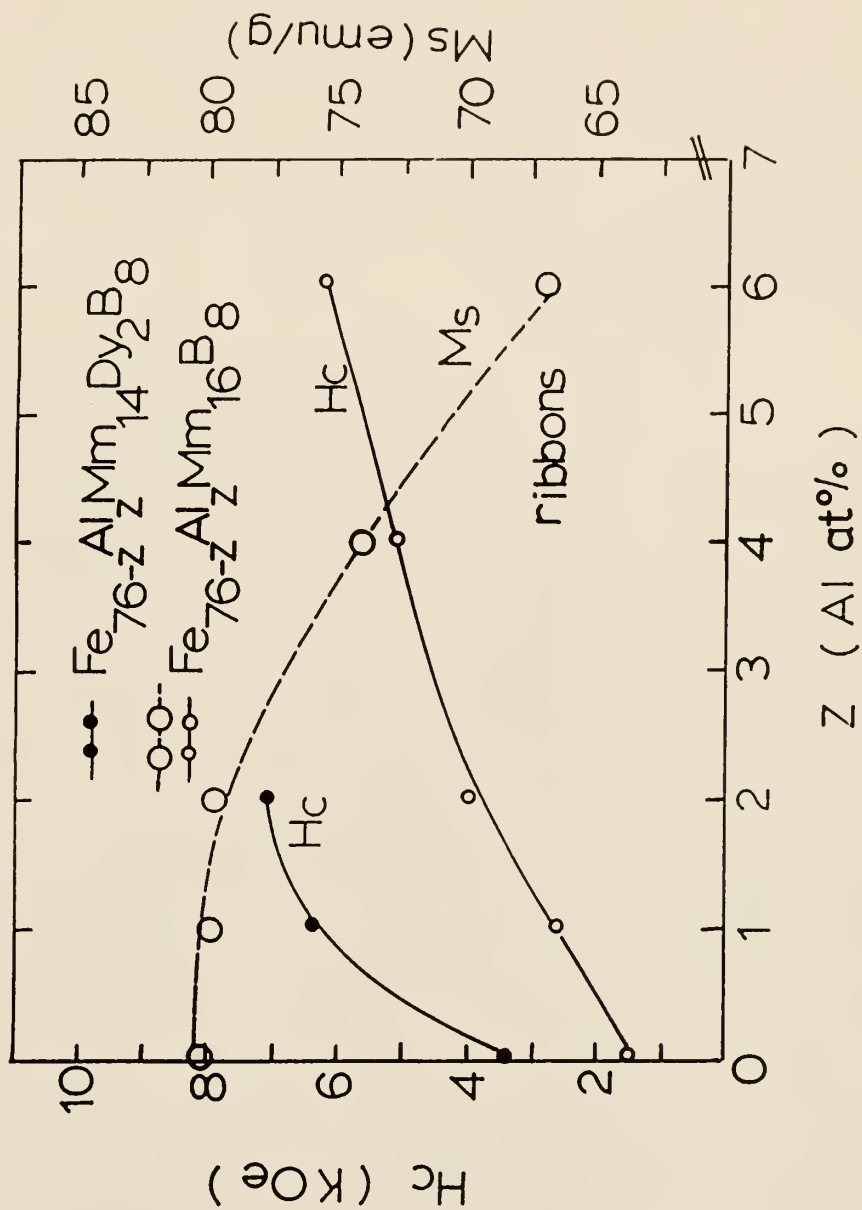


Fig. 4.6 The dependence of coercivity H_c and magnetization M_s of Mn-Fe-B based ribbons on the concentration of Al and Dy. Al was found to be beneficial for improving the coercivity. The detailed magnetic properties are summarized in Table 4.3.

R	$R_2Fe_{14}B$		M_s (emu/g)		T_c	H_A (KOe)	
	a(A°)	c(A°)	4.2 K	300 K	($^\circ C$)	4.2 K	300 K
La	8.822	12.338		130	257	30	20
Ce	8.75	12.10	152	121	149	30	30
Pr	8.81	12.27	190	165	300	320	87
Nd	8.81	12.21	194	167	315	cone	67
Dy	8.76	11.99	57	70	325	167	150

Table 4.1 Magnetic properties and structure of single phase $R_2Fe_{14}B$ ribbons.

Samples	Ribbons			Heat-treated		
	M_s	H_c	T_c^{am}	M_s	H_c	T_c
	(emu/g)	(KOe)	($^{\circ}C$)	(emu/g)	(KOe)	($^{\circ}C$)
$Fe_{76}Mm_{16}B_8$	83.1	0.4	120	75.0	1.6	240
$Fe_{76}Mm_9Nd_7B_8$	90.6	0.5	150	83.5	9.4	280
$Fe_{76}Mm_7Nd_9B_8$	100.1	0.2	150	89.0	8.2	305
$Fe_{76}Nd_{16}B_8$	117.2	0.2	150	98.5	12.2	320

Table 4.2 Magnetic properties of Mm-substituted $Fe_{76}Nd_{16-x}Mm_xB_8$ ribbons.

Samples	Ribbons			Heat-treated		
	M_s	H_c	T_c^{am}	M_s	H_c	T_c
	(emu/g)	(KOe)	($^{\circ}C$)	(emu/g)	(KOe)	($^{\circ}C$)
$Fe_{76}Mm_{16}B_8$	85.0	0.5	120	87.6	2.0	245
$Fe_{73}Ni_3Mm_{16}B_8$	90.0	0.2	200	90.0	5.5	230
$Fe_{70}Ni_6Mm_{16}B_8$	89.0	0.2	120	89.0	3.8	240
$Fe_{76}Mm_{14}Dy_2B_8$	72.4	0.1	260	72.5	3.5	260
$Fe_{73}Ni_3Mm_{14}Dy_2B_8$	81.6	0.2	120	81.6	8.4	240
$Fe_{70}Ni_6Mm_{14}Dy_2B_8$	72.0	0.2	235	72.0	9.1	255
$Fe_{73}Sn_3Mm_{16}B_8$	73.6	0.3	120	81.3	2.1	250
$Fe_{70}Sn_6Mm_{16}B_8$	68.6	0.3	240	71.1	1.3	240
$Fe_{73}Sn_3Mm_{14}Dy_2B_8$	91.4	0.3	120	91.4	1.7	240
$Fe_{70}Sn_6Mm_{14}Dy_2B_8$	67.0	0.2	290	70.7	1.2	250

Table 4.3 Magnetic properties of Mm-Fe-B ribbons with of Ni, Sn and Dy additions.

Samples	Ribbons			Heat-treated		
	M_S	H_c	T_c^{am}	M_s	H_c	T_c
	(emu/g)	(KOe)	(°C)	(emu/g)	(KOe)	(°C)
$Fe_{70}Mm_{10}B_8$	83.1	0.4	120	75.0	1.6	240
$Fe_{75}Al_1Mm_{10}B_8$	83.0	0.2	120	80.4	1.6	240
$Fe_{74}Al_2Mm_{10}B_8$	67.0	0.4	100	81.2	4.1	225
$Fe_{72}Al_4Mm_{10}B_8$	74.2	0.4	250	74.9	5.1	250
$Fe_{70}Al_6Mm_{10}B_8$	65.6	0.1	230	67.4	6.1	230
$Fe_{74}Al_2Mm_{14}Dy_2B_8$	60.0	0.2	100	67.9	7.0	240

Table 4.4 Magnetic properties of Mm-Fe-B ribbons with Al and Dy additions.

Chapter 5

Mm-Fe-B SINTERED MAGNETS

The high coercivity Mm-Fe-B alloy ribbons have a microstructure consisting of fine grains with a size in the range of $100 \text{ \AA} \sim 3000 \text{ \AA}$. Because of this it is quite evident that the magnetic properties of the ribbons are isotropic and the remanence magnetization is low, $M_r/M_s = 0.5$. Fig. 5.1 shows that the hysteresis loops of the $Nd_2Fe_{14}B$ ribbons are almost the same when the magnetic field is applied perpendicular and parallel to the ribbon plane. In order to increase the remanent magnetization M_r , powder alignment is used by the powder metallurgy method. The magnet which is made by the powder metallurgy method is called sintered magnet.

In this chapter, the three important effects of particle size, sintering and annealing on sintered magnets are reviewed in detail. Substitutions of Al, Dy and Co play important roles in Mm-Fe-B based magnets; the magnetic properties, temperature characteristics and microstructure of the magnets will be discussed.

5.1 Effect of Particle Size

The particle size is very important in achieving high coercivity. This effect is shown in Fig. 5.2, where the coercivity is plotted as a function of

milling time in sintered $Fe_{65}Al_5Mm_{22}B_8$ magnets. The optimum particle size was found to be in the range of $3 \sim 5 \mu m$ corresponding to a milling time of about 150 min. The experiment showed that the particle size for magnet fabrication is very critical. When the particle size is larger or smaller than the optimum value, the coercivity is decreased drastically.

5.2 Effect of Sintering and Annealing Temperature

The coercivity is very sensitive to the microstructure of magnet materials. When R-Fe-B magnets are sintered, the grains of $R_2Fe_{14}B$ phase are increased to about $15 \mu m$ from a powder size of $3 \sim 5 \mu m$ by the high temperature treatment which is near the melting temperature of the alloy.

The main phase $R_2Fe_{14}B$ is retained after the alloy is quenched from high temperature to room temperature. The coercivity of Mm-Fe-B magnets depends on the sintering temperature as shown in Fig 5.3. For $Fe_{71}Mm_{20.5}Al_{1.5}B_7$ magnets, the optimum coercivity was obtained by sintering temperature at $1060^\circ C$ for 1hr followed by an annealing at a temperature of $650^\circ C$ for 1hr.

When the sample was annealed at lower temperatures $600 \sim 750^\circ C$, rich R and B phases in R-Fe-B sintered magnets were found at grain boundaries. The annealing temperature is more sensitive than other manufacturing conditions. The experimental results of the coercivity dependence on annealing

temperatures are plotted in Fig. 5.4. Here all other preparation conditions were fixed except the annealing temperature. The coercivity of the samples is steeply changed by different annealing temperatures. However, the mechanism of coercivity which is related to the boundaries of $Mm_2Fe_{14}B$ and R and B rich phases is not known yet.

5.3 Al Substitution in Sintered Magnets

Additions of Al in $Fe_{70-x}Al_xMm_{22}B_8$ alloys lead to an increase in coercivity H_c and a decrease in saturation M_s , as shown in Fig. 5.5. The optimum value x is about 5 at% for both H_c and M_s . For $Fe_{70-x}Al_xMm_{22}B_8$ sintered magnets, $H_c = 6.5$ KOe, and $M_s = 65$ emu/g. G.Burzo [58] has considered the possibility that Al increases the fluidity of the Nd-rich phase during sintering, leading to a greater magnetic isolation and consequently a higher coercivity through more effective coating of the matrix grains. The resulting thinner Nd-rich phase would also be more effective in pinning the domain walls. The Al-induced compositional changes at the grain boundaries are believed to be the primary reason for the coercivity increase.

Other Al substitutions in $Fe_{65}Al_xMm_{27-x}B_8$ and $Fe_{87-x}Mm_xAl_5B_8$ sintered magnets are shown in Fig. 5.6 and Fig. 5.7. High Al substitutions at the expense of Mm resulted in a decrease of both H_c and M_s . It is shown again that the concentration of Al and Mm are very critical in producing a

reasonable magnet.

5.4 Addition of Dy_2O_3 , Nd_2O_3 and Dy in Sintered Magnets

Dy_2O_3 or Nd_2O_3 additions in the form of powders are preferred compared to metal substitution because Dy and Nd metals are expensive. The effect of Dy_2O_3 and Nd_2O_3 additions to $Fe_{68}Al_2Mm_{22}B_8$ alloys are shown in Fig. 5.8. The coercivity H_c was increased linearly and the magnetization M_s was decreased with increasing x (Dy_2O_3 or Nd_2O_3). Because of the high anisotropy field of Dy, the addition of Dy_2O_3 was more effective than Nd_2O_3 and Al in increasing the coercivity of the alloy (see Fig. 5.8). Typical hysteresis loops of the magnets are shown in Fig. 5.9. For an addition of 5 wt% Dy_2O_3 , $H_c = 10$ KOe and $M_s = 70$ emu/g.

Also like in Mm-Fe-B ribbons, the coercivity H_c is increased with partial substitution of Dy for Mm in sintered magnets. The enhancement in coercivity H_c of sintered magnets at room temperature is proportional to the amount of Dy addition and leads to an extended usable temperature range. These results are shown in Fig. 5.10 and Fig. 5.11. It is worth noticing that the magnetization M_s is increased with increasing Fe and decreasing rare earth content. For example in $Fe_{70}Mm_{22}B_8$ and $Fe_{75}Al_1Mm_{16}Dy_1B_7$ alloys, the magnetization M_s is increased from 72 to 90 emu/g while coercivity is kept high 6 ~ 7 KOe in Fig. 5.10. However, the amount of Dy in Mm-Fe-B

magnets is limited within a range of 1 ~ 3 at%. The magnetization decreases with higher Dy content because of an antiferromagnetic coupling of Dy with Fe.

5.5 Temperature Characteristics of Mm-Fe-B Magnets

The temperature dependence of magnetic properties of Mm-Fe-B based magnets are shown in Fig. 5.11 and Fig. 5.12. A very high coercivity (up to 25 KOe) was developed at the low temperature. A comparison of the results in the figures, shows that a higher coercivity is achieved with more Dy and a higher Curie temperature with more Co. The coercivities of the Mm-Fe-B magnets were reduced 35 ~ 50 Oe/°C in temperature range 20 ~ 150 °C. A smaller temperature dependence of the coercivity is found in Mm-Fe-Co-B magnets with 5 at% Co 20 ~ 25 Oe/°C in the same temperature range (see table 5.1). Hysteresis loops for a typical sample, $Fe_{75}Al_1Mm_{16}Dy_1B_7 + 5$ wt% Dy_2O_3 , are shown in Fig. 5.13. A high coercivity $H_c = 20$ KOe with magnetization $M_s = 114$ emu/g are obtained with an applied field $H = 55$ KOe at 5 K. The shape of the hysteresis loops was abnormal below 200 K, similar to Nd-Fe-B magnets showing the presence of two magnetic phases.

Curie temperatures of all the sintered magnets are summarized in Fig. 5.14 and table 5.2. The addition of 5 wt% Dy_2O_3 , 3 at% Dy and 5 at% Co in Mm-Fe-B based magnets lead to a Curie temperature increase of 15, 30,

60 °C, respectively. On the contrary, the Curie temperature was decreased by 25 °C because of addition of 5 at% Al.

5.6 Phase and Microstructure of a Mn-Fe-B Sintered Magnet

The existence of $Mm_2Fe_{14}B$ main phase in Mn-Fe-B magnets was confirmed by X-ray analysis. The lattice constants of the tetragonal $Mm_2Fe_{14}B$ phase are the same as in $Nd_2Fe_{14}B$, $a = 8.80 \text{ \AA}$ and $c = 12.21 \text{ \AA}$. Detail data for seven samples are summarized in Table 5.3. The magnetization of the $Mm_2Fe_{14}B$ is $M_s = 132 \text{ emu/g}$ at room temperature and the Curie temperature is $T_c = 250 \text{ }^\circ\text{C}$.

The grain sizes of high coercivity samples were about $10 \sim 15 \mu\text{m}$, as shown in Fig.5.15 and Fig.5.16.

DTA experimental data on Mn-Fe-B alloys showed phase transitions at temperatures around $1065 \text{ }^\circ\text{C}$ and $650 \text{ }^\circ\text{C}$, respectively (see Fig. 5.17). The transition temperatures were exactly in the range of sintering and annealing temperatures. It is an important step that suitable sintered and annealing temperatures can be found from DTA experiments for preparing high performance permanent magnets.

The transition temperature of the minor phases were changed by the addition of Al in Mn-Fe-B base magnets. For an addition of 2 at% Al in $Fe_{69}Al_2Mm_{22}B_7$ sintered magnet, the transition temperatures of minor

phases decreased by about $20 \sim 80 \text{ }^\circ\text{C}$ as shown in Fig. 5.18. The melting temperature T_m of Al is low ($T_m = 660 \text{ }^\circ\text{C}$). As in Nd-Fe-B sintered magnets, experimental evidence of domain wall pinning at grain boundary phase has been studied [2,3,4]. The effect of Al on coercivity may be the same as the effect of R-rich and B-rich phase at the grain boundaries in Mm-Fe-B sintered magnets.

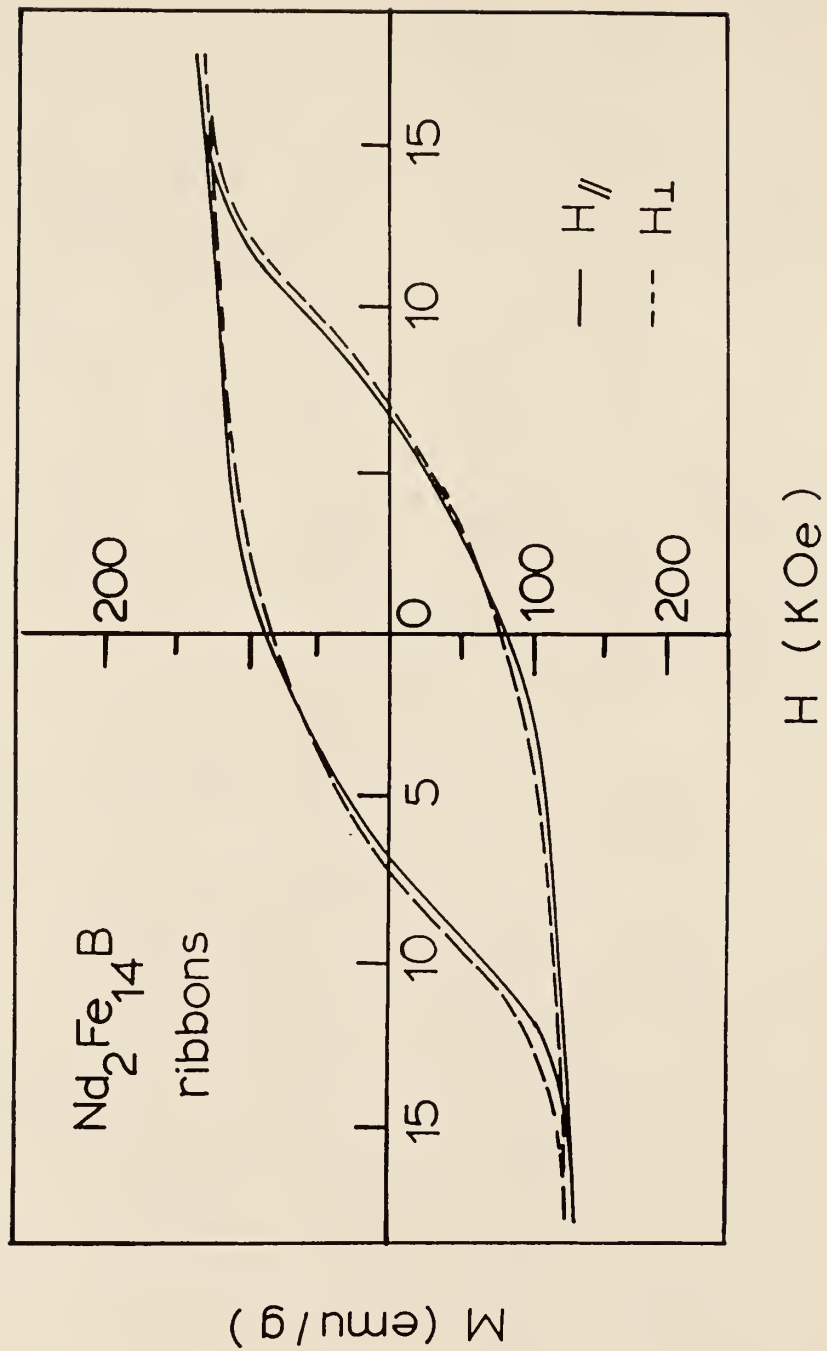


Fig. 5.1 The magnetic properties of the ribbons are isotropic. Two hysteresis loops of the $Nd_2Fe_{14}B$ ribbon were almost the same when the magnetic field was applied perpendicular and parallel to the ribbon plane.

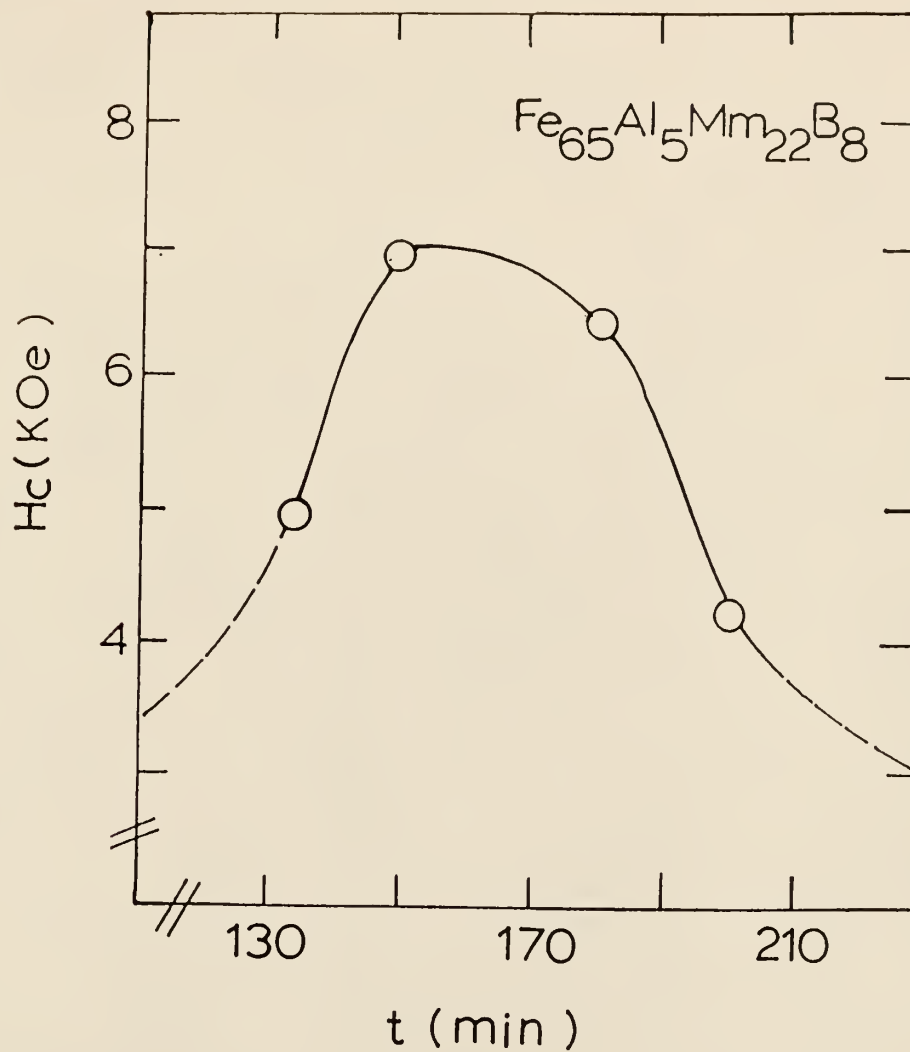


Fig. 5.2 The coercivity H_c dependence on particle size in $Fe_{68}Al_2Mm_{22}B_8$ sintered magnets. The maximum coercivity was in the range of $3 \sim 5 \mu m$ corresponding to a milling time of about 150 mins.

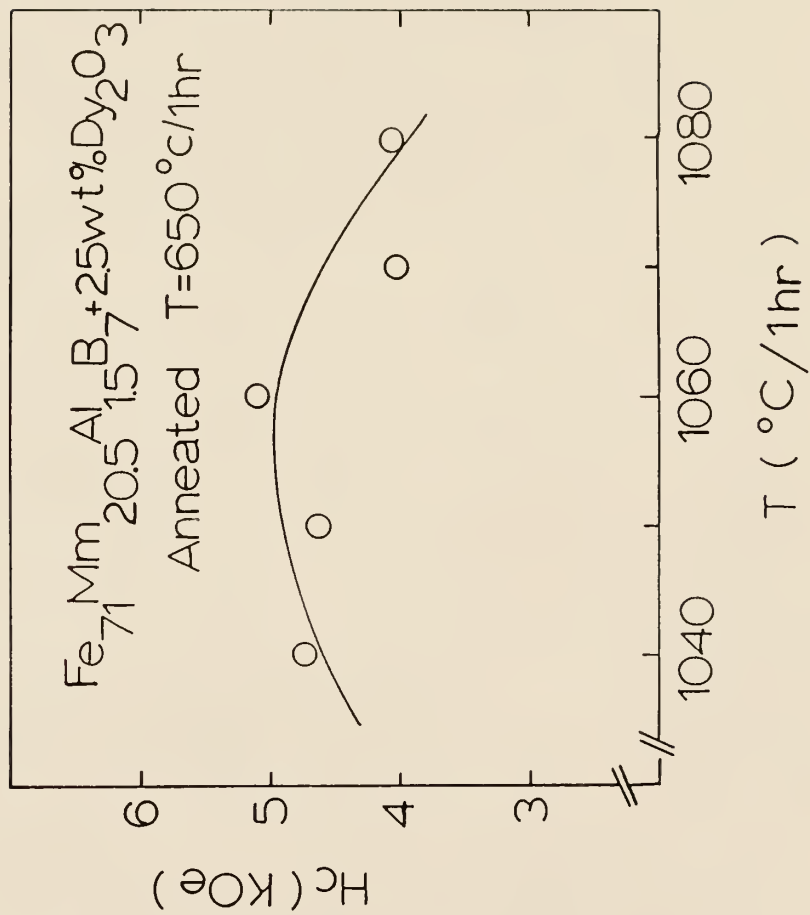


Fig. 5.3 The dependence of coercivity of Mm-Fe-B sintered magnets on the sintering temperature. Optimum coercivity was obtained at the sintering temperature of $1060^\circ\text{C}/1\text{ hr}$.

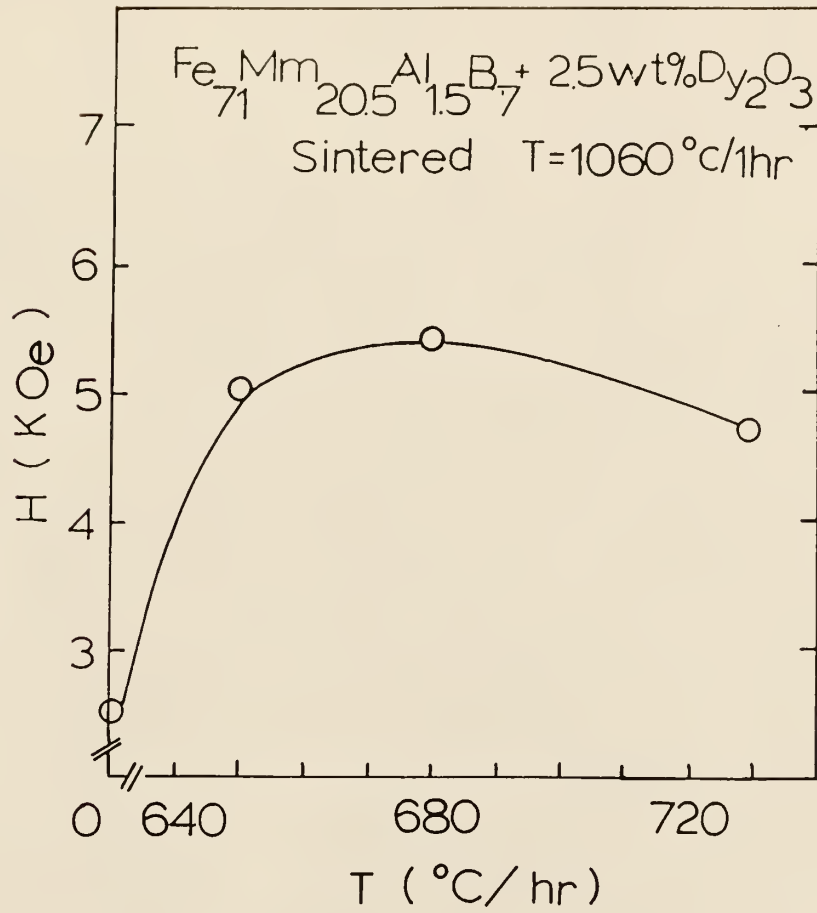


Fig. 5.4 The dependence of coercivity of Mm-Fe-B sintered magnets on the annealing temperature. The annealing temperature was more sensitive than the other of manufacturing parameters.

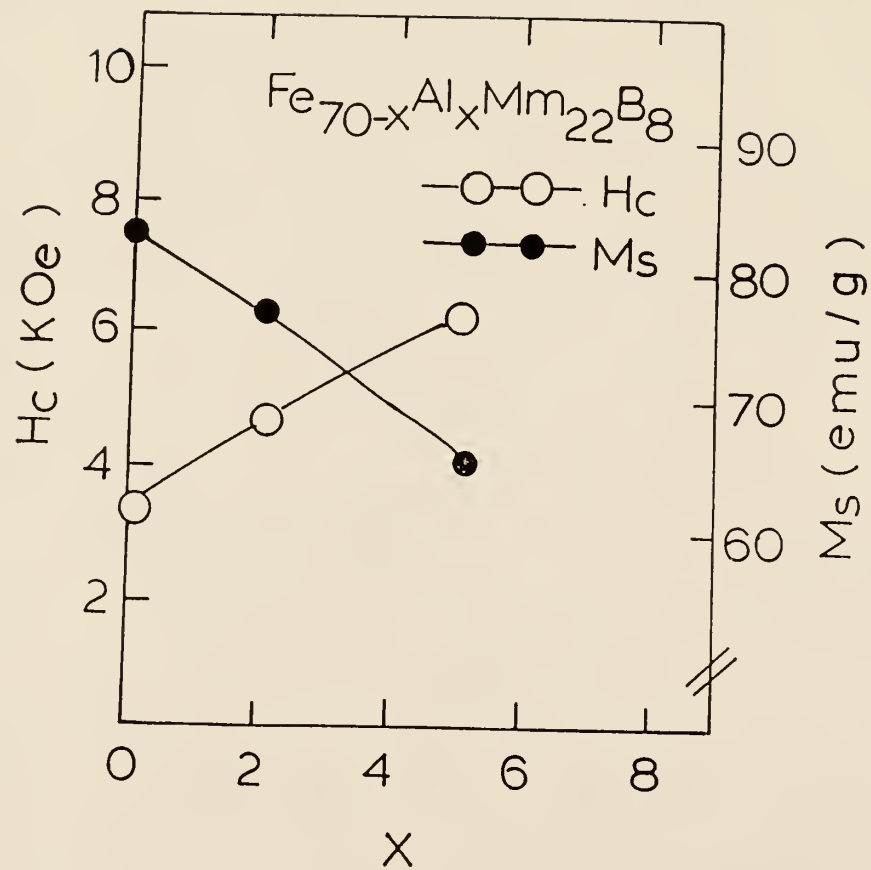


Fig. 5.5 The dependence of coercivity H_c and magnetization M_s of $Fe_{70-x}Al_xMm_{22}B_8$ sintered magnets on the concentration of Al. For a $Fe_{65}Al_5Mm_{22}B_8$ sample ($x = 5$), $H_c = 6.5$ KOe and $M_s = 65$ emu/g.

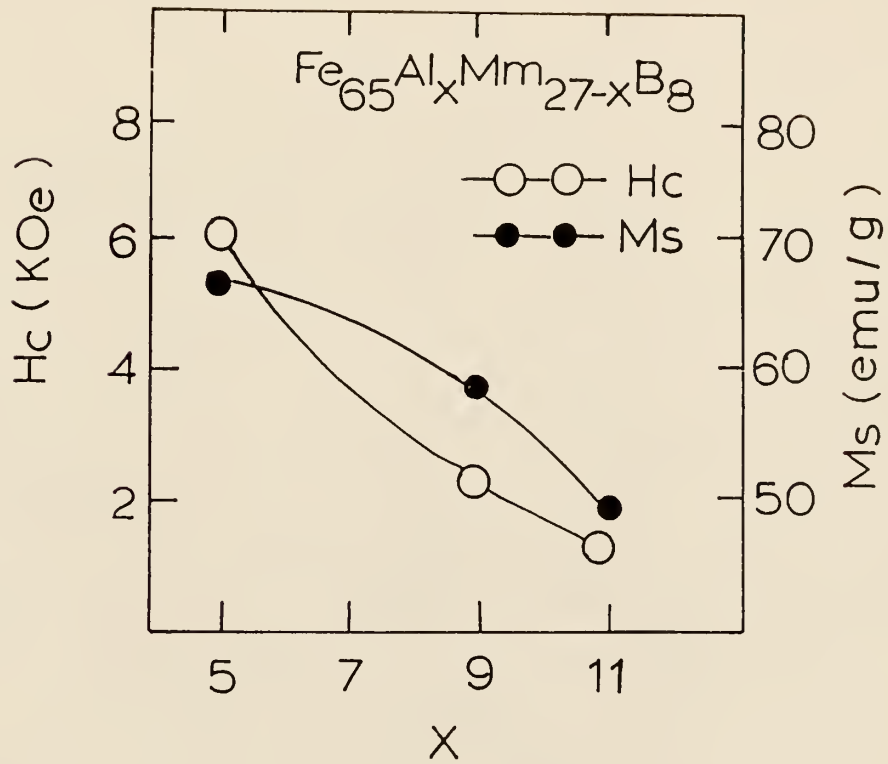


Fig. 5.6 Effect of Al substitutions for Mm in $Fe_{65}Al_xMm_{27-x}B_8$ sintered magnets.

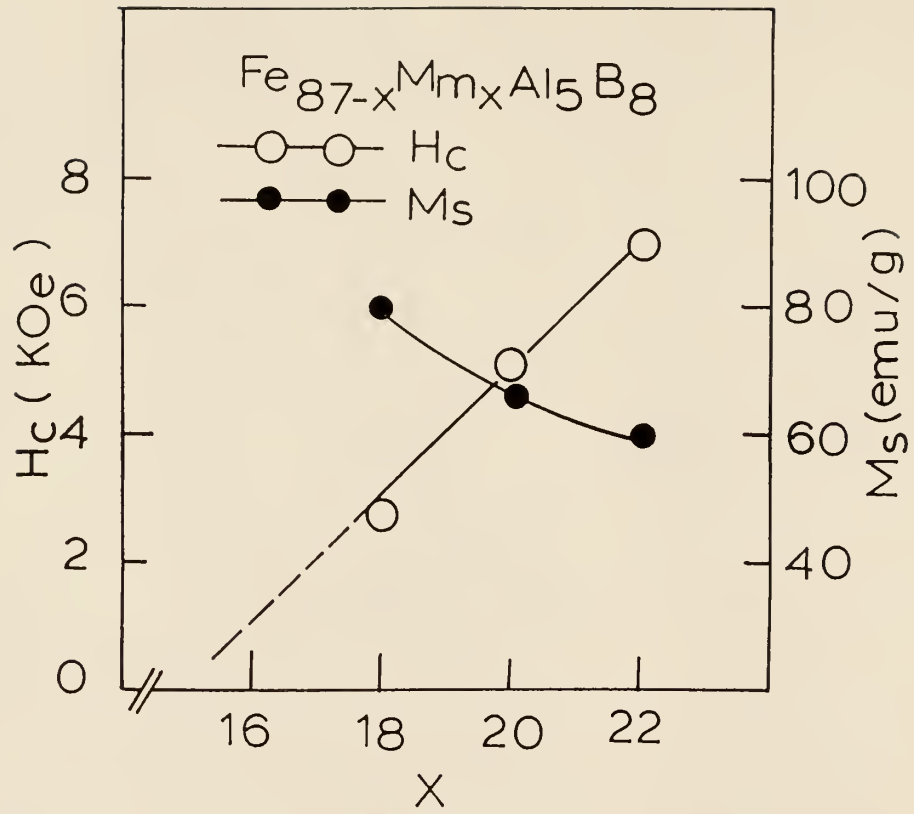


Fig. 5.7 Mm substitutions for Fe in $Fe_{87-x}Al_5Mm_xB_8$ sintered magnets.

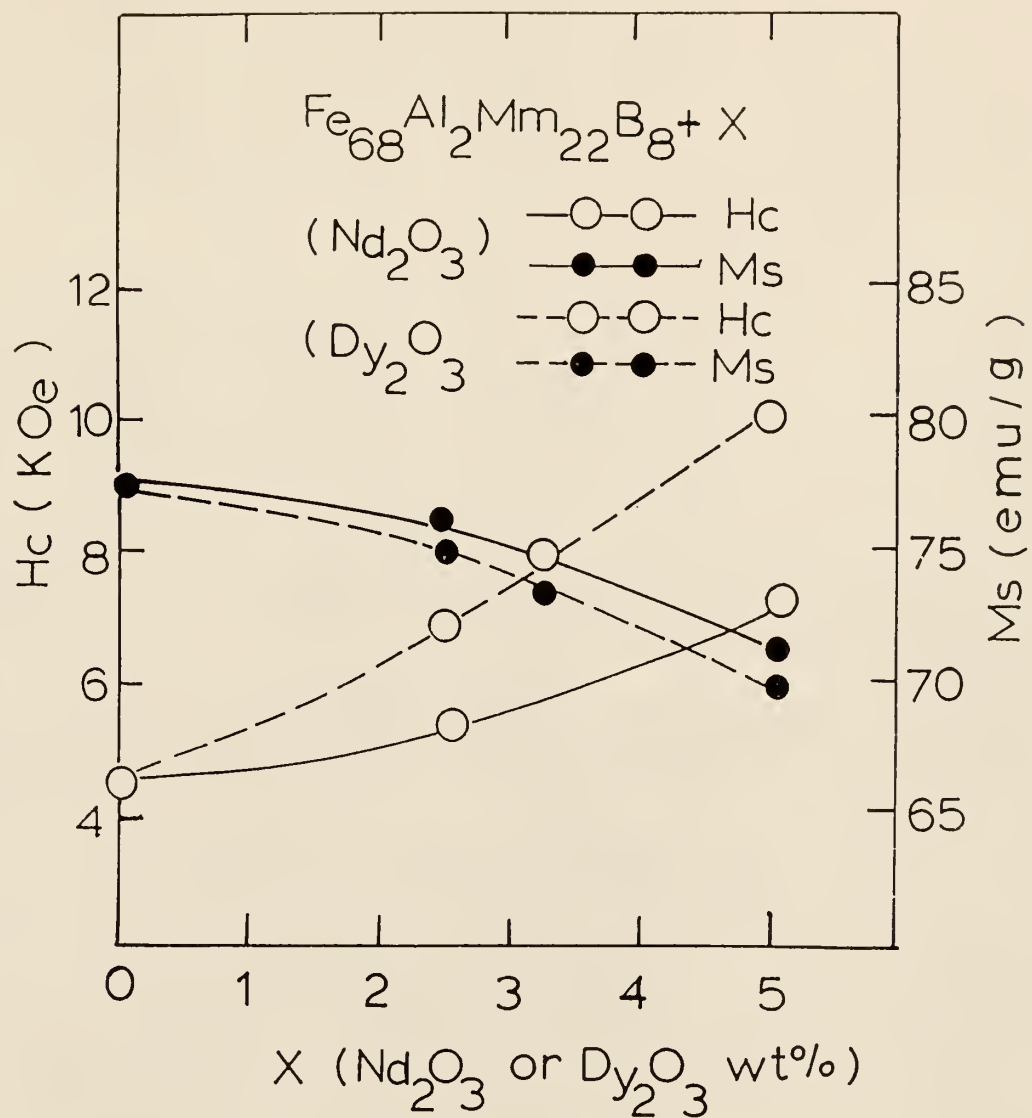


Fig. 5.8 The magnetic properties of Mm-Fe-B sintered magnets with additions of Dy_2O_3 and Nd_2O_3 powders.

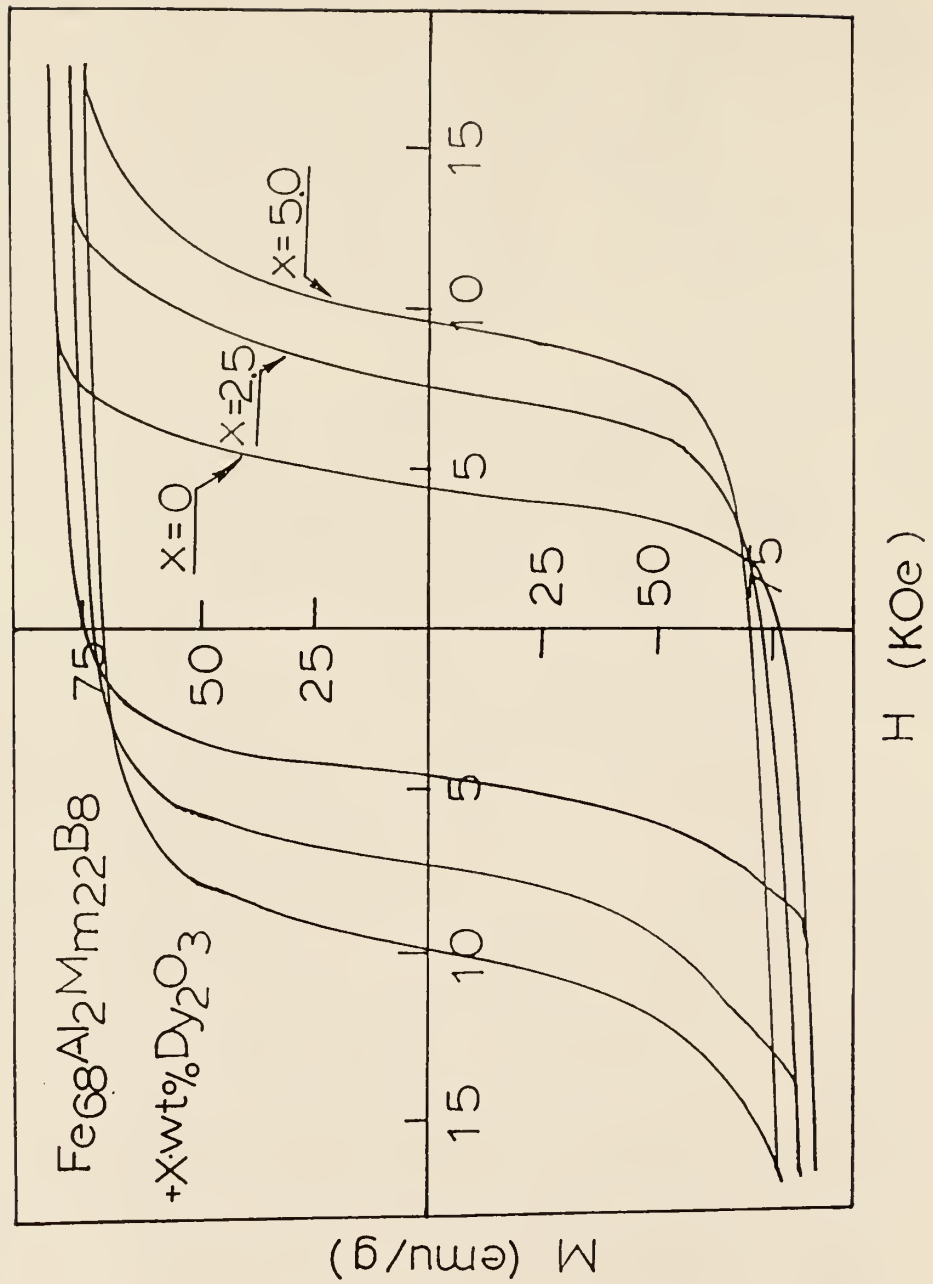


Fig. 5.9 The hysteresis loops of the $Fe_{68}Al_2Mm_{22}B_8$ with x wt% Dy_2O_3 sintered magnets. For $x = 5$, $H_c = 10$ KOe and $M_s = 70$ emu/g.

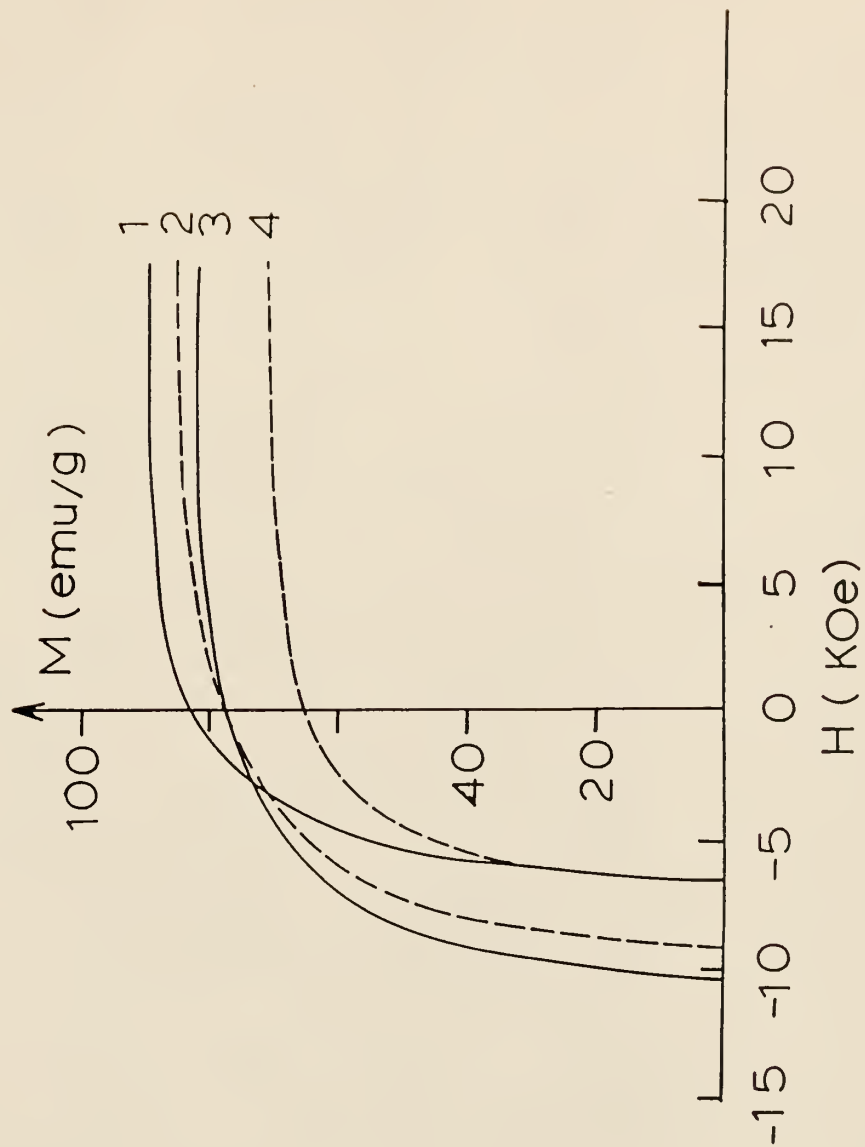


Fig. 5.10 Magnetization curves of several sintered magnets.

1. $Fe_{75}Al_1Mm_{16}Dy_1B_7 + 5 \text{ wt}\% Dy_2O_3$,
2. $Fe_{75}Al_1Mm_{15}Dy_2B_7 + 3.5 \text{ wt}\% Dy_2O_3$.
3. $Fe_{75}Mm_{15}Dy_3B_7 + 3.55 \text{ wt}\% Dy_2O_3$,
4. $Fe_{70}Mm_{22}B_8 + 5 \text{ wt}\% Dy_2O_3$.

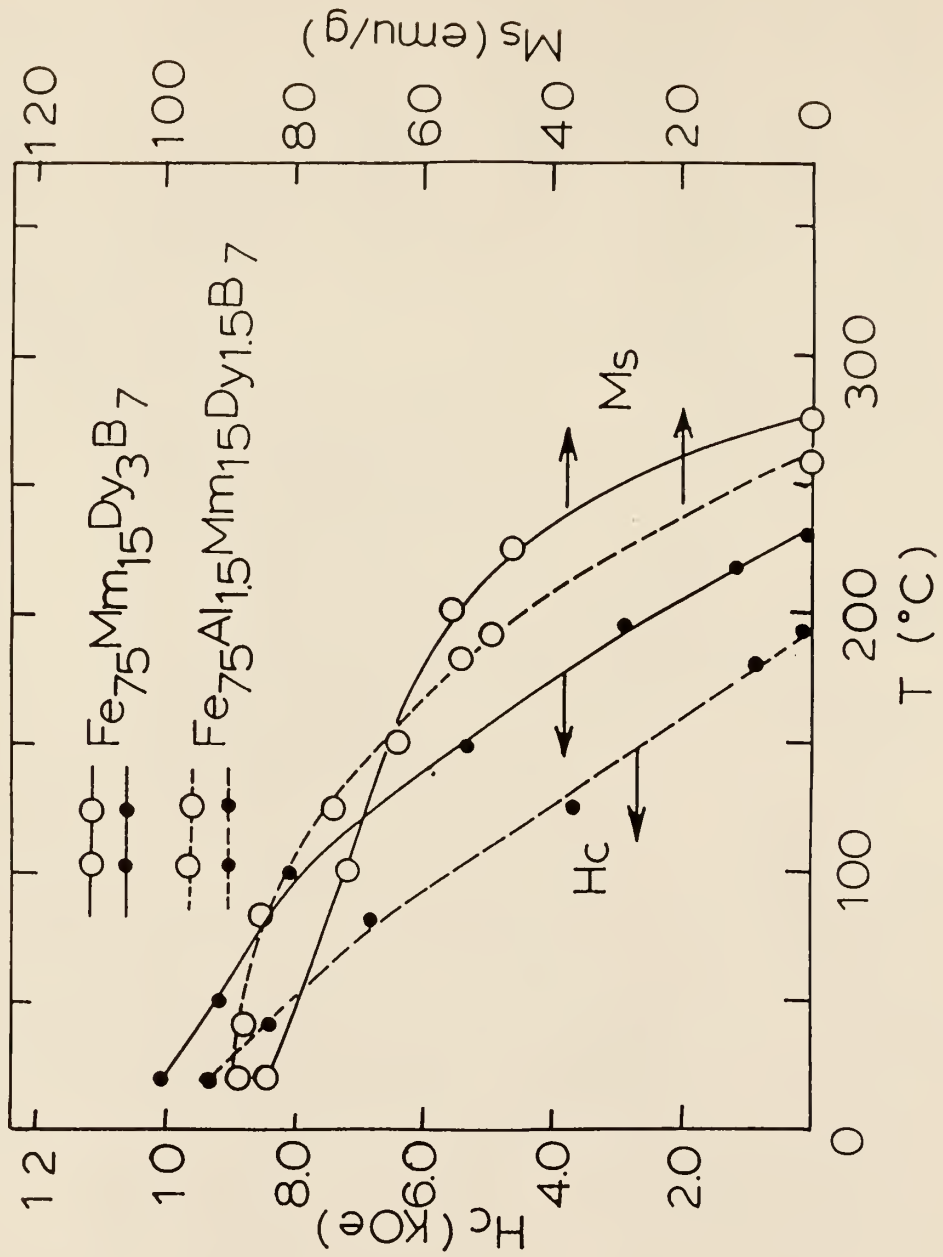


Fig. 5.11 The temperature dependence of coercivity H_c and magnetization M_s for $Fe_{75}Al_1Mm_{16}Dy_1B_7$ and $Fe_{75}Al_{1.5}Mm_{15}Dy_{1.5}B_7$ sintered magnets.

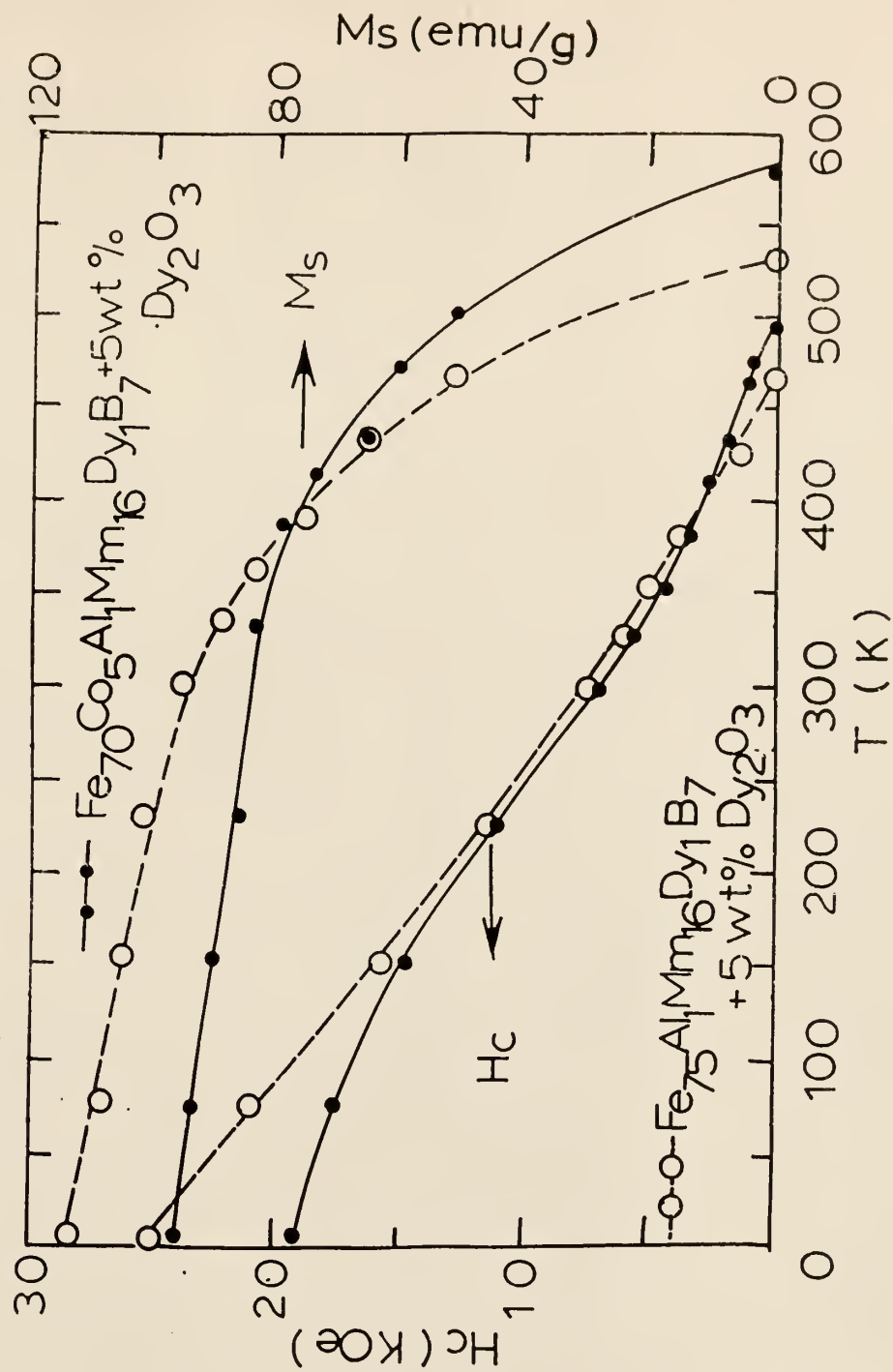


Fig. 5.12 The temperature dependence of coercivity H_c and magnetization M_s for $Fe_{70}Co_5Al_1Mm_{16}Dy_1B_7 + 5\text{ wt}\% Dy_2O_3$ and $Fe_{75}Al_1Mm_{16}Dy_1B_7 + 5\text{ wt}\% Dy_2O_3$ sintered magnets.

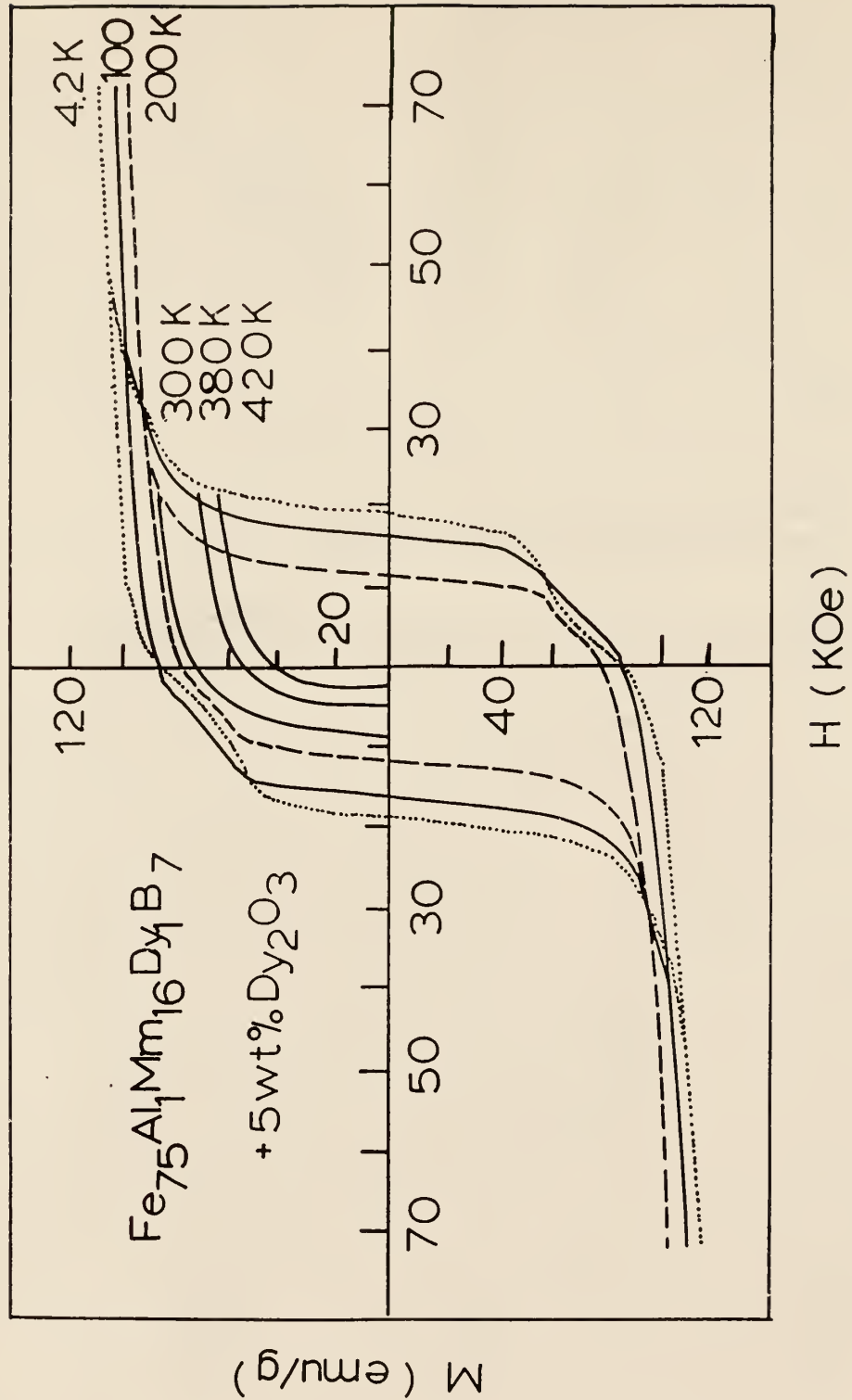


Fig. 5.13 Hysteresis loops of $Fe_{75}Al_xMm_{16}Dy_1B_7 + 5 \text{ wt}\% Dy_2O_3$ sintered magnets at different temperatures.

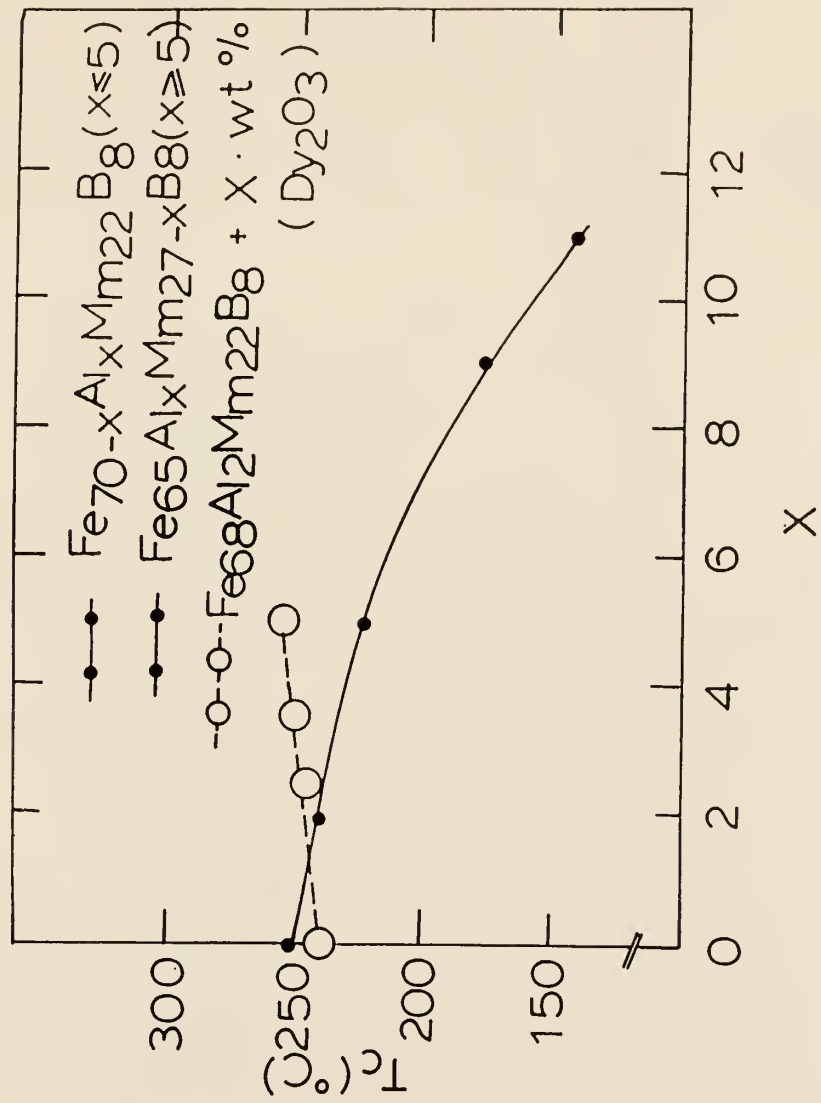


Fig. 5.14 The Curie temperature of Mm-Fe-B based sintered magnets.

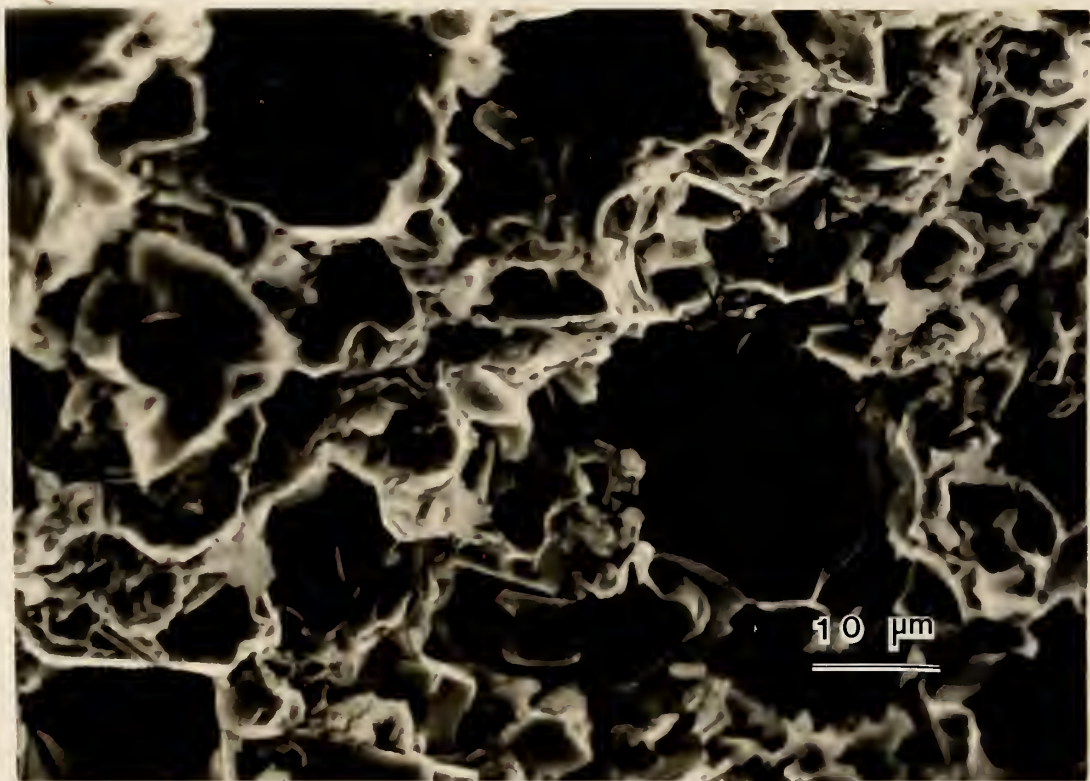


Fig. 5.15 The grain size of the $Fe_{68}Al_2Mm_{22}B_8$ sintered magnets.

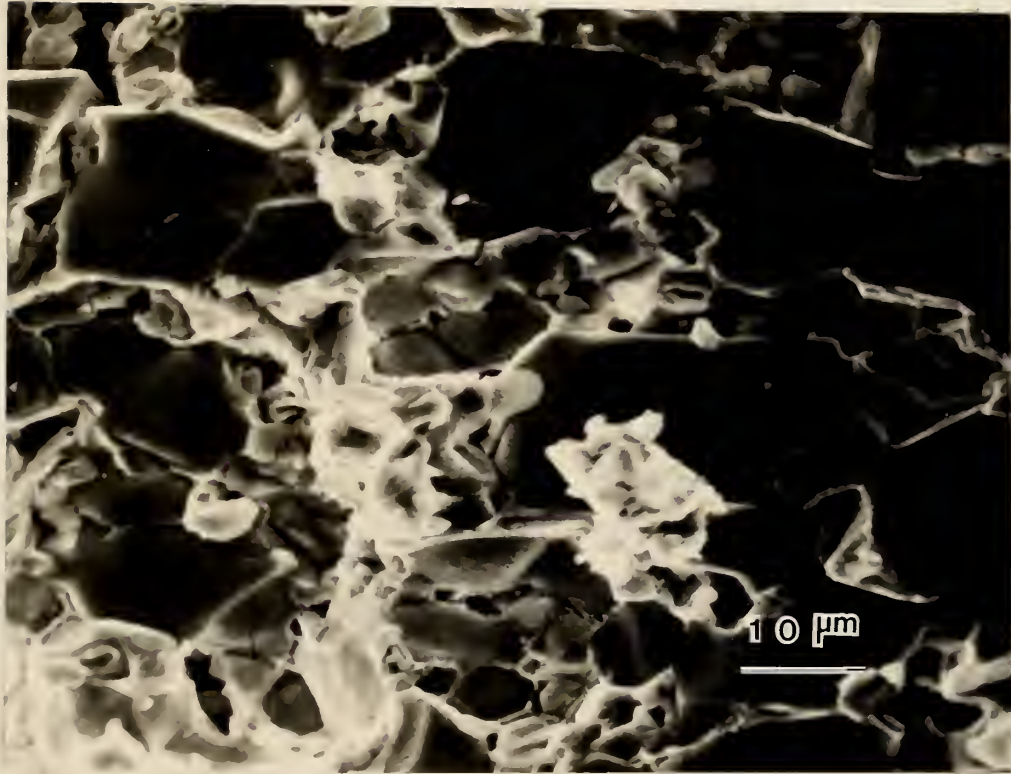


Fig. 5.16 The grain size of the $Fe_{75}Al_2Mm_{16}Dy_1B_7 + 5 \text{ wt\% } Dy_2O_3$ sintered magnets.

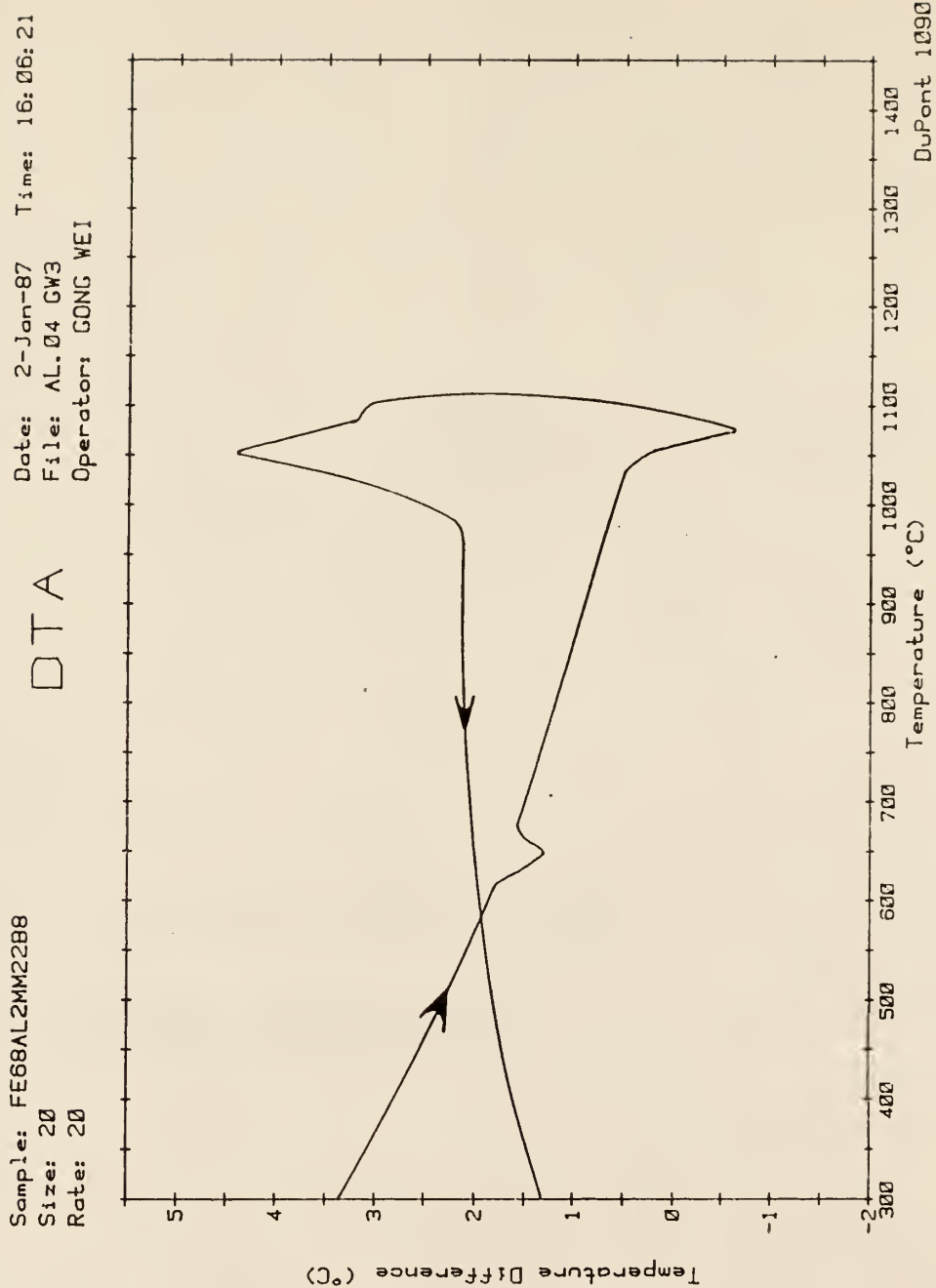


Fig. 5.17 DTA analysis of the $Fe_{68}Al_2Mm_{22}Dy_1B_8$ sintered magnets. The transition temperature of the $Mm_2Fe_{14}B$ and R-rich phase were $1065\text{ }^{\circ}C$ and $650\text{ }^{\circ}C$, respectively.

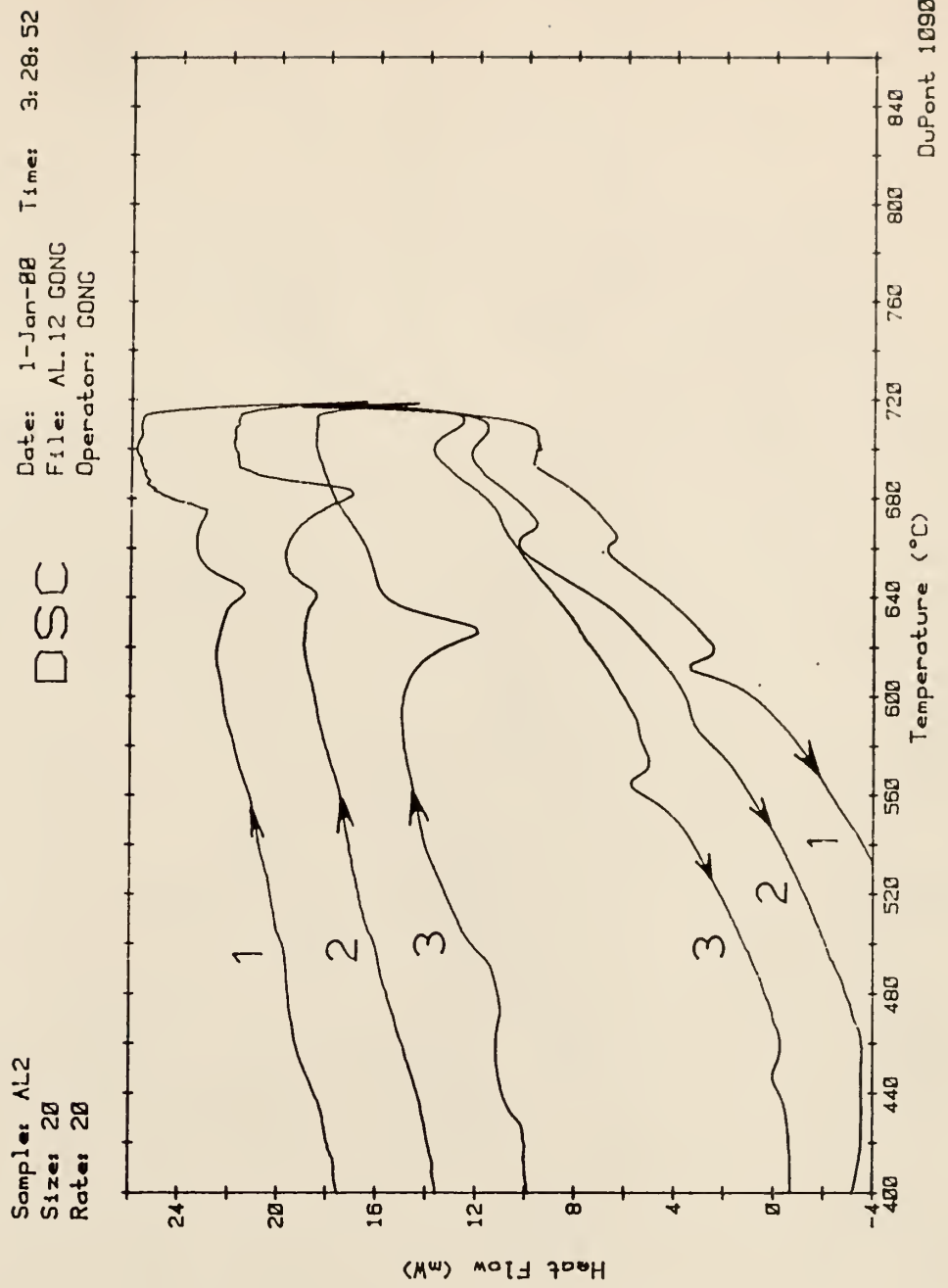


Fig. 5.18 DSC analysis of the Mm-Fe-B sintered magnets.

1. $Fe_{70}Mm_{22}B_8$,
2. $Fe_{75}Mm_{15}Dy_3B_7 + 3.5 \text{ wt}\% Dy_2O_3$.
3. $Fe_{68}Al_2Mm_{22}B_8$.

Samples	Dy_2O_3	T_c	M_s	H_c	$\alpha = \Delta H_c / \Delta T$
	(wt%)	($^{\circ}C$)	(emu/g)	(KOe)	(Oe/ $^{\circ}C$)
$Fe_{75}Al_1Mm_{16}Dy_1B_7$	5	250	89.0	6.3	38
$Fe_{75}Al_{1.5}Mm_{15}Dy_{1.5}B_7$	4	265	87.0	8.1	47
$Fe_{75}Mm_{15}Dy_3B_7$	3.5	275	8.4	10.1	36
$Fe_{70}Co_5Mm_{16}Dy_1B_7$	5	320	86.0	6.0	25
$Fe_{70}Co_5Mm_{17}Dy_1B_7$	5	325	86.0	5.0	20

Table 5.1 Magnetic properties of Mm-Fe-B sintered magnets.

ND2					A1	A2	A3	A4	A5	A6	A7
θ°	I	$1/D^2$ exp.	hkl	$1/D^2$ th	θ°	θ°	θ°	θ°	θ°	θ°	θ°
20.45	M	0.0930	212	0.0914	21.1	21.1	21.0	20.8	20.8	20.8	20.75
22.75	W	0.1140	221	0.1100	23.3	23.3	23.0	23.3	23.3	23.3	23.55
25.25	S	0.1386	311	0.1358	25.2	25.1	25.6	25.3	25.3	25.5	25.55
27.65	M	0.1641	223	0.1636	26.9	27.1	27.0	26.8	26.8	26.8	26.65
28.75	S	0.1763	214	0.1719	28.9	28.9	28.7	28.7	29.1	29.0	28.85
29.75	M	0.1877	105	0.1806	29.9	29.6	29.5	29.5	29.8	29.8	29.75
30.55	S	0.1969	313	0.1895	30.6		30.2				30.55
32.15	W	0.2145	224	0.2106	31.8		32.0				31.75
32.75	S	0.2229	410	0.2195	33.1	33.1	33.0	33.0	33.0	32.9	32.95
34.25	S	0.2414	411	0.2262	34.4	34.3	34.4	34.5	34.5	34.5	34.55
37.75	S	0.2856	324	0.2751	38.1	38.1	37.8	38.1	38.1	38.0	37.75
40.45	W	0.3208	404	0.3139	42.1		39.0				
42.55	W	0.3484	325	0.3357	42.1			41.8	41.8	41.7	42.55
45.55	M	0.3884	415	0.3872	46.1	46.1	45.5	45.5	45.8		
46.75	M	0.4043	513	0.3961	46.6	46.8	46.5	46.7	46.8	47.8	
50.75	M	0.4570	514	0.4430				50.0	50.0		
51.25	S	0.4635	317	0.4578		51.3		51.0	51.3	51.0	49.65
53.25	M	0.4892	208	0.4809				53.5			
54.75	M	0.5082	515	0.5034	54.1	54.1	54.8	54.5	54.8	54.5	
56.25	M	0.5268	444	0.5205	55.1	55.1				56.0	
58.25	M	0.5510	534	0.5464	58.1	58.1	61.0	58.0	58.3	58.0	
60.75	M	0.5801	516	0.5722	61.1	61.1	61.0	61.0	61.3	60.7	

Table 5.2 The existence of $Mm_2Fe_{14}B$ main phase was confirmed by x-rays.

$a = 8.80 \text{ \AA}$ and $c = 12.21 \text{ \AA}$.

$$Nd_2 = Nd_2Fe_{14}B, \quad A_1 = Fe_{70}Mm_{22}B_8,$$

$$A_2 = Fe_{68}Al_2Mm_{22}B_8, \quad A_3 = Fe_{65}Al_5Mm_{20}B_8,$$

$$A_4 = Fe_{68}Al_9Mm_{20}B_8, \quad A_5 = Fe_{68}Al_2Mm_{22}B_8 + 5 \text{ wt\% } Dy_2O_3,$$

$$A_6 = Fe_{73}Mm_{20}B_7, \quad A_7 = Fe_{75}Mm_{15}Dy_3B_7 + 3.5 \text{ wt\% } Dy_2O_3.$$

Chapter 6

SINGLE PHASE $R_2Fe_{14}B$ POWDERS AND RIBBONS

The single domain particle size $D_s = 1.4 \gamma/M_s^2$ is calculated to be 0.3 μm for Nd-Fe-B, where the domain wall energy is $\gamma = 35 \text{ erg/cm}^2$ and magnetization $M_s = 1280 \text{ G}$ [59]. Sintered Nd-Fe-B magnets typically have grain diameters $D = 5 \sim 15 \mu m$ [60] and rapidly solidified magnets have $D = 200 \sim 800 \text{ \AA}$ [13]. Thus, $D \gg D_s$ for sintered magnets and $D \ll D_s$ for rapidly solidified magnets.

Sintered Nd-Fe-B magnets have several domains per grain ($D \gg D_s$) in the thermally demagnetized state. The domain walls move easily inside the grains and the coercivity increases markedly with increasing magnetic field. The coercivity of sintered magnets is attributed to "localized domain wall pinning" otherwise referred to as "nucleation" (see section 5.6). In rapidly solidified magnets with the fine grained microstructure, it is more difficult to separate the nucleation and pinning models of coercivity .

In this chapter, the average particle size of powder samples was about 1 $\sim 5 \mu m$ using ball milling. The ribbon samples were made by melt-spinning using an optimum wheel speed $v = 20 \sim 40 \text{ m/s}$. The average grain size is $D = 600 \text{ \AA}$ and 800 \AA for $Nd_2Fe_{14}B$ and $Dy_2Fe_{14}B$ ribbons, respectively (see Fig. 6.1 and Fig. 6.2).

To understand better the coercivity mechanism in R-Fe-B magnets, the magnetic properties of single phase $R_2Fe_{14}B$ powders and ribbons have been studied using initial magnetization curves, dependence of coercivity on particle size and magnetic field and temperature.

6.1 $Mm_2Fe_{14}B$ Powders and Ribbons

The anisotropy field H_A of the $Mm_2Fe_{14}B$ was measured by the intersection of two magnetization curves obtained with the applied field parallel and perpendicular to the aligned direction of the powder. $H_A = 40$ KOe at room temperature. The uniaxial anisotropy constant K is obtained from $K = M_s H_A / 2$; $K = 1.93 \times 10^7$ erg/cm³ (see Fig. 6.3).

Using formulas (2.8) and (2.10), the anisotropy constants K_1 and K_2 were determined by plotting M_H^2 versus H/M_H , $K_1 = 1.39 \times 10^6$ erg/cm³, $K_2 = 7.18 \times 10^6$ erg/cm³ and $K = K_1 + 2K_2 = 1.58 \times 10^7$ erg/cm³. The results are shown in Fig. 6.4. The uniaxial anisotropy constants K obtained from the two methods are almost the same.

Using melt-spinning with optimum wheel speed 35 m/s, the coercivity H_c and magnetization M_s of the $Mm_2Fe_{14}B$ ribbons were $H_c = 2.0$ KOe, $M_s = 132$ emu/g at 300 K and $H_c = 4.0$ KOe and $M_s = 142$ emu/g at 5 K.

6.2 Nd₂Fe₁₄B Powders and Ribbons

The dependence of coercivity H_c'' , H_c^\perp and the ratio $\alpha = M_r/M_s$ on particle size in Nd₂Fe₁₄B powders are shown in Fig. 6.5; here H_c'' and H_c^\perp is the coercivity with applied field parallel and perpendicular to the aligned direction of the powder, respectively. D is an average powder particle size taken from SEM pictures. The critical single domain size of Nd₂Fe₁₄B samples can be found and is estimated to be 0.3 μm from the intersection of H_c'' and H_c^\perp curves in Fig. 6.5. This value is in agreement with the theoretical calculations. The coercivity H_c is 3 ~ 4 KOe and the anisotropy field $H_A = 60$ KOe at room temperature and $H_c = 9 \sim 10$ KOe at 5K.

The dependence of coercivity H_c in Nd-Fe-B ribbons on grain size is shown in Fig. 6.6. The maximum coercivity $H_c = 8$ KOe and 15 KOe for Nd₂Fe₁₄B and Nd₁₅Fe₇₇B₈, respectively, were obtained by annealing at 700 °C for 30 minutes with an average grain size $D = 600$ Å. The coercivity of the samples decreased with larger grain size at higher annealing temperatures. Corresponding to the definition in Fig.2.3, the critical diameter of the single domain D_s is $D_s = 600$ Å for Nd-Fe-B ribbons. Fig. 6.7 shows the temperature dependence of coercivities and hysteresis loops in Nd₂Fe₁₄B ribbons. The Nd₂Fe₁₄B ribbons maintained a high coercivity at low temperature, which is different from Nd₁₅Fe₇₇B₈ ribbons. A probable reason is the Nd₂Fe₁₄B sample has only one phase.

6.3 Dy₂Fe₁₄B Powders and Ribbons

The existence of high coercivity in $Dy_2Fe_{14}B$ powders is shown in Fig. 6.8 with $H_c = 22$ KOe at room temperature. The coercivities and hysteresis loops of $Dy_2Fe_{14}B$ ribbons depend strongly on temperature. The magnetic structure of $Dy_2Fe_{14}B$ was studied by neutron diffraction [61]. It was confirmed that all magnetic moments lie in the c-direction with Dy and Fe being coupled antiparallel. Consequently, the samples have very high magnetocrystalline anisotropic field, $H_A = 150$ KOe at 300 K (see Table 4.1), and were not saturated by applied fields up to $H = 72$ KOe. The coercivity H_c of the ribbons was at least higher than 40 KOe as shown in Fig. 6.9.

6.4 Coercivity Mechanism

The initial curves and hysteresis loops of the $R_2Fe_{14}B$ ($R = Nd, Dy$) powders and ribbons at room temperature are put together in Fig. 6.10. The powder particles samples were not aligned. The initial curve of the $Nd_2Fe_{14}B$ ribbons was different from other samples. This is a typical curve for uniform domain wall pinning.

In $Nd_2Fe_{14}B$ and $Dy_2Fe_{14}B$ ribbons, the coercivity of the ribbons was slowly increased with field at small applied fields $H < H_{cr}$. But when $H > H_{cr}$, the coercivity of the ribbons was quickly increased by the high field (see Fig. 6.11 and Fig. 6.12). It is clear that the coercivity of the $R_2Fe_{14}B$ ($R =$

Nd, Dy) ribbons is controlled by domain wall pinning. On the contrary, the coercivity of the $R_2Fe_{14}B$ ($R = Nd, Dy$) powders is controlled by nucleation or localized domain wall pinning.

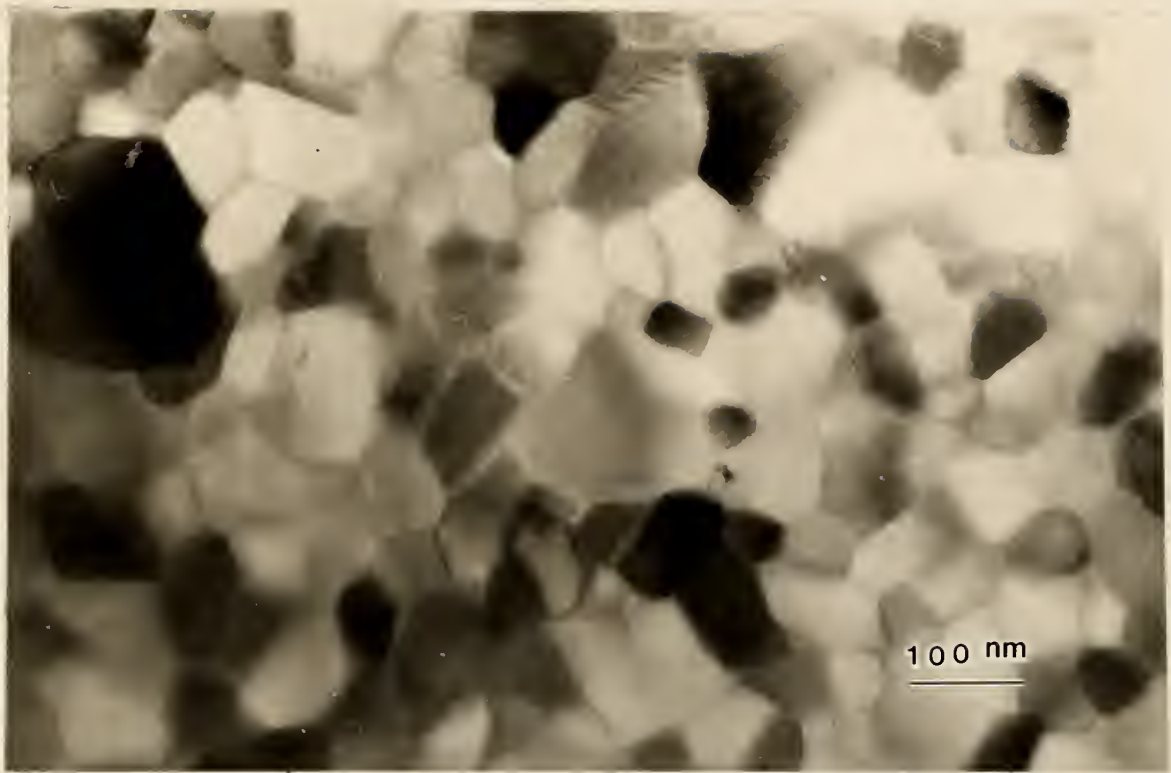


Fig. 6.1 The grain sizes of single phase $Nd_2Fe_{14}B$ ribbons with optimum wheel speed.

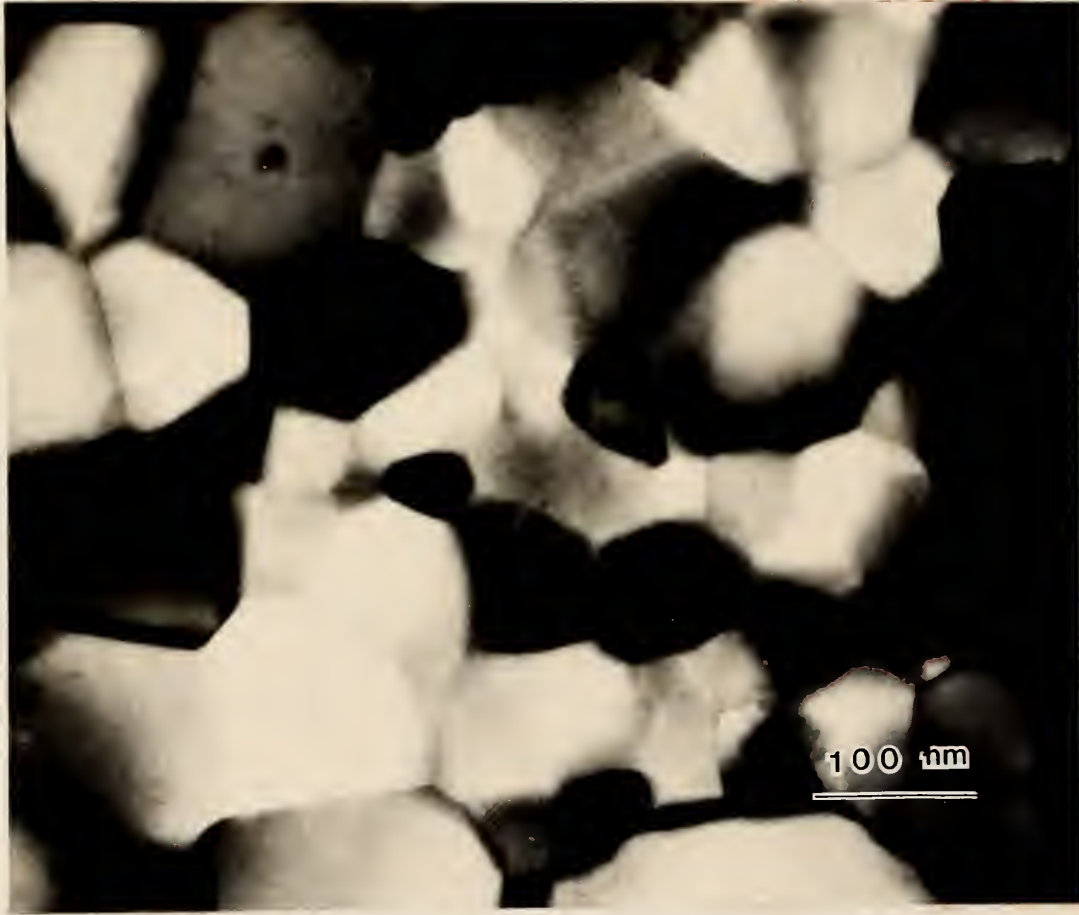


Fig. 6.2 The grain size of single phase $Dy_2Fe_{14}B$ ribbons with optimum wheel speed.

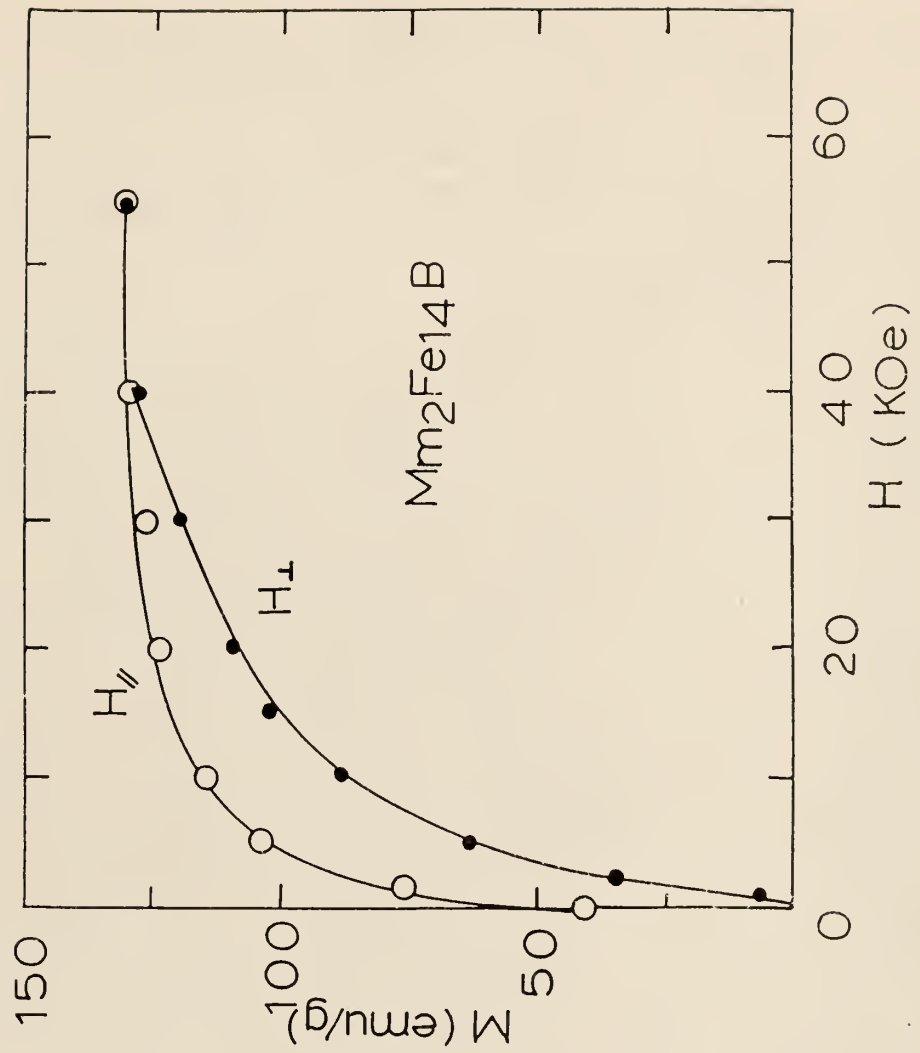


Fig. 6.3 The magnetization curves of the $Mm_2Fe_{14}B$ powder were measured in applied fields parallel and perpendicular to the aligned direction of the powder. The anisotropy field $H_A = 40$ KOe at room temperature.

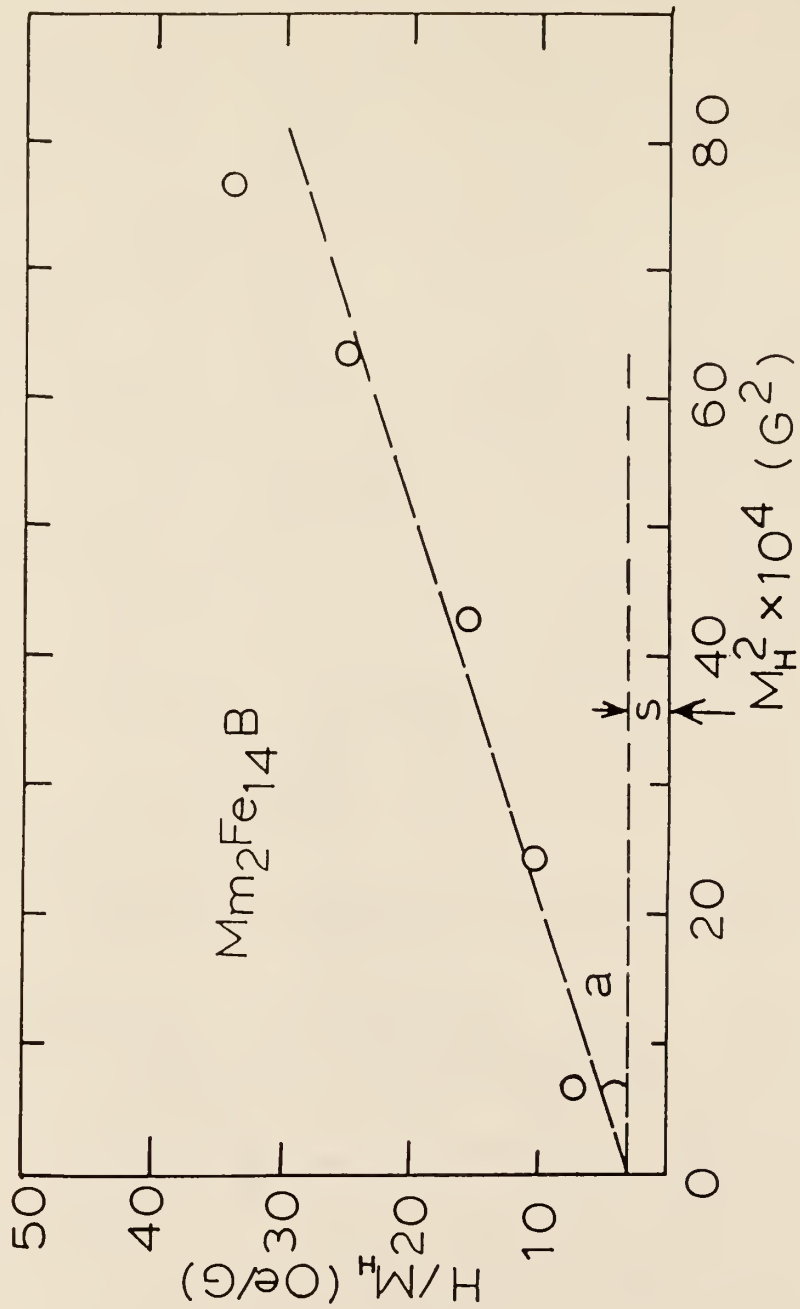


Fig. 6.4 The anisotropy constants K_1 , K_2 and K were calculated by plotting M_H^2 versus H/M_H .

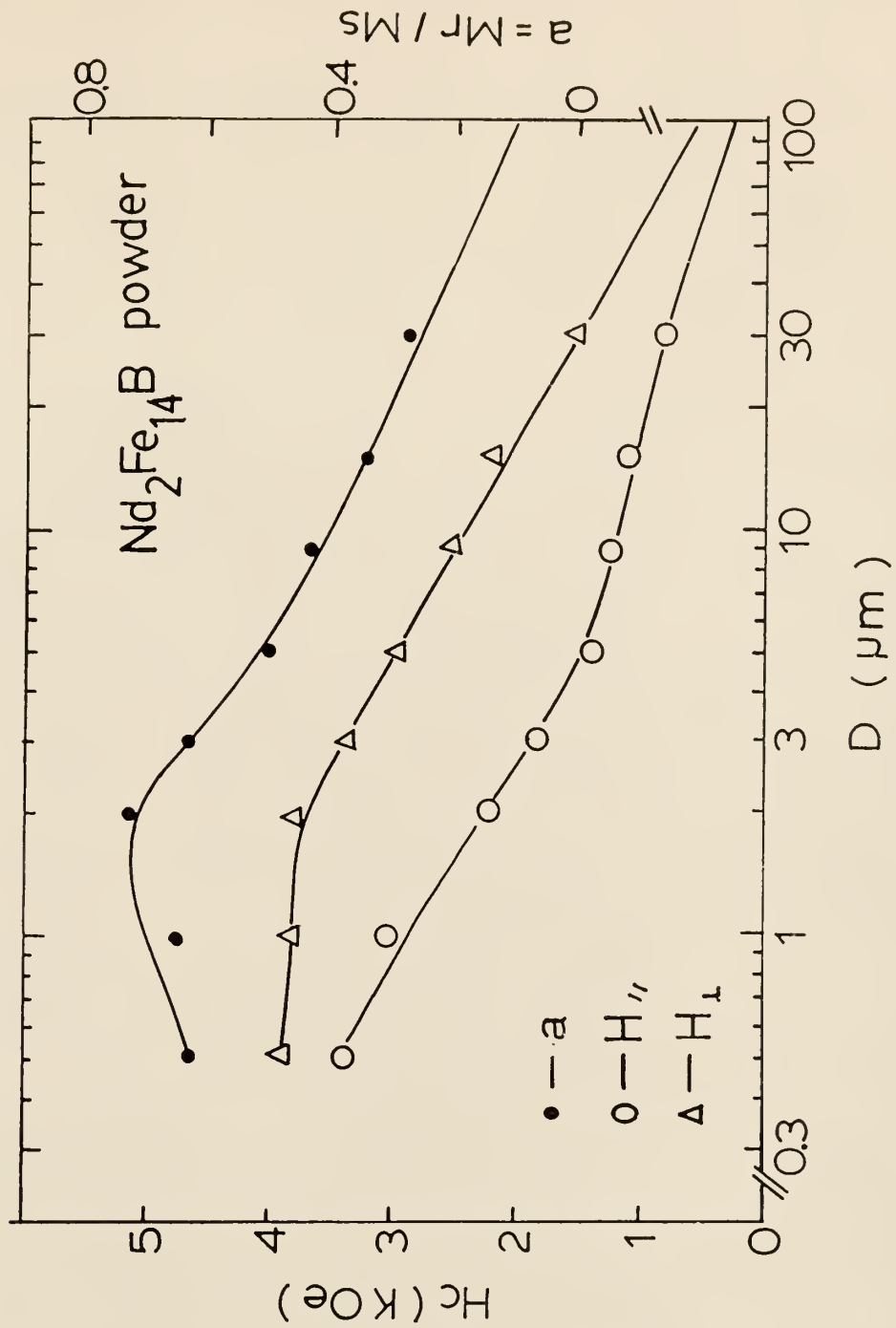


Fig. 6.5 Magnetic properties of single phase $\text{Nd}_2\text{Fe}_{14}\text{B}$ powder versus particle sizes D . D was an average powder particle size taken from SEM pictures.

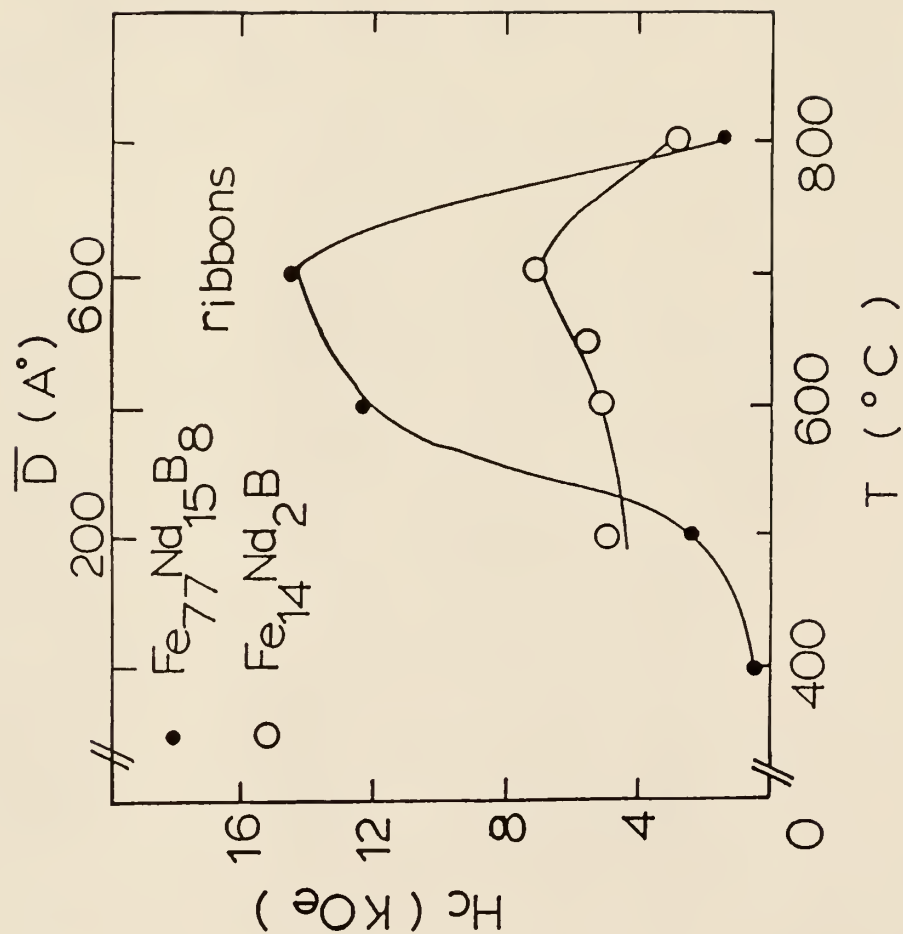


Fig. 6.6 The coercivity H_c of Nd-Fe-B ribbons versus the grain size. The maximum H_c was obtained by annealing at 700 °C/30 min with an average grain size $D = 600 \text{ \AA}$, $H_c = 8 \text{ KOe}$ and 15KOe for single phase $\text{Nd}_2\text{Fe}_{14}\text{B}$ and $\text{Nd}_{15}\text{Fe}_{77}\text{B}_8$, respectively.

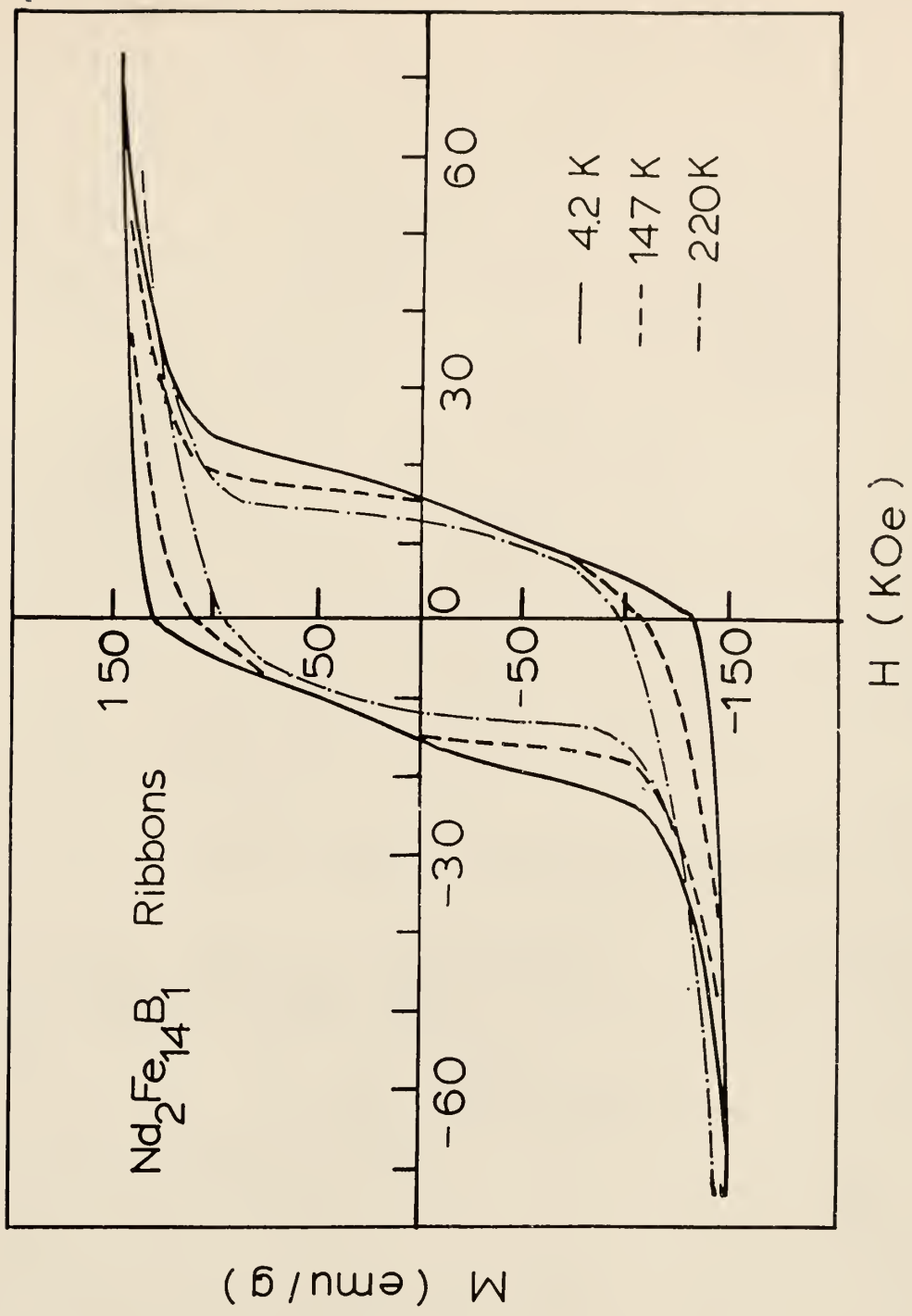


Fig. 6.7 The hysteresis loops of single phase $Nd_2Fe_{14}B$ at different temperatures.

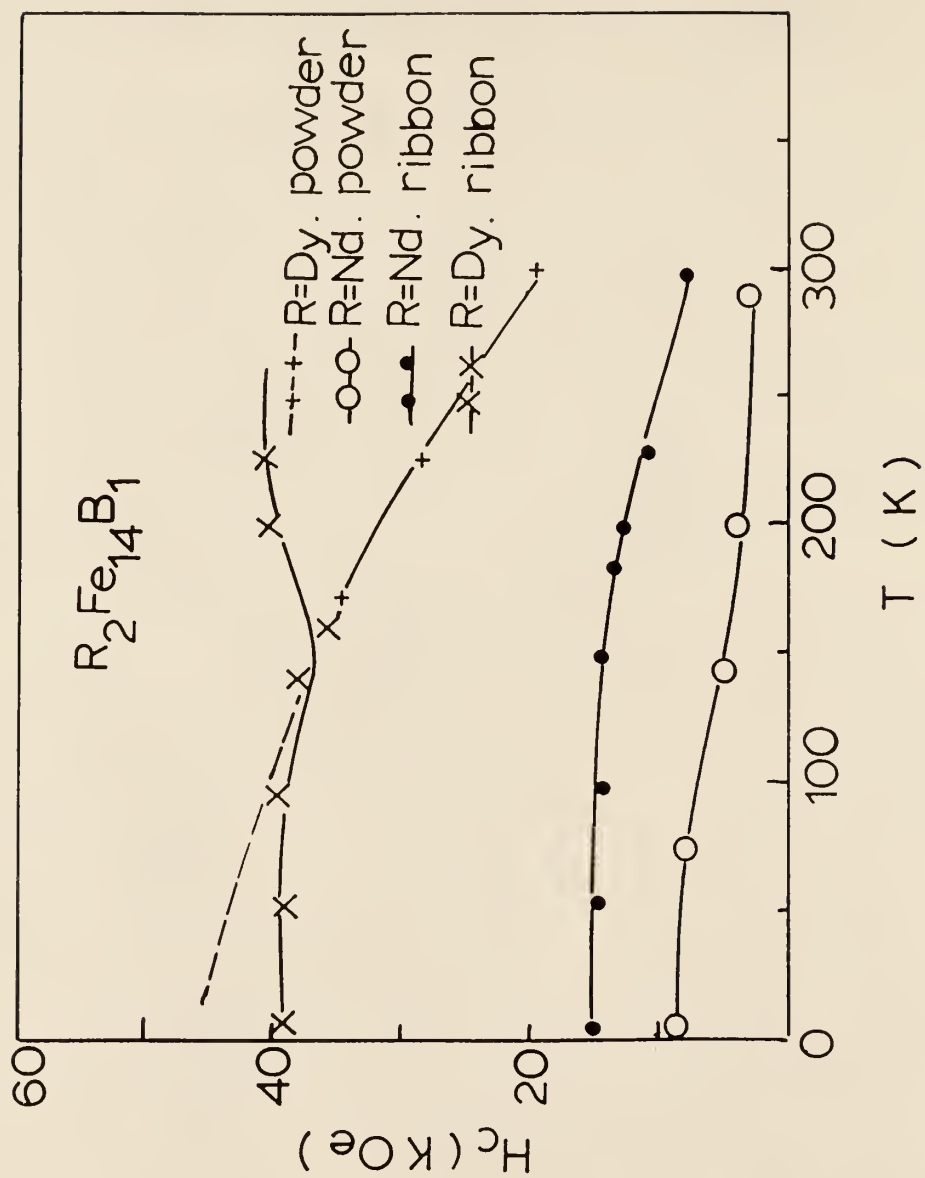


Fig. 6.8 The coercivity of the single phase $R_2Fe_{14}B$ ($R = Nd, Dy$) powder and ribbons as a function of temperatures. $Dy_2Fe_{14}B$ samples were not saturated by an applied field $H = 72$ KOe.

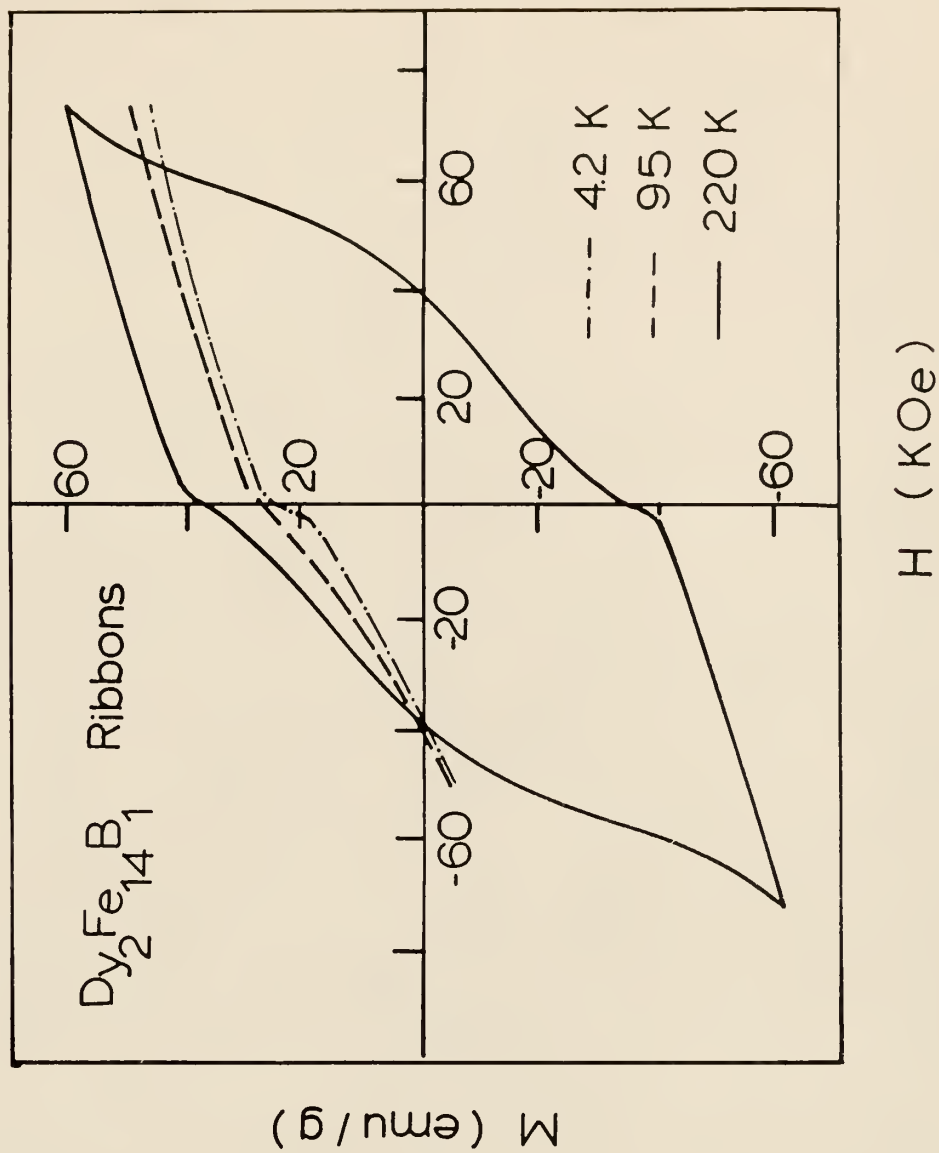


Fig. 6.9 The hysteresis loops of single phase $Dy_2Fe_{14}B$ at different temperatures.

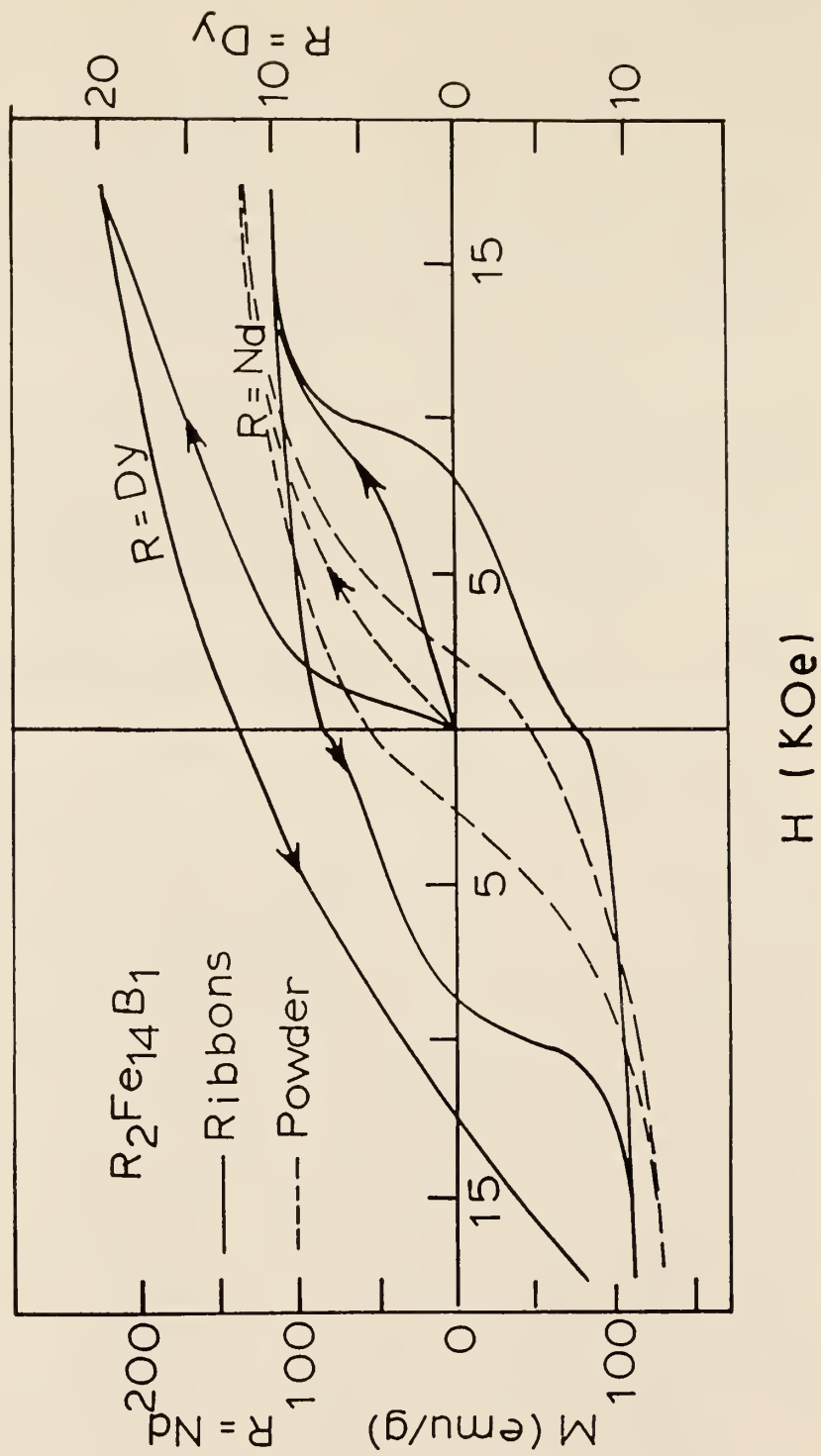


Fig. 6.10 The initial curves and hysteresis loops of single phase $R_2Fe_{14}B_1$ ($R = Nd, Dy$) powder and ribbons at room temperature.

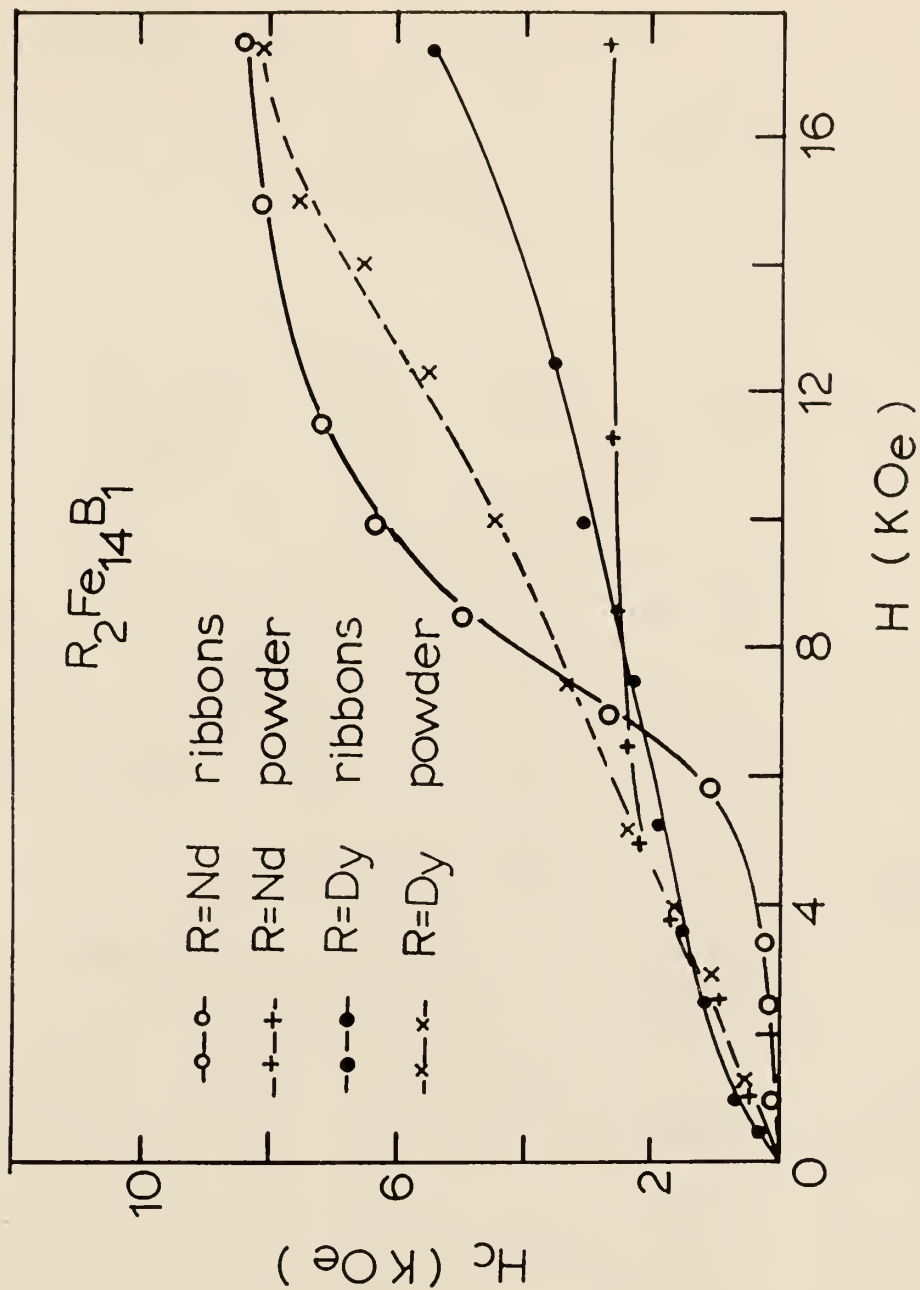


Fig. 6.11 The coercivity H_c of $R_2Fe_{14}B$ ($R = Nd, Dy$) powder and ribbons as a function of applied field H ($H = 17.5$ K Oe).

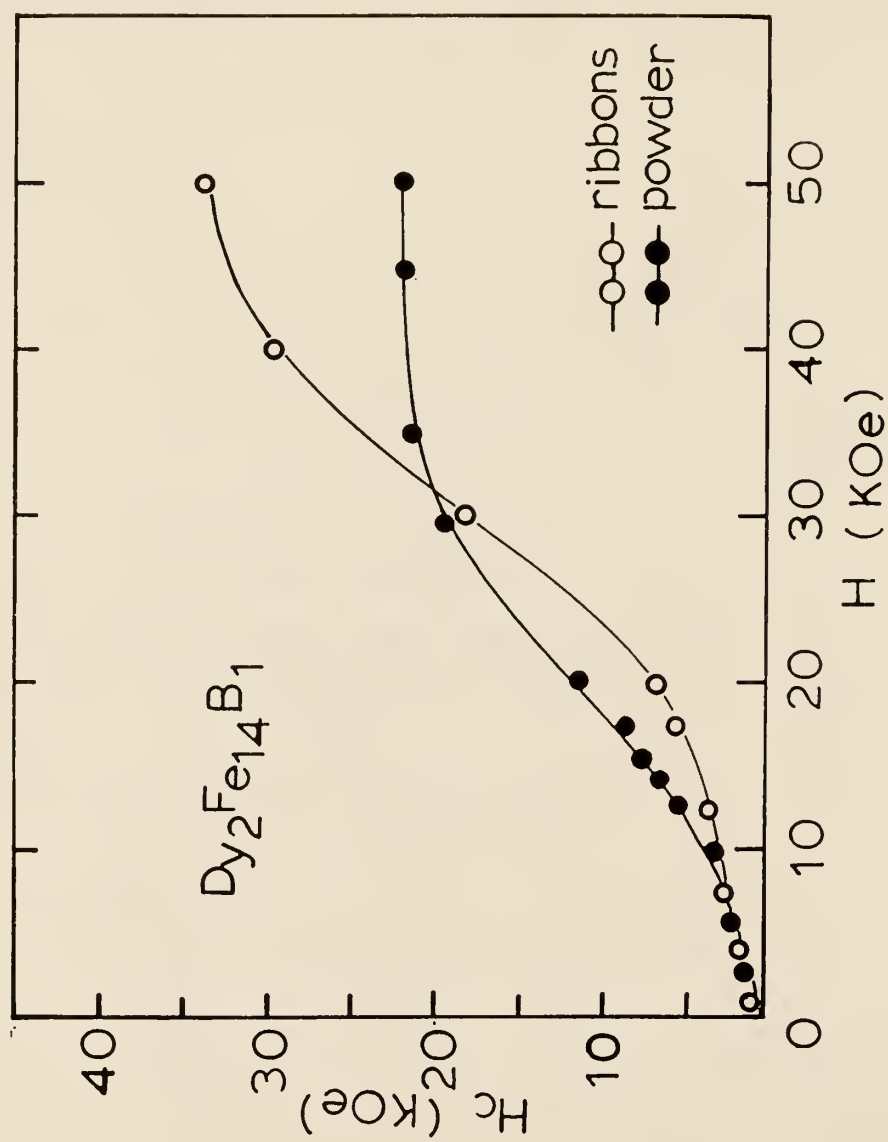


Fig. 6.12 The coercivity H_c of $R_2Fe_{14}B$ ($R = Nd, Dy$) and ribbons as a function of applied field H ($H = 55$ KOe).

CONCLUSIONS

- (1) There is a great potential in Mn-Fe-B alloys for permanent magnet development.
- (2) In Mn-Fe-B magnets, the coercivities were improved by adding small amounts of Al, Dy and Dy_2O_3 . An optimum composition $Fe_{75}Al_1Mn_{16}Dy_1B_7$ with 5 wt% Dy_2O_3 was found. The best properties are $H_c = 7 \sim 9$ KOe, $4\pi M_r = 7500 \sim 8000$ G, $(BH)_{max} \approx 12$ MGOe and $T_c = 515$ K. The price per energy product of the sample may compete with Ferrites.
- (3) There is a main $Mm_2Fe_{14}B$ phase in Mn-Fe-B magnets, which has a tetragonal structure with $a = 8.80$ Å and $c = 12.21$ Å. The magnetization M_s and anisotropy field H_A of the $Mm_2Fe_{14}B$ is $M_s = 132$ emu/g and $H_A = 40$ KOe at room temperature. $M_s = 142$ emu/g at 5 K. The uniaxial anisotropy constants K , K_1 and K_2 are $K = 1.93 \times 10^7$ erg/cm³, $K_1 = 1.39 \times 10^6$ erg/cm³, $K_2 = 7.18 \times 10^6$ erg/cm³, at room temperature.
- (4) The additions of 5 wt% Dy_2O_3 , 3 at% Dy and 5 at% Co in Mn-Fe-B based magnets, lead to an increase in Curie temperature T_c by about 15, 30 and 60 °C respectively. On the contrary, T_c was decreased by 25 °C with addition of 5 at% Al.
- (5) For $Nd_2Fe_{14}B$ powder samples, the critical single domain size is about 0.3 μm. This size is in agreement with the theoretical calculated value. The coercivity of the powder may be attributed to high crystalline anisotropy.
- (6) For R-Fe-B (R = Nd, Dy) ribbon magnets, the coercivities depended strongly on the grain size. The critical size for single domain particles D_s is about 600 Å in the ribbons. In general, the grain size for optimum coercivity H_c is in a range of 500 ~ 1000 Å. The coercivity of the $R_2Fe_{14}B$ (R = Nd, Dy) ribbons was controlled by domain wall pinning.

REFERENCES

- [1] "The Physical Principles of Magnetism", Allan H. Morrish, John Wiley and Sons, Inc., (1965) p.1.
- [2] B. Wilson, Phil. Trans. Roy. Soc. London **69**, 51 (1779).
- [3] T. Mishima, Iron Age **130**, 346 (1932).
- [4] C. Kittel, Revs. Modern Phys. **21**, 541 (1949).
- [5] "Alnico Permanent Magnet Alloys", De vos, Academic Press, New York, London (1969) p.473.
- [6] J. D. Fast and J. J. de Jong, J. de Phys. Radium **20**, 371 (1959).
- [7] K. J. Strnat, G. J. Hoffer, W. Ostertag, and I. C. Olson, J. Appl. Phys. **37**, 1252 (1966).
- [8] "Rare Earth-Cobalt Permanent Magnets", Wheeler Associates, Inc., (1979).
- [9] K. H. J. Buschow, " Ferromagnetic Materials" Vol.1 Chap.4, edited by E. P. Wohlfarth, North-Holland Publishing company, 1980.
- [10] N. C. Koon and B. N. Das, Appl. Phys. Lett. **39**, 840 (1981).
- [11] J. J. Croat, Appl. Phys. Lett. **39**, 357 (1981).
- [12] G. C. Hadjipanayis, R. C. Hazelton, and K. R. Lawless, Appl. Phys. Lett. **43**, 797 (1983).
- [13] J. J. Croat, J. F. Herbst, R. w. Lee, and F. E. Pinkerton, J. Appl. Phys. **55**, 2078 (1984).
- [14] N. C. Koon and B. N. Das, J. Appl. Phys. **55**, 2063 (1984).
- [15] M. Sagawa, S. Fujimura, N. Togawa, H. Yamamoto, and Y. Matsuura, J. Appl. Phys. **55**, 2083 (1984).
- [16] D. Givord, H. S. Li, and J. M. Moreau, Solid State Commun. **50**, 497 (1984).
- [17] J. H. Herbst, J. J. Croat, F. E. Pinkerton and W. B. Yelon, Phys. Rev. **29**, 4176 (1984).
- [18] M. Sagawa, S. Fujimura, H. Yamamete, Y. Matsuura, and K. Hiraga, IEEE Trans. Magn. **MAG-20**, 1584 (1984).

- [19] C. Abache and H. Oesterreicher, *J. Appl. Phys.* **60**, 1114 (1986)
- [20] M. H. Ghandehari, *Appl. Phys. Lett.* **48**, 548 (1986).
- [21] M. Sagawa, S. Hirosawa, H. Yamamoto, S. Fujimura, and Y. Matsuura, *Japa. J. Appl. Phys.* **26**, 785 (1987).
- [22] U. Enz, "Ferromagnetic Mterials" Vol.3 Chap.1, edited by E. P. Wohlfarth, North-Holland Publishing co., 1982.
- [23] C. A. M. Ven den Broek and A. L. Stuijts, *Phlips Techn. Rev.* **37**, 157 (1977).
- [24] J. J. Went, *Phlips Techn. Rev.* **13**, 194 (1952).
- [25] G. C. Hadjipanayis, Y. F. Tao and K. Gudimetta, *Appl. Phys. Lett.* **47**, 757 (1985).
- [26] S. Sinnema, R. J. Radwanski and J. J. M. Franse, *J. M. M. M.* **44**, 333 (1984).
- [27] S. Hirosawa, Y. Matsuura, H. Yamamoto, S. Fujimura, and M. Sagawa, *J. Appl. Phys.* **59**, 873 (1986).
- [28] C. Abache and J. Oesterreicher, *J. Appl. Phys.* **60**, 3671 (1986).
- [29] C. R. Paik, H. Miho, M. Okada, and M. Homma, *inte mag. Tokyo Japan* (1987).
- [30] O. Popov, V. Skumryen and M. Mikhov, *J. M. M. M.* **71**, L7 (1987).
- [31] J. Yamasaki, H. Yanagida, K. Mohri, N. Teshima, O. Kohmoto, T. Yoneyama, and N. Yamaguchi, *TEEE Trans. Magn.* **MAG-20**, 763 (1986).
- [32] W. Gong and G. C. Hadjipanayis, *J. Appl. Phys.* **63**, 3513 (1988).
- [33] "The Physical Principles of Magnetism", Allan H. Morrish, John wiley and Sons, Inc., (1965) p.353
- [34] L. Neel, *Compt. Rend.* **224**, 1550 (1947)
- [35] C. Guillaud, *J. Phys. Radium*, **8**, 347 (1947).
- [36] E. C. Stoner and E. R. Wohlfarth, *Phil. Trans. Roy. Soc. London* **A240** 599 (1948).
- [37] Wang Zhen-xi, Gong Wei, Wong Yi-zhon, Feng Min-ying, Wu Zhon-lin

- Chinese Phys. Lett. **2**, No.2 (1985).
- [38] W. Sucksmith, F. E. Thompson, Proc. Roy. Soc. (London) **A67**, 505 (1954).
- [39] Wang Yi-zhong, Wang Zhen-xi, Gong Wei, Feng Min-ying, Chinese Phys. Lett. **2**, No.8 (1985).
- [40] C. W. Chen, "Magnetism and Metallurgy of Soft Magnetic Materials" Vol. XV, North-Holland (1977).
- [41] R. C. Weast, "Handbook of Chemistry and Physics" 65 th Edition 1984-1985, CRC Press PE-104.
- [42] P. Weiss, J. Phys. **6**, 667 (1907).
- [43] D. J. Craik and R. S. Tebble, Ferromagnetism and Ferromagnetic Domains," John Wiley and Sons, Inc, New York (1965).
- [44] "Ferromagnetism and Ferromagnetic Domains", D. J. Craik and R. S. Tebble, John Wiley and Sons Inc, New York (1965) p36.
- [45] J. D. Livingston, J. Appl. Phys **57**, 4137 (1985).
- [46] "Introduction to Magnetic materials," B. D. Cullity, Addison-Wesley Publishing Co, (1972) p387.
- [47] E. H. Frei, S. Shtrikman and D. Trrves, Phys. Rev. **106** ,446 (1957).
- [48] A. Aharoni and S. Shtrikman, Phys. Rev. **109**, 1522 (1958).
- [49] A. Menth, H. Nagel and R. S. Perkins, in Ann. Rev. Materials Science, Edited by R. A. Huggins et al, Vol.8 (1978) P21.
- [50] W. F. Brown, Rev. Mod. Phys. **17**, 15 (1945).
- [51] H. Kronmueler, J. Magn. Magn. Mat. **7**, 341 (1978).
- [52] H. Kronmueler, K. D. Durst and G. Martinek, J. Magn. Magn. Mat. **69**, 149 (1987).
- [53] M. Kersten, Phys. Z. **44**, 63 (1943).
- [54] S. Foner, Rev. Sci. Instr. **30**, 548 (1959).
- [55] E. Babic, E. Girt, R. Krsnik and B. Zeontic. J. Phys. E. Scientific Instruments **3**, 1015 (1970).
- [56] "Elements of X-Ray Diffraction", B. D. Cullity, Addison Wesley Pub-

- lishing Company, Colifornia, London, (1978).
- [57] K. H. J. Buschow, H. M. Van Noort and D. B. de Mooij, *J. Less-common Metals* **109** 79 (1985).
 - [58] E. Butzo, A. T. Pedziwiatr and W. E. Wallace, *Sol. State. Comm.* **61**, 51 (1986).
 - [59] J. D. Livingston , *The Internationalworkshop on Rare-Earth Magnets and Their Applications*, Dayton, Ohio. May (1985).
 - [60] M. Sagawa et al. *J. Appl. Phys.* **55**, 2083 (1984).
 - [61] J. F. Herbst and W. B. Yelon, *J. Appl. Phys.* **57**, 2343 (1985).

ABSTRACT

The outstanding hard magnetic properties of Nd-Fe-B alloys are due to the tetragonal $Nd_2Fe_{14}B_1$ phase. However, the high cost of Nd keeps the price of Nd-Fe-B magnets much higher than Ferrites which find wide applications. In fact, the tetragonal $R_2Fe_{14}B_1$ phase is found with most Rare Earth elements and a great potential exists for Misch metal based Mm-Fe-B alloys for permanent magnet development. The purpose of this work has been to study the magnetic and microstructure properties of the Rare Earth-Iron-Boron based systems. The magnets were prepared by melt-spinning and powder metallurgy methods. The hard magnetic properties of the magnets were improved by adding small amounts of *Dy*, *Al* and Dy_2O_3 . An economical permanent magnet, whose price per energy product may compete with Ferrites, has the following magnetic properties; for a typical sample of $Fe_{75}Al_1Mm_{16}Dy_1B_7$ with 5 wt% Dy_2O_3 : $H_c = 7 \sim 9 KOe$, $4\pi M_r = 7800 G$, $(BH)_{max} \approx 12 MGoe$ and $T_c = 515 K$. The density of the alloy is $7.3 g/cm^3$. The high saturation M_s and Curie temperature T_c can be explained by the presence of $Mm_2Fe_{14}B_1$ phase in the alloy which has been confirmed by X-rays. The coercivity mechanism of the magnets is discussed by theoretical models associated with high magnetocrystalline anisotropy.

MAGNETIC AND MICROSTRUCTURE PROPERTIES
OF M_{11} -Fe-B PERMANENT MAGNETS

by

WEI GONG

B.S., Beijing University, 1978

AN ABSTRACT OF MASTER THESIS

submitted in partial fulfillment of the
requirements for the degree

MASTER OF SCIENCE

Department of Physics

College of Arts and Science

KANSAS STATE UNIVERSITY

Manhattan, Kansas

1988

ABSTRACT

The outstanding hard magnetic properties of Nd-Fe-B alloys are due to the tetragonal $Nd_2Fe_{14}B_1$ phase. However, the high cost of Nd keeps the price of Nd-Fe-B magnets much higher than Ferrites which find wide applications. In fact, the tetragonal $R_2Fe_{14}B_1$ phase is found with most Rare Earth elements and a great potential exists for Misch metal Mm-Fe-B alloys for permanent magnet development. The purpose of this work has been to study the magnetic and microstructure properties of the Rare Earth-Iron-Boron based systems. The magnets were prepared by melt-spinning and powder metallurgy methods. The hard magnetic properties of the magnets were improved by adding to small amounts of Dy, Al and Dy_2O_3 . An economical permanent magnet, whose price per energy product may compete with Ferrites, has the following magnetic properties; for a typical sample of $Fe_{75}Al_1Mm_{16}Dy_1B_7$ with 5 wt% Dy_2O_3 : $H_c = 7 \sim 9 KOe$, $4\pi M_r = 7800 G$, $(BH)_{max} \approx 12 MGOe$ and $T_c = 515 K$. The density of the alloy is $7.3 g/cm^3$. The high saturation M_s and Curie temperature T_c can be explained by the presence of $Mm_2Fe_{14}B_1$ phase in the alloy which has been confirmed by X-rays. The coercivity mechanism of the magnets is discussed by theoretical models associated with high magnetocrystalline anisotropy.